NOTE TO USERS

The original manuscript received by UMI contains pages with slanted print. Pages were microfilmed as received.

This reproduction is the best copy available.

UMI®

uOttawa

L'Université canadienne
Canada's university

FACULTÉ DES ÉTUDES SUPÉRIEURES ET POSTOCTORALES

uOttawa

L'Université canadienne
Canada's university

FACULTY OF GRADUATE AND POSDOCTORAL STUDIES

Carlos Leung

AUTEUR DE LA THÈSE / AUTHOR OF THESIS

M.A.Sc. (Mechanical Engineering)

GRADE / DEGREE

Department of Mechanical Engineering

FACULTÉ, ÉCOLE, DÉPARTEMENT / FACULTY, SCHOOL, DEPARTMENT

Examination of the Pulsating Detonation Instability in a Two-Step Model Using Characteristics

TITRE DE LA THÈSE / TITLE OF THESIS

Matei Radulescu

DIRECTEUR (DIRECTRICE) DE LA THÈSE / THESIS SUPERVISOR

CO-DIRECTEUR (CO-DIRECTRICE) DE LA THÈSE / THESIS CO-SUPERVISOR

Davide Spinello

Jason Etele

Gary W. Slater

Le Doyen de la Faculté des études supérieures et postdoctorales / Dean of the Faculty of Graduate and Postdoctoral Studies

Examination of the Pulsating Detonation Instability in a Two-Step Model using Characteristics

Carlos Leung

A thesis submitted to the Faculty of Graduate and Postdoctoral Studies
in partial fulfillment of the requirements for the degree of

MASTER OF APPLIED SCIENCE

in Mechanical Engineering

Ottawa-Carleton Institute for Mechanical and Aerospace Engineering
University of Ottawa
Ottawa, Canada
May 2010

Your file Votre référence
ISBN: 978-0-494-69022-2
Our file Notre référence
ISBN: 978-0-494-69022-2

Abstract

The nonlinear dynamics of one-dimensional pulsating detonations were studied numerically using a simple two-step chain branching model with separate induction and exothermic reaction zones. The stability boundary was found for a wide range of non-dimensional activation energy and heat release. The wave dynamics within the detonation structure responsible for non-linear pulsating instability were studied using the three families of characteristic curves on x-t diagrams, representing the trajectories of pressure waves and particle paths. This clarified the dynamics responsible for loss of stability and the period of the pulsating instability.

Four main regimes of pulsations were observed: the high frequency, very high frequency, low frequency and transition regimes. The high and very high frequency modes tend to manifest itself for low values of activation energy, while the low frequency mode tends to appear for higher activation energy. The very high frequency pulsations are governed by a cycle of expansion waves traveling across the induction zone along the C- characteristics coupled with the compression waves traveling across the induction zone along the C+ characteristics. The high frequency pulsations are controlled by a coupling between the particle path originating from the leading shock traveling across the induction zone and the compression wave traveling across the induction zone via the C+ characteristics. The low frequency oscillations involve the C- characteristics or particle paths traveling across the entire detonation from the shock followed by the C+ characteristics traveling toward the leading shock.

The mechanisms governing the pulsating instability and the periods of oscillation were found to be in good qualitative agreement with Toong's phenomenological model based on the wave dynamics in a square wave model.

Acknlowedgements

I would like to thank my research supervisor, Matei Radulescu, for continually providing a guiding hand and sharing his ideas on my work. Without his help and feedback, the completion of this thesis would not be possible. I would also like to thank James Quirk and Gary Sharpe, who have been a tremendous help in setting up the numerical simulations.

Table of Contents

List of Tables

List of Figures

Nomenclature

Variable	*Description*
Δ_i	Induction zone length
Δ_e	Reaction zone length
γ	Ratio of specific heat
λ_e	Reaction zone progress variable
λ_i	Induction zone progress variable
ν	Reaction order of reaction zone
ρ	Dimensionless density
$\tilde{\rho}$	Density
$\dot{\sigma}$	Thermicity
χ	Stability parameter
c	Acoustic speed
e	Specific internal energy
E	Dimensionless activation energy
$\tilde{E}$	Activation energy
k	One-step Arrhenius model scaling constant
K_i	Induction zone scaling constant (two-step model)
K_e	Reaction rate variable of reaction zone (two-step model)
M	Mach number of the leading shock
p	Dimensionless pressure
$\tilde{p}$	Pressure
$\tilde{Q}$	Heat release
Q	Dimensionless heat release
R	Ideal gas constant
T	Dimensionless temperature
$\tilde{T}$	Temperature
u	Dimensionless velocity

$\tilde{u}$	Velocity

Subscripts	*Description*
$\{\}_{CJ}$	Chapmann Jouguet state downstream of the reaction zone
$\{\}_{o}$	Unreacted state upstream of the shock
$\{\}_{s}$	Post shock state downstream of the shock

Chapter 1

Introduction

1.1 - Motivation

A detonation is a self-sustained supersonic combustion wave. It can be idealized as a leading shock wave coupled with a trailing chemical reaction zone, as shown schematically in *Figure 1.1*. Detonations rely on the propensity of the material to expand upon reaction, a property shared by most reactive materials generating product gases. The standard model for a detonation consists of a leading shock, across which no reactions occur, which serves to compress the material and initiate exothermic reactions. The ensuing combustion of the material, leading to material expansion, provides the work to maintain the propagation of the lead shock.

Detonations occur in reactive gases, combustion of dust particles in air, energetic materials in condensed form (explosives), and thermo-nuclear reactions (Fickett and Davis 1979). Detonations are thus of interest in propulsion applications, industrial safety, explosive applications and thermo-nuclear reactions in astrophysical phenomena, such as Supernovae explosions. Detonation models have also been used to model other astrophysical explosions (Oran 2005), phase change waves (Gulen et al. 1994), traffic jams (Flynn et al. 2009), shallow water waves (Kasimov 2008) and other self-sustained wave propagation phenomena.

The speed at which detonations propagate, known as the Chapman-Jouguet (CJ) detonation velocity, is unique for any reactive medium. It is independent of the details inside the reaction zone structure, and only depends on the global energy release across the reaction zone. A sketch of a CJ detonation wave is shown in *Figure 1.1*. The CJ detonation describes a detonation propagating such that flow velocity in the burnt region

behind the reaction zone, in the reference frame of the leading shock, is sonic. As a result, acoustic signals originating from the burnt region will never reach the shock and influence the dynamics of the detonation, hence providing an information boundary (event horizon), making the detonation wave self-sustained (Fickett and Davis 1979).

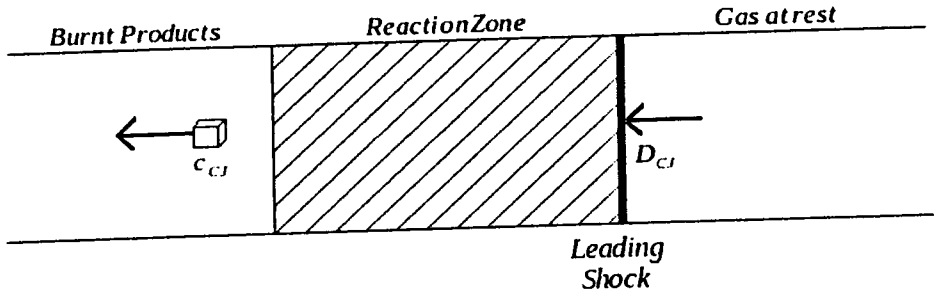

Figure 1.1 - Sketch of a CJ detonation wave. D_{CJ} is the velocity of the leading shock, u_{CJ} is the velocity of the burnt gas, and c_{CJ} is the speed of sound in the burnt region.

The simplest hydrodynamic model for a detonation is obtained from the usual conservation laws in which diffusion transport terms are neglected (i.e., the reactive Euler equations) coupled with a rate law for the consumption of the reactants. The earliest theory, developed independently by Zel'dovich (1940), von Neumann (1942), and Doering (1943), assumed that detonations were steady waves propagating with the one-dimensional structure shown in *Figure 1.1*. Under these assumptions, the reactive Euler equations can be simplified and the steady state solution (also called the ZND solution after its founders) can be obtained. However, the steady solution is rarely seen in practice and experiments show that detonations are typically very unstable to flow perturbations (Lee 2008).

Two distinct modes of instability have been observed experimentally. In multiple dimensions, the instability is seen as a complex cellular structure (Strehlow 1968). In one dimension, the instability manifests itself as a pulsating instability, as seen experimentally along the stagnation streamline of a supersonic projectile fired into a detonable mixture (Lehr 1972; Alpert and Toong 1972). Both the highly non-linear cellular structures and pulsating dynamics are currently very poorly understood, requiring direct numerical simulations for their prediction.

The current work is a numerical investigation focusing on the study of the one-dimensional pulsating mode of instability. In this work, the physical mechanisms governing the instability will be studied in detail.

1.2 - Previous Work

Most previous work on detonation stability assumes the ZND model and studies how the structure becomes unstable in single and multiple dimensions as a function of time. Below, the various models for the ZND reaction zone structure are briefly reviewed, along with the techniques used to study the linear and non-linear stability of the structure.

1.2.0 - The ZND model with realistic thermo-chemistry

The ZND structure of real detonations can be obtained by integrating the governing steady conservation laws along with a complex network of chemical reactions initiated behind the shock, which is always assumed to be non-reactive. Realistic ZND detonation structures typically consist of an induction zone in which very little heat is liberated and all fluid properties (density, pressure, temperature, velocity) remain approximately constant , followed by a thin region of rapid heat release. *Figure 1.2*

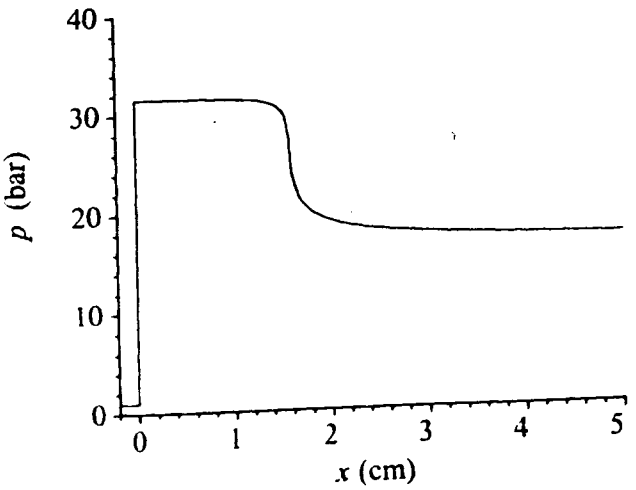

Figure 1.2 - Calculated steady state structure of a CJ detonation in methane- air mixture (taken from Law 2006)

shows, for example, the steady state structure of a detonation propagating through a stoichiometric methane-air mixture.

To date, although quite realistic reaction zone structures can be computed in this fashion, the study of the reaction stability is very difficult, due to the required computational price in computing the complex chemical kinetics. The complexity of the dynamic interactions also make the interpretation of the results quite difficult. Likewise, although few non-linear detonation stability studies have been attempted in 1D by direct numerical simulation (Daimon and Matsuo 2007), multi-dimensional studies are currently very difficult to conduct (Powers 2005). For this reason, simpler models are usually sought, which offer a practical way to conduct large-scale simulations, while offering the analytical transparency to clarify the dynamics.

1.2.1 - The square wave model

A close idealization to the realistic structure of the ZND model was obtained by the square wave model (Shchelkin 1965). In the square wave model, the leading shock is followed by a thermally neutral induction zone, in which no heat is released, followed by an infinitely thin reaction zone where all of the heat is released instantaneously. Only the induction zone duration is assumed to depend exponentially on the shock strength, in order to capture the realistic dependence. The square wave is similar in structure to realistic detonations, and provides a reasonable approximation to actual detonations (Fickett and Davis 1979).

Early attempts at unraveling the pulsating mechanism of detonations was based on the square wave model (Alpert and Toong 1972). Using the simplified square wave model, Alpert and Toong (1972) proposed a semi-quantitative description of the pulsating instability. A schematic of Toong's mechanism can be seen in *Figure 1.3*.

The dynamics of the reaction zone structure are given in a frame of reference of the mean detonation propagation, such that the position of the lead shock and reaction zone appears stationary when plotted on an space-time diagram, such as *Figure 1.3*. The instability cycle begins when a compression wave from the interior overtakes the shock front at t_0. This causes a strengthening and acceleration of the shock front, creating a

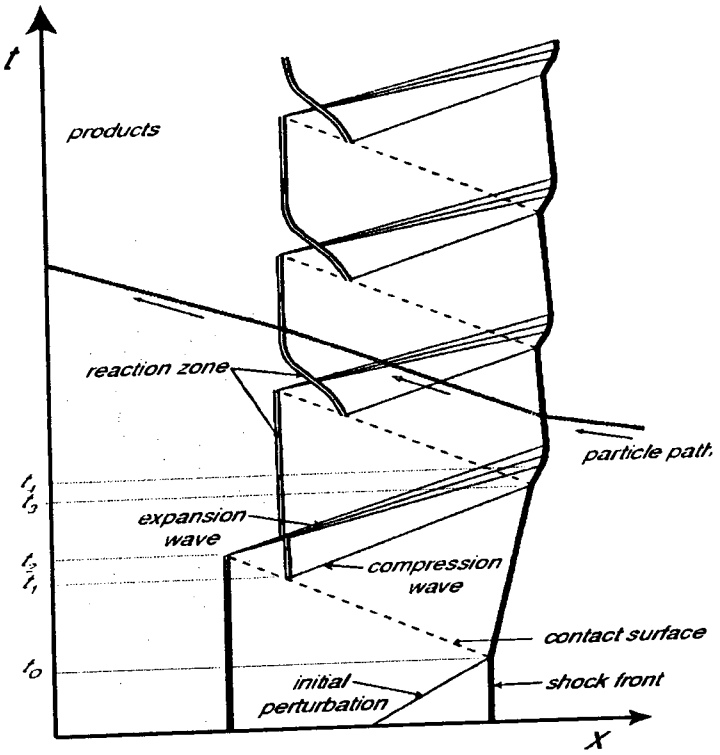

Figure 1.3 - Schematic of Toong's mechanism for pulsating instability (taken from Law 2006)

contact surface (represented by the dashed lines) above which the gas particles processed by the strengthened shock are hotter. The first hotter particle will react faster, leading to a shortening of the induction zone and a creation of a new reaction zone at t_1. The old reaction zone terminates at t_2 when the reaction of the last undisturbed particle completes. The creation of the new reaction zone triggers a compression wave and the termination of the old reaction zone creates an expansion. The next cycle begins when the compression wave catches up to the shock front, strengthening the shock at t_3. The expansion wave reaches the shock front at t_4, decelerating the shock, between t_0 and t_3.

Toong's mechanism, however, is pathological, as the square wave structure has been shown by Zaidel (1961) to be always unstable. The square wave model is thus unsuited for the study of the onset of instability, and as such, a more realistic chemical model is needed.

1.2.2 - One-step Arrhenius model

The simplest reaction zone model free of singularities in the reaction zone is the irreversible one-step Arrhenius model. In this model, it is assumed that the rate of energy release follows the classical Arrhenius dependence, given by:

$$\frac{D\lambda}{Dt} = k(1-\lambda)\exp\left(\frac{-\tilde{E}}{R\tilde{T}}\right)$$

A detailed description of the one-step Arrhenius model can be found in Fickett and Davis (1979). The Arrhenius model usually has a more distributed structure, where an induction zone can no longer be identified. A sample ZND structure for the one-step model is shown in *Figure 1.4*.

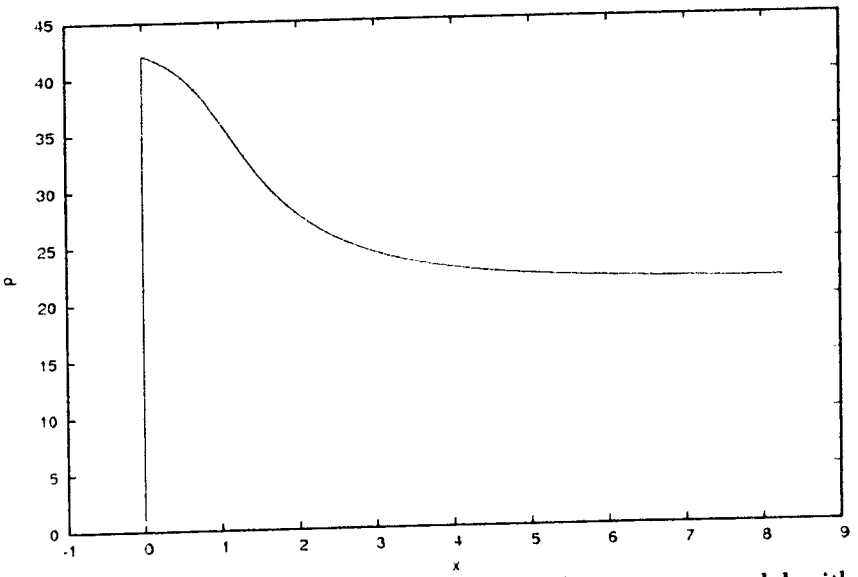

Figure 1.4 - Sample ZND pressure profile of the one-step model with parameters $\tilde{E}/R\tilde{T}_o = 27$, $\tilde{Q}/R\tilde{T}_o = 50$, $\gamma = 1.2$

1.2.2.1 Linear stability of one-step model

The earliest formal linear stability analysis of detonations was pioneered by Erpenbeck (1962). Erpenbeck's work involved a one-step Arrhenius chemical model. In his stability analysis, Erpenbeck calculated the stability boundary numerically for various parameters of the linearized equations using a Laplace transform technique. However,

due to analytical difficulties, his technique was not applicable to the CJ case. Since then, different techniques were developed to calculating the linear stability boundary, such as the normal mode approach used by Lee and Stewart (1990) and Sharpe (1997), and the recent reworking of Erpenbeck's method by Tumin (2007).

In the aforementioned works, extensive numerical treatment of the linear stability problem was required, due to the non constant coefficients in the ordinary differential equations generated. Furthermore, little insight of the non-linear pulsating mechanisms can be extracted from these studies. However, the linear stability of a detonation can be examined analytically using asymptotic limits. One of the earliest examples was done by Buckmaster and Neves (1989), where the linear stability of the one-step model was analyzed in the limit of very high activation energies. Under this limit, the detonation structure reduces to the square wave structure (Fickett and Davis 1979). It was shown in this work, and later confirmed by the linear stability analysis of Short (1996), that the one-step model in the limit of very high activation energies was intrinsically unstable, displaying the same pathology found by Zaidel (1961). Other asymptotic limits, such as the Newtonian limit, the limit as the ratio of specific heats approaches unity, (Short 1996) have been studied.

1.2.2.2 - Direct numerical simulations of the one-step model

Linear stability analysis provides insight on the detonation sensitivity to small, linear perturbations. It is useful for predicting the onset of instability, and provides information on the growth rate of the perturbations. However, linear stability analysis provides no information on the long term non-linear behaviour of the pulsations. Direct numerical simulations have been performed in order to study the non-linear behaviour of pulsating detonations. One of the early studies was done by Fickett and Wood (1964), in which the time dependent equations were solved using the method of characteristics. They showed that the stability limits found through non-linear simulations agreed well with the linear stability results of Erpenbeck. In the stable regimes, the long-time solution eventually converged to the ZND solution, and in the unstable regime, the pulsations of the shock pressure saturated at a final amplitude. Since then, many non-linear simulations

were performed and compared to the stability limits obtained through linear analysis. Bourlioux et. al (1991) used a finite volume technique and was able to produce results in close agreement with Lee and Stewart's (1990) results. Sharpe and Falle (1999) ran simulations varying activation energy, and found that for low activation energies, where non-linear effects did not play a significant role, the results agreed with the linear stability results obtained by Sharpe (1997). Daimon and Matsuo (2002) ran simulations varying overdrive, and the stability limits obtained agreed well with Lee and Stewart (1990). More recently, Ng et al. (2005[a]) showed that the dynamics of the one-dimensional detonation with a one-step reaction follow the classical route to chaos through period doubling bifurcations as the activation energy was increased. Moreover, the sequence of bifurcations followed the universal route to chaos, where subsequent bifurcations reproduced Feigenbaum's constant (Strogatz, 1994). The reason for this is puzzling and still unknown, although it demonstrates that the detonation paradigm appears useful to study other non-linear phenomena sharing the same dynamics.

Although useful, the one step model suffers from the main drawback that for realistic values of the activation energy, a well defined induction zone is not apparent (Fickett and Davis 1979). Only for unrealistically high activation energies, the profile develops a clear thermally neutral induction zone. However, the reaction zone becomes extremely thin in this limit; the wave structure thus approaches that of the square wave, and becomes pathologically unstable. The weakness with the one-step model is thus that the structure is governed by the single variable, the activation energy, and that by modifying the activation energy, the properties of the induction and reaction zone change simultaneously. As such, a large number of realistic reactions cannot be properly represented by the one-step model (Short and Quirk 1997). More importantly, however, is that the inability to properly control the induction and reaction zones separately makes insight into the stability problem, the pulsating dynamics and transition to chaos difficult.

1.2.3 - Two-step chain branching model

The two-step chain branching model is the simplest model that addresses the weaknesses of the one-step model and the square wave model. The two-step model is a

natural extension of the square wave model, consisting of a temperature dependent induction zone with no heat release, followed by a finite, temperature independent exothermic reaction zone.

Analytical work has been done on the two-step model, including the work of Clavin et al (1997), where the stability was studied using the Newtonian limit and a high degree of overdrive, and in the work of Short (2001), using the asymptotic limit of high activation energy in the induction zone. In Short's work, it was found that the stability is governed by ratio of the induction and reaction zone lengths. A longer reaction zone relative to the induction zone has a stabilizing effect on the detonation. Indeed, Short's predictions were confirmed by the non-linear numerical simulations of Short and Sharpe (2003) and [b]Ng et al. (2005). The latter also studied the transition to chaos and again reproduced Feigenbaum's universal bifurcation route. In both works, it was found that the the stability limit can be well correlated by a stability parameter, defined as the product of the non-dimensional activation energy and the ratio of the induction length to reaction length. No clear interpretation was however provided for this criterion.

1.3 - Present Study

Despite the numerous studies on pulsating detonation instability, the current understanding of the underlying physical mechanisms is not satisfactory. In previous work, it has been shown that stability is governed by the activation energy of the induction zone and the ratio of the induction and reaction zone lengths. However, the role that the parameters play and their effect on the wave dynamic features of the pulsations remain unclear. The present study is a numerical investigation that attempts to identify the mechanisms responsible for the pulsations, and to clarify the role played by the temperature sensitivity of the induction zone and the length of the reaction layer. More importantly, the current work develops a strategy in studying the non-linear wave dynamic interactions.

The current work employs the two-step chain branching model. The two-step model allows for independent control over the induction zone and reaction zone, ensuring the existence of an induction zone. Further, unlike the square wave model, the two-step

model is not pathologically unstable. The two-step model is the simplest non-pathological model with an induction zone, allowing us to examine the pulsating dynamics in the same framework as Alpert and Toong's square wave model analysis.

The pulsating wave dynamics are studied through the reconstruction of the family of characteristics. The characteristic curves track the trajectories of the particle paths, compression waves and expansion waves. By reconstructing and examining the family of characteristics of a pulsating detonation, the gas dynamic interactions can more easily and clearly be studied.

The outline of this work is as follows: The mathematical model used will be discussed in Chapter 2. The numerical method employed will be discussed in Chapter 3. Chapter 4 presents the results obtained through numerical simulations. Finally, Chapter 5 contains concluding remarks.

Chapter 2

The Model

2.1 - Governing Equations

The fluid was modeled by the one-dimensional reactive Euler equations, describing the conservation of mass (2.1), momentum (2.2) and energy (2.3) in the lab frame respectively:

$$\frac{\partial \tilde{\rho}}{\partial \tilde{t}} + \frac{\partial (\tilde{\rho}\tilde{u})}{\partial \tilde{x}} = 0 \tag{2.1}$$

$$\frac{\partial (\tilde{\rho}\tilde{u})}{\partial \tilde{t}} + \frac{\partial (\tilde{\rho}\tilde{u}^2 + \tilde{p})}{\partial \tilde{x}} = 0 \tag{2.2}$$

$$\frac{\partial (\tilde{\rho}(\tilde{e} + \frac{\tilde{u}^2}{2} + \tilde{q}))}{\partial \tilde{t}} + \frac{\partial [\tilde{\rho}\tilde{u}(\tilde{e} + \frac{\tilde{u}^2}{2} + \frac{\tilde{p}}{\tilde{\rho}} + \tilde{q})]}{\partial \tilde{x}} = 0 \tag{2.3}$$

where $\tilde{\rho}$ is the density, $\tilde{u}$ the velocity, $\tilde{p}$ the pressure, $\tilde{e}$ the specific internal energy, and $\tilde{q}$ the residual chemical energy available in the mixture. The tilde here denotes a dimensional variable.

For simplicity, we assume a calorically perfect gas, giving:

$$\tilde{p} = \tilde{\rho} R \tilde{T} \tag{2.4}$$

where R is the ideal gas constant, and $\tilde{T}$ the temperature, and the equation of state for specific internal energy is:

$$\tilde{e} = \frac{\tilde{p}}{(\gamma - 1)\tilde{\rho}} \tag{2.5}$$

where γ is the ratio of specific heats, and the acoustic speed is:

$$\tilde{c} = \sqrt{\frac{\gamma \tilde{p}}{\tilde{\rho}}} \tag{2.6}$$

The governing equations together with the perfect gas assumption gives us three

equations with the four variables, $\tilde{\rho}, \tilde{p}, \tilde{u}, \tilde{q}$.

2.2 - The Chemical Model

A two-step chemical model will be used in order to close the governing system of equations. The two step model consists of two components: a temperature sensitive induction zone in which no heat is released, and a temperature independent exothermic reaction zone. The chemistry is governed by the equations:

$$\frac{D\lambda_i}{D\tilde{t}} = -H(\lambda_i) K_i \exp\left(\frac{-\tilde{E}}{R\tilde{T}}\right) \tag{2.7}$$

$$\frac{D\lambda_e}{D\tilde{t}} = (1 - H(\lambda_i)) K_e (1-\lambda_e)^{\nu} \tag{2.8}$$

where λ_i is the progress variable for the induction zone, λ_e the progress variable for the reaction zone, K_i a scaling parameter adjusted so that the induction zone length is unity, $\tilde{E}$ the activation energy controlling the temperature sensitivity of the induction zone duration, K_e a reaction rate constant, and ν the reaction order of the reaction zone, and $H(\xi)$ is the Heaviside function:

$$H(\xi) = \begin{cases} 1 & , \xi > 0 \\ 0 & \xi \le 0 \end{cases} \tag{2.9}$$

Since all the heat is liberated in the reaction zone, the residual chemical heat, $\tilde{q}$, can be written in terms of the reaction progress variable:

$$\tilde{q} = \lambda_e \tilde{Q}$$

where $\tilde{Q}$ represents the total chemical energy available in the unreacted gas.

The chemical model will be discussed in more detail below in the discussion on the steady state structure.

2.3 - Scalings

In the numerical simulations in this study, the flow variables have been scaled with the post shock density and pressure:

$$\rho = \frac{\tilde{\rho}}{\tilde{\rho}_s}, \quad p = \frac{\tilde{p}}{\tilde{p}_s}, \quad T = \frac{\tilde{T}}{R\tilde{T}_s}, \quad u = \frac{\tilde{u}}{\sqrt{R\tilde{T}_s}}, \quad c = \frac{\tilde{c}}{\sqrt{R\tilde{T}_s}}$$

where the *s* subscript denotes the post shock state.

The scaling parameter, K_i, is adjusted so that the induction zone length, Δ_i, is unity. This gives the length and time scaling:

$$x=\frac{\tilde{x}}{\Delta_i}, \quad t=\frac{\tilde{t}}{\Delta_i/\sqrt{R\tilde{T}_s}}$$

The activation energy and heat release have been scaled by the post shock temperature. The non dimensional activation energy and heat release, E and Q, are:

$$E=\frac{\tilde{E}}{R\tilde{T}_s}, \quad Q=\frac{\tilde{Q}}{R\tilde{T}_s}$$

2.4 - The Chapman-Jouguet (CJ) solution

The governing equations, (2.1)-(2.3) admit a steady state solution (Fickett and Davis 1979). By treating the detonation structure as a discontinuity and assuming steady state, the conservation laws can be rewritten in the form:

$$\tilde{\rho}_b\tilde{u}'_b=\tilde{\rho}_o\tilde{u}'_o \tag{2.10}$$

$$\tilde{\rho}_b\tilde{u}_b^2+\tilde{p}_b=\tilde{\rho}_o\tilde{u}_o^2+\tilde{p}_o \tag{2.11}$$

$$\frac{\gamma}{\gamma-1}\frac{\tilde{p}_b}{\tilde{\rho}_b}+\frac{1}{2}\tilde{u}_b^2+\tilde{Q}=\frac{\gamma}{\gamma-1}\frac{\tilde{p}_o}{\tilde{\rho}_o}+\frac{1}{2}\tilde{u}_o^2 \tag{2.12}$$

where the *b* subscript represents the burnt state at the rear of the reaction zone, and the *o* subscript represents the unburnt state upstream of the shock. The velocities, u'_o and u'_b, represent the velocities in the reference frame of the leading shock. The primes denote quantities in the shock fixed frame and can be transformed from the lab frame under the transformation:

$$u'=u-D_{CJ} \tag{2.13}$$

$$x'=x-D_{CJ}t \tag{2.14}$$

where D_{CJ} is the detonation velocity.

By manipulating (2.10)-(2.12), a steady state solution can be found such that the flow velocity of the reacted state behind the reaction zone is exactly sonic relative to the leading shock (Fickett and Davis 1979). Such a solution is called the Chapman-Jouguet

(CJ) solution.

The Mach number of the CJ wave is given by:

$$M_{CJ}=\sqrt{(1+\frac{\gamma^2-1}{\gamma}\frac{\tilde{Q}}{R\tilde{T}_o})+\sqrt{(1+\frac{\gamma^2-1}{\gamma}\frac{\tilde{Q}}{R\tilde{T}_o})^2-1}} \tag{2.15}$$

and the CJ state behind the reaction zone is given by:

$$\frac{\tilde{p}_{CJ}}{\tilde{p}_o}=\frac{1+\gamma M_{CJ}^2}{\gamma+1} \tag{2.16}$$

$$\frac{\tilde{\rho}_{CJ}}{\tilde{\rho}_o}=\frac{M_{CJ}^2(\gamma+1)}{1+\gamma M_{CJ}^2} \tag{2.17}$$

$$\frac{\tilde{u}'_{CJ}}{\tilde{c}_o}=\frac{M_{CJ}-M_{CJ}^{-1}}{\gamma+1} \tag{2.18}$$

The CJ solution above for the Mach number and the rear burnt state is independent of the reaction rate. However, (2.15)-(2.18) give no information about the structure of the reaction zone

2.5 - The Steady State Structure

The steady state structure of the detonation, also called the Zel'dovich-Neumann-Doring (ZND) solution, can be obtained given a rate law for the chemical reactions, as in (2.7) and (2.8).

Using the Rankine-Hugoniot shock jump conditions (Liepmann and Roshko 1957):

$$\frac{\tilde{\rho}_s}{\tilde{\rho}_o}=\frac{\tilde{u}'_o}{\tilde{u}'_s}=\frac{(\gamma+1)M_{CJ}^2}{(\gamma-1)M_{CJ}^2+2} \tag{2.19}$$

$$\frac{\tilde{p}_s-\tilde{p}_o}{\tilde{p}_o}=\frac{2\gamma}{\gamma+1}(M_{CJ}^2-1) \tag{2.20}$$

the post-shock conditions can be obtained knowing the upstream state and the Mach number of the shock, given in (2.15).

Starting with the post shock state, where $\tilde{\rho}=\tilde{\rho}_s$, $\tilde{p}=\tilde{p}_s$, $\tilde{u}'=\tilde{u}'_s$, $\lambda_i=1$, $\lambda_e=0$, the rate law, (2.7) and (2.8), can be integrated until the end of the reaction zone, when λ_e

reaches 1.

Figure 2.1 and *2.2* show the ZND profiles for the temperature and reaction progress variables (λ_i and λ_e) respectively for various values of K_e. The induction zone, described by (2.7), is of Arrhenius form with no heat release and the temperature stays constant, as can be seen in *Figure 2.1.* The progress variable, λ_i, is 1 at the leading shock and the reaction proceeds until λ_i reaches 0, as seen in *Figure 2.2.* At $\lambda_i = 0$, $H(\lambda_i)$ in (2.7) acts as a switch that terminates the induction zone. When $\lambda_i = 0$, the induction zone ends, triggering the start of the reactions in the reaction zone, as seen in *Figure 2.2.*

The exothermic reaction zone, described by (8), is not sensitive to changes in temperature. For $\lambda_i > 0$, $(1-H(\lambda_i))=0$ and the reaction rate of the reaction zone is 0. The exothermic reaction proceeds as soon as the induction zone ends ($\lambda_i = 0$) as shown in *Figure 2.2.* In this second step of the chemical reaction, all of the heat is liberated. The term K_e is a rate constant that controls the reaction rate, and an increase in K_e causes a shortening of the reaction zone, as can be seen in *Figure 2.1.*

2.6 - Characteristics Curves

In compressible flows, weak compression and expansion waves travel at the local sound speed and are convected by the flow. The trajectories of these pressure waves can be expressed (in non-dimensional parameters):

$$\frac{dx}{dt}=u+c \tag{2.21}$$

$$\frac{dx}{dt}=u-c \tag{2.22}$$

(2.21) and (2.22) correspond to the C+ and C- characteristics respectively, representing the path that pressure waves travel along in the positive and negative x direction. The positive x direction is taken in the direction of detonation propagation.

A third family of characteristics, C0, exists:

$$\frac{dx}{dt}=u \tag{2.23}$$

describing the path of a fluid particle. A more detailed account of characteristics can be

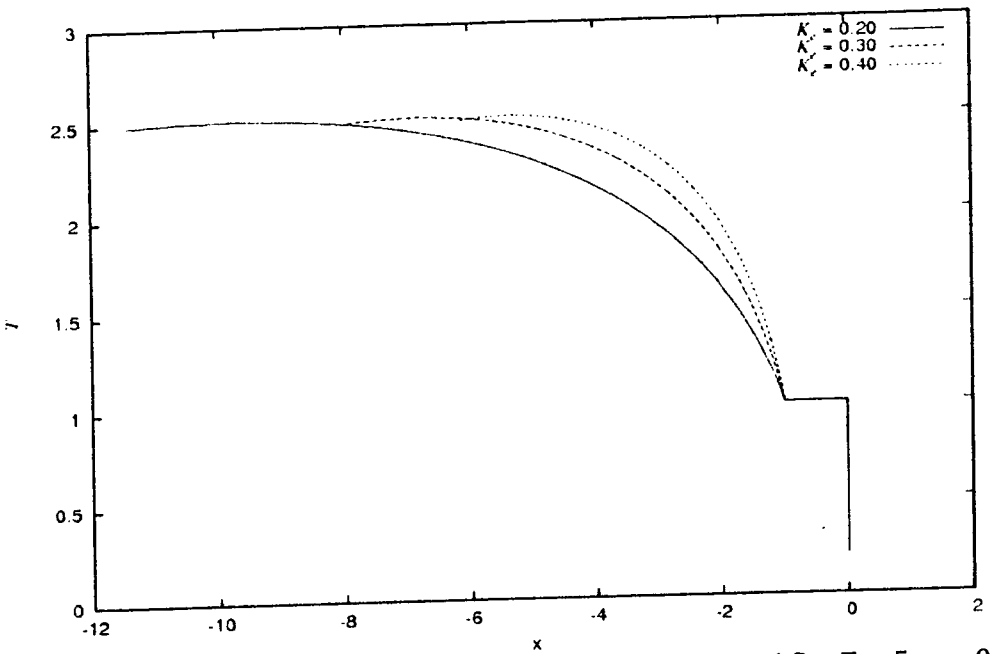

Figure 2.1 - ZND temperature profiles for Q = 10.3875, γ=1.2, E = 5, ν = 0.5

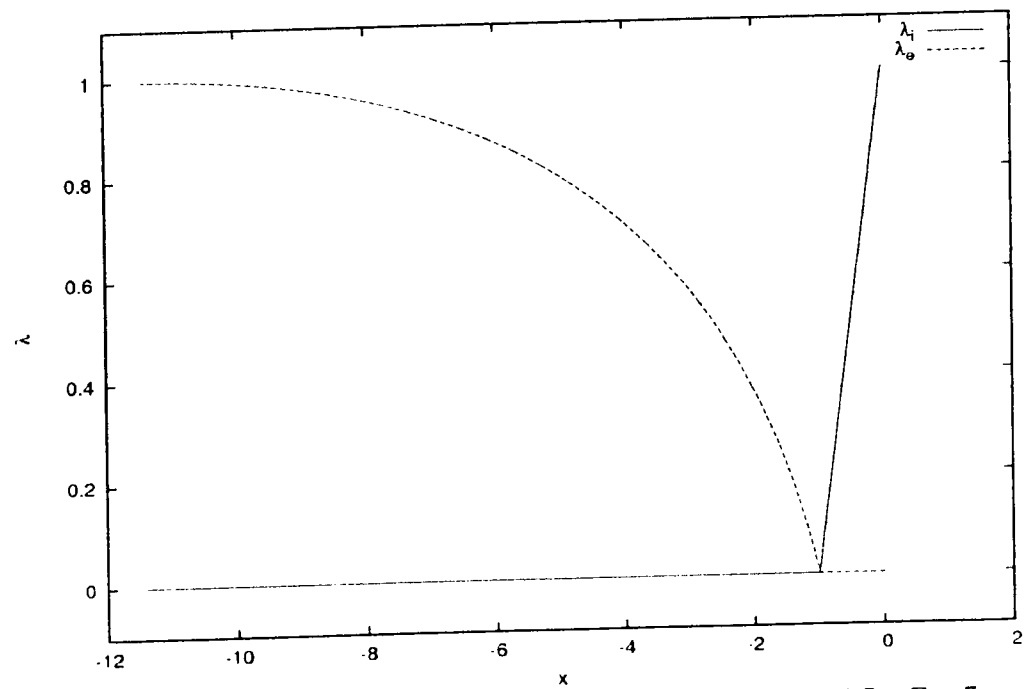

Figure 2.2 - *ZND* progress variable profiles for Q = 10.3875, γ=1.2, E = 5, ν = 0.5, K_e = 0.20

found in Whitham (1974).

The family of C+ characteristics for a stable CJ detonation is shown in *Figure 2.3.* Note that since the flow at the rear of the reaction zone is sonic relative to the leading shock, $u + c$ is exactly 0 in the reference frame of the shock, and hence the characteristics behind the reaction zone can never catch up to the leading shock. This shows that for a steady CJ detonation, pressure waves originating from behind the reaction zone will never catch up to the leading shock, as shown in *Figure 2.3.*

In reality, detonations are unstable and the steady state solution is rarely seen. Tracking the characteristic paths in unsteady detonation solutions will permit us to study how pressure waves propagate across the reaction zone structure, giving a clearer picture of the pulsating dynamics.

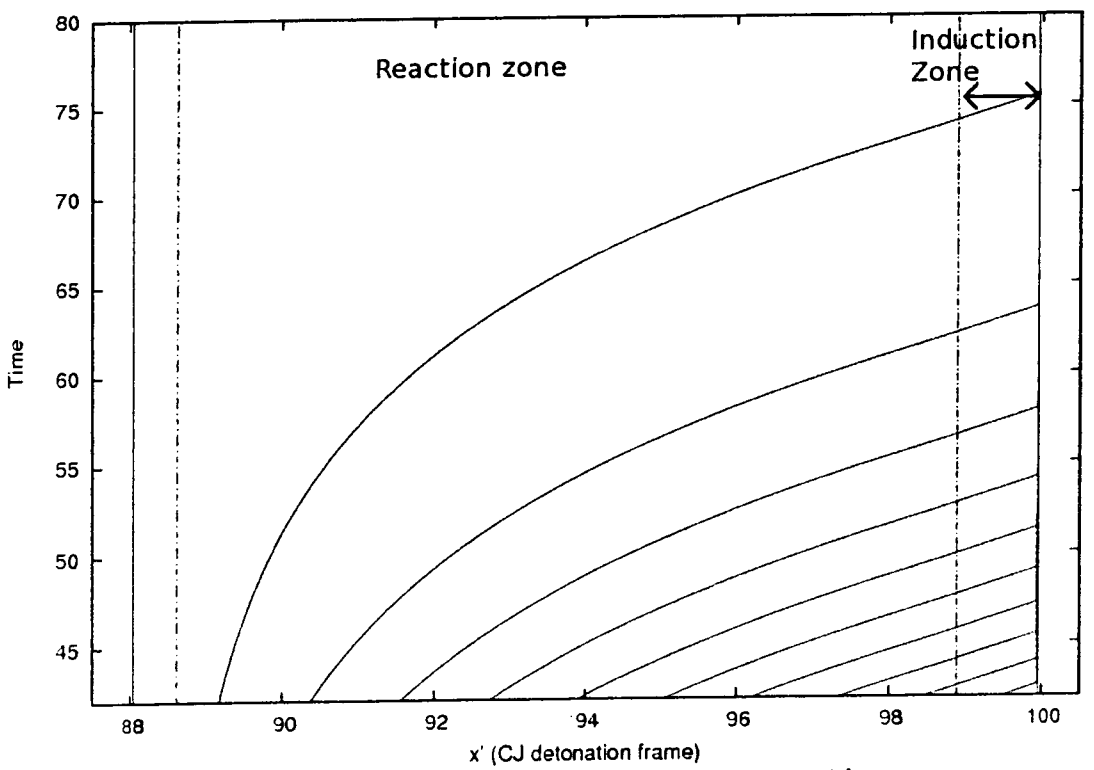

Figure 2.3 - Family of C+ characteristics for a stable detonation, with parameters Q = 10.3875, γ = 1.2, E = 5, ν = 0.5, K_e = 0.20. Characteristics originating from the burnt region do not catch up to the reaction zone

Chapter 3

Numerical Method

The numerical simulations in this study were performed using the AMRITA system developed by J.J. Quirk (1998). It is a computational engine driven through its own scripting language. AMRITA is a system designed for automating and archiving computational studies, allowing for easy reproducibility and reliability of numerical investigations. To save on computational expense, AMRITA features an adaptive mesh refinement scheme that uses a tiered grid system, $G = \{G_0, G_1, \ldots, G_{lmax}\}$ where G_0, the coarsest grid, covers the entire computational domain, while the finer subgrids are employed in specified areas requiring further refinement.

The numerical simulations were run using a linearized Riemann solver based on Roe's scheme, which computes the governing equations in the lab frame. An example AMRITA script can be found in *Appendix B*. Roe's scheme is detailed in (Roe 1981).

The two-step model was implemented by modifying the existing routines for the three-step chain branching model used by Short and Quirk (1997). The equations contained in the routines for the source term, partial derivatives and computation of the ZND profile were changed to fit the equations of the two-step model presented in Chapter 2. The modified routines can be found in *Appendix C*.

The simulations were run on a computational domain of 8,000-16,000 induction lengths, with a mesh spacing of 1 induction length on the coarsest grid level. The refinement criteria used are:

$$x > x_r - 10 \text{ and } \rho > 1.1\,\rho_o \tag{3.1}$$

$$\rho_+ - \rho > 0.001 \text{ and } \lambda_1 > 0.99 \tag{3.2}$$

$$p_+ - p > 1 \tag{3.3}$$

where x_r is the location of the end of the reaction zone, ρ_o is the upstream density, ρ and p are the values of the density and pressure for a given cell, respectively, and ρ_+ and p_+ the value of the density and pressure of a neighbouring cell in the positive x direction. The positive direction is in the direction of detonation propagation.

The simulation checks conditions (3.1)-(3.3) for every cell, and for each cell that satisfies one of (3.1)-(3.3), refinement is provided and a finer subgrid is used for both the current cell and its neighbouring cells. A refinement factor of 2 was used in this study, giving a mesh spacing of $1/2^i$ for the ith grid level. Condition (3.1) provides refinement for all cells from 10 induction lengths behind the reaction zone to the point where the density is 1.1 times larger than the unreacted upstream density. This insures adequate refinement everywhere within the detonation structure, taking special care to properly refine the rear of the reaction zone. Conditions (3.2) and (3.3) are to insure refinement ahead of the leading shock such that the shock structure is always captured on the finest grid. A sketch of the refinement conditions is shown in *Figure 3.1*.

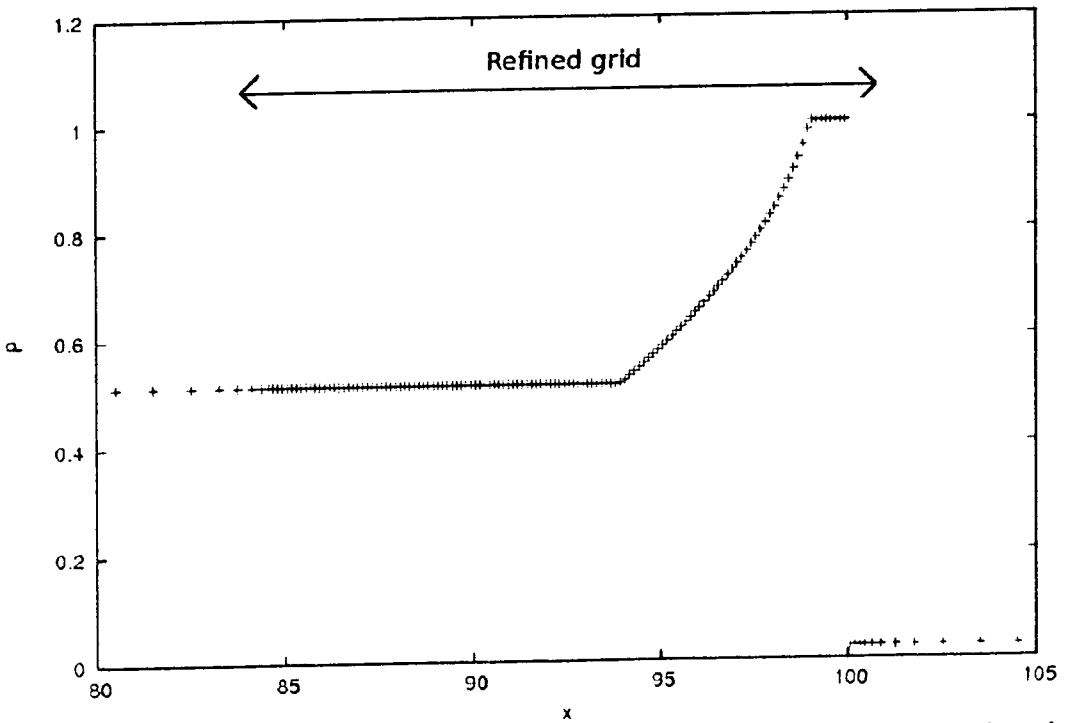

Figure 3.1 - Sketch of grid refinement with a resolution of 8 points per induction length on the finest grid

The simulations were initialized by imposing the ZND solution onto the domain, with the leading shock placed 100 induction lengths away from the rear boundary, where the rear boundary is in the direction opposite of detonation propagation, and the front boundary is in the direction of the detonation propagation. The rear boundary condition was prescribed at the CJ solution behind the reaction zone. For the front boundary, a zeroth order extrapolation of the interior points was performed, and thus treated as an outflow. Note that the domain size and duration of the simulation is chosen so that detonation wave never reaches the front boundary and hence there is no flow at the front boundary. All simulations were run using a CFL number of 0.4.

3.1 - Construction of the Families of Characteristics

The families of characteristic curves can be described by the equations (2.21)-(2.23), describing the C+ curves, C- curves, and C0 (or particle paths) respectively. The C+ characteristics represent the path of compression or expansion waves traveling in the direction of the leading shock, and the C- characteristics represent the waves traveling in the opposite direction of the leading shock. The sound speed is $c=\sqrt{\frac{\gamma P}{\rho}}$.

At the beginning of the simulations, the origin of the three sets of characteristics (the C+ characteristics, C- characteristics, and particle paths) were created at discrete locations. A linear interpolation was used to find the values of $u+c$, $u-c$, and u at each location point for each of the characteristics. The equations (2.21)-(2.23) were then integrated using an explicit first order discretization to find the location of each characteristic at the next time step. The process was then repeated for each time step until the end of the simulation.

The integration above was performed in the lab frame. However, in this work, the characteristics were transformed into the shock frame using (2.13) and (2.14) and plotted on an x-t diagram in the shock frame for visual clarity.

The integration described above is performed in post-processing, thus the reconstruction of the characteristics does not affect the results of the numerical

simulations.

3.2 Convergence Study

A set of resolution studies were performed. The onset of stability was found for each set of parameters by adjusting the reaction rate parameter, K_e until the transition from the stable to unstable regime (or the stability boundary) was found. The number of grid levels and the stability boundary was found for higher resolutions until a grid converged solution for the stability boundary was obtained. The model parameters used in the convergence study were Q = 10.3875, v = 0.5, γ=1.2, and the stability boundary for various resolutions is shown in *Table 3.1*.

Table 3.1 - Stability boundary for various resolutions for Q = 10.3875, v = 0.5, γ=1.2

Points per induction length	E = 5 K_e	E = 10 K_e
32	0.36	0.15
64	0.37	0.15
128	0.37	0.15
256	0.37	0.15

Table 3.1 indicates that a resolution of 64 points per induction length on the most refined grid is sufficient for a grid converged value for the stability boundary at E = 10. At E = 5, a resolution of 128 points per induction length on the most refined grid is sufficient for a converged value of the stability boundary.

Figure 3.2 shows the shock pressure history for the long-term oscillations for E = 10. For all of the resolutions shown, the amplitude is approximately 1.06, and the period of oscillation is approximately 98. A resolution of 64 points per induction length is sufficient in obtaining a grid converged solution for the amplitude, period, and stability boundary for E = 10.

Figure 3.3 shows the shock pressure history for a long-term pulsation for E = 5. For 32 points per induction length, only smooth low frequency pulsations are observed,

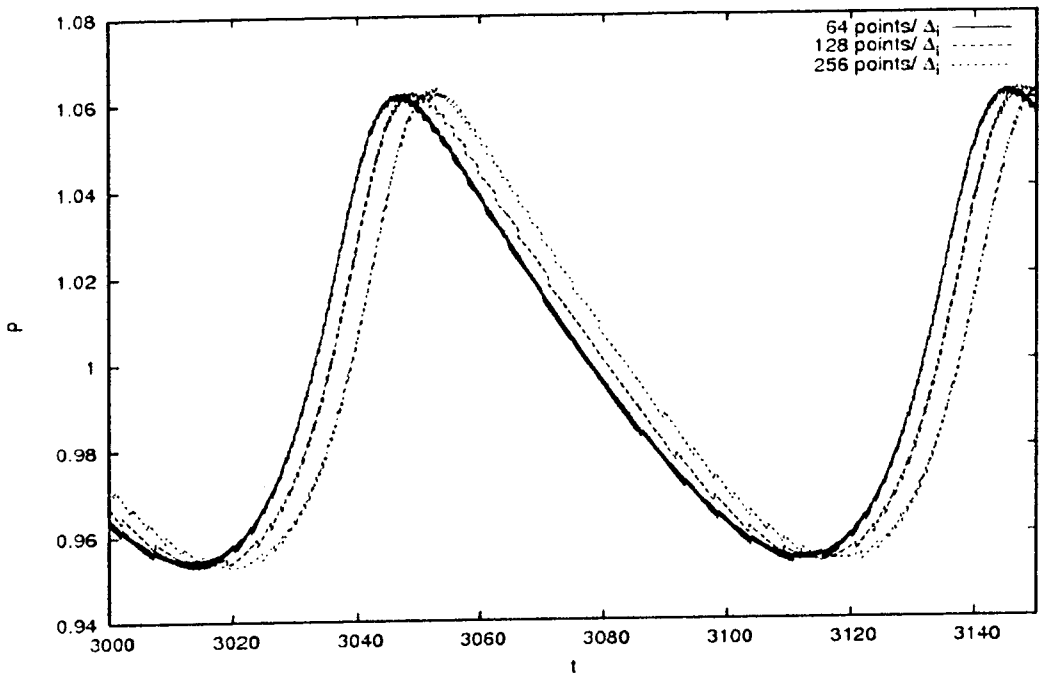

Figure 3.2 - Shock pressure history for $E = 10$, $\upsilon = 0.5$, $\gamma = 1.2$ and $K_e = 0.15$ at various resolutions

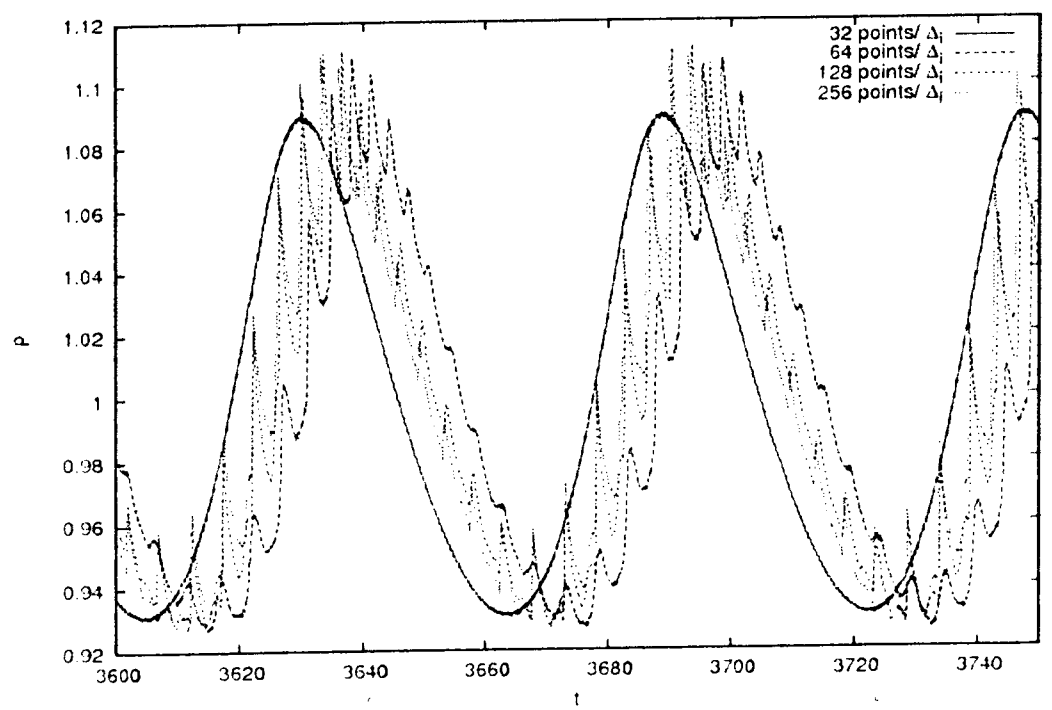

Figure 3.3 - Shock pressure history for $E = 5$, $\upsilon = 0.5$, $\gamma = 1.2$ and $K_e = 0.37$ at various resolutions

whereas for resolutions of 64 points per induction length or higher, low and high frequency oscillations are simultaneously seen. *Figure 3.3* indicates that a resolution of 128 points per induction length is sufficiently accurate in obtaining a grid converged stability boundary and in capturing both frequencies of pulsation.

In this study, a resolution of 128 points per induction length corresponding to 7 grid levels will be used to insure that the pulsating dynamics are properly resolved.

3.3 - Comparison with previous results

The code used in this study was benchmarked with the results obtained by Short and Sharpe (2003) for the stability boundary. The scalings used in this study differ from those used by Short and Sharpe, and the conversion between the scalings is detailed in *Appendix A*.

The stability boundary found in this study and by Short and Sharpe are shown in *Table 3.2* in terms of the scalings used in this work. Short and Sharpe used the parameters $\gamma = 1.4$, $Q = 1.6988$, $\nu = 0.5$, and found the stability boundary for a given activation energy, E, by varying K_e. The resolution used by Short and Sharpe typically corresponded to 256 points for the detonation length. In contrast, the resolution used in this study was 128 points per induction length. For parameters $E = 10$, $\gamma = 1.4$, $Q = 1.6988$, $\nu = 0.5$, the ZND profile is 5.647 induction lengths long, corresponding to 723 points over the detonation reaction zone length.

Very good agreement was found between the results generated by this work and those generated by Short and Sharpe.

Table 3.2 - Stability boundary (scalings are with respect to those used in this paper)

E	K_e *(Short and Sharpe)*	K_e *(this work)*
10.0	0.414	0.416
12.5	0.314	0.314
25.0	0.142	0.141

Chapter 4

Results and Discussion

Using the numerical method described in Chapter 3, a parametric study was performed to first obtain the stability boundary as activation energy, E, and heat release, Q, were varied over a wide interval. After the stability boundary was obtained for each set of parameters, the pulsating dynamics close to the stability boundary were studied using the family of characteristic curves.

In all of the figures shown in this section, all quantities are in terms of non-dimensional scalings defined in Section 2.3.

4.1 - The Stability Boundary

The stability boundary was found for various activation energy, E, and heat release, Q. The specific heat ratio, γ, and the reaction order, ν, were kept constant at 1.2 and 0.5 respectively. For simplicity, small variations in γ as the mixture reacts are not taken into account in this work and can be considered in future work. For each set of parameters, the stability boundary was determined by varying the reaction rate constant, K_e, and finding the value below which the detonation becomes stable. Many of the simulations were run for time t = 5,000. However, for various parameters, this time interval was unable to capture the saturation of pulsating dynamics into a limit cycle. For these parameters, the simulation was allowed to run until the pulsations saturated at a final amplitude. A map of the stability results can be found in *Table 4.1*. *Figure 4.1-4.4* show ZND profiles at the stability boundary for four different activation energies at a fixed heat release. The shock pressure histories close to the stability boundary for each set of parameters are shown in *Appendix F*.

4.1.1 - The Stability Parameter, χ

Previous work has shown that the stability boundary of a pulsating detonation is well correlated by the stability parameter $\chi = E(\Delta_i/\Delta_e)$ (Radulescu 2003; Short and Sharpe 2003; [b]Ng. et al 2005). However, there is no standard definition for Δ_e. Ng et al estimated the reaction zone length as:

$$\Delta_e = \frac{u'_{CJ}}{\dot{\sigma}_{max}} \tag{4.1}$$

where $\dot{\sigma}$ is the thermicity, defined as:

$$\dot{\sigma} = \frac{(\gamma-1)}{\gamma}\frac{\tilde{Q}}{R\tilde{T}_o}\frac{D\lambda_e}{Dt} \tag{4.2}$$

which represents a normalized heat release rate. The inverse of the thermicity gives a characteristic time scale for heat release, which is then used to compute the reaction zone length in (4.1). The reaction length described by (4.1) gives a characteristic length scale over which most of the heat is released. The definition of the reaction length defined above is general enough that it can easily be calculated for detailed chemical kinetic models. Calculation of the maximum thermicity is detailed in *Appendix E.*

4.1.2 Stability Boundary Results

In the stability results summarized in *Table 4.1*, the stability boundary is shown for each set of activation energy and heat release, and the stability parameter was calculated using the definition of the reaction length given by (4.1). *Table 4.1* shows that at the stability boundary, for a fixed Q, as E is increased, K_e decreases (and hence the ratio Δ_i/Δ_e decreases and the reaction zone becomes long relative to the induction zone). *Table 4.1* indicates that the stability boundary is roughly correlated with the stability parameter at $\chi \sim 10$. *Figures 4.1-4.4* show visually that at a fixed Q, increasing the activation energy leads to a longer reaction zone at the stability boundary.

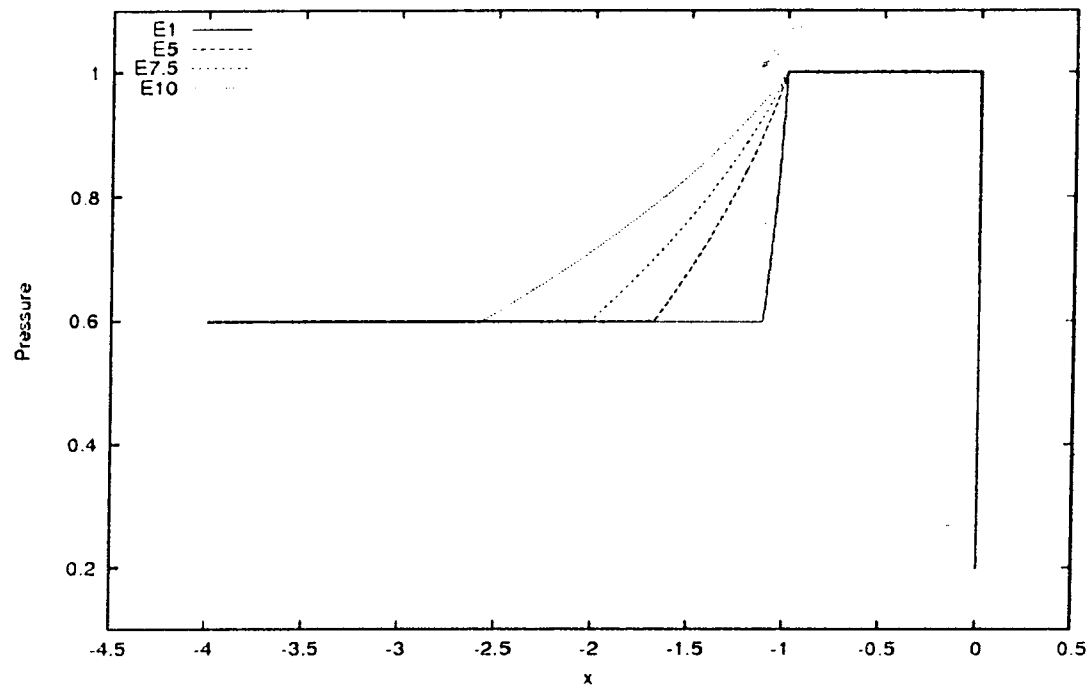

Figure 4.1 - ZND profiles for Q = 2.789 at the stability boundary specified by *Table 4.1*

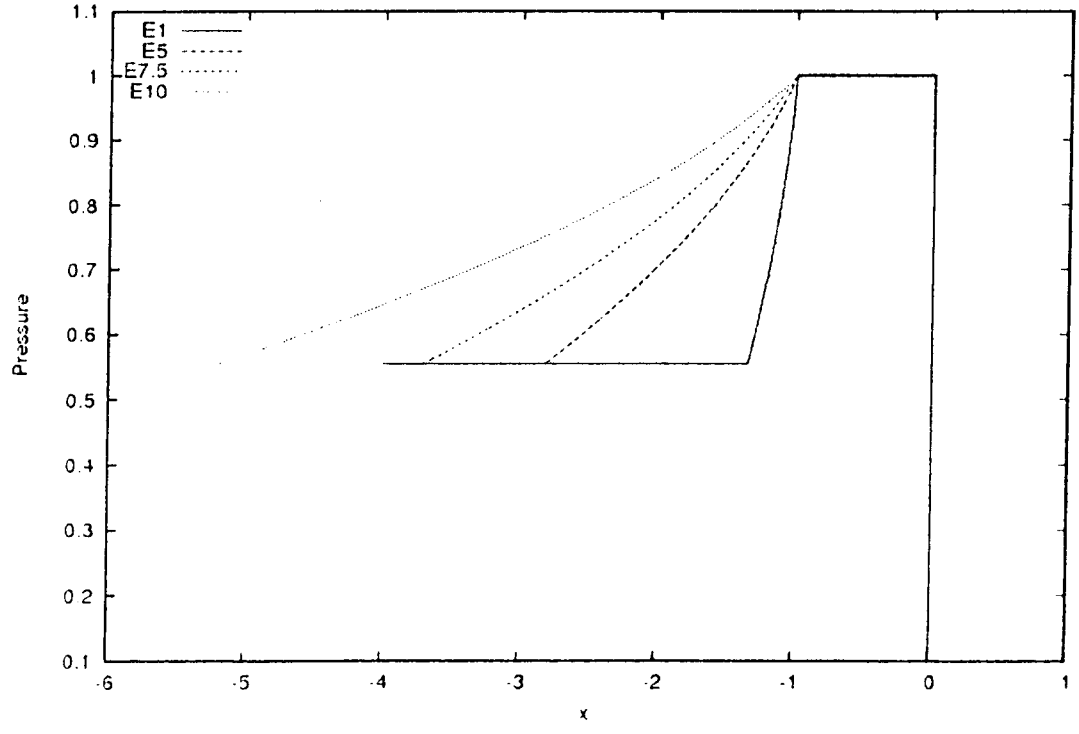

Figure 4.2 - ZND profiles for Q = 5.000 at the stability boundary specified by Table 4.1

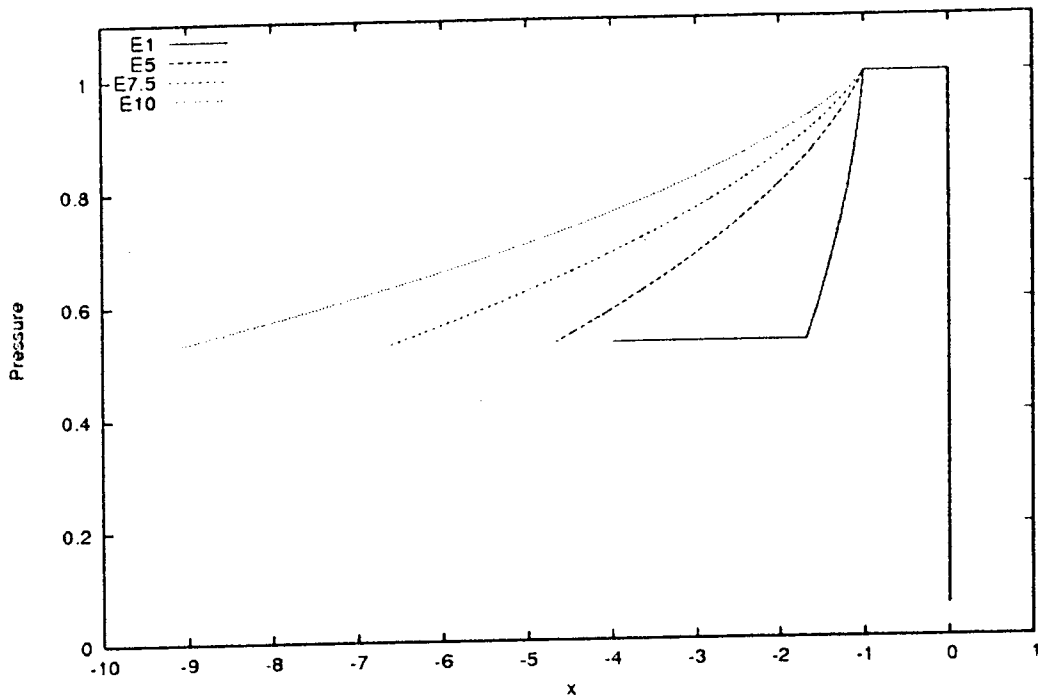

Figure 4.3-ZND profiles for Q = 7.500 at the stability boundary specified by *Table 4.1*

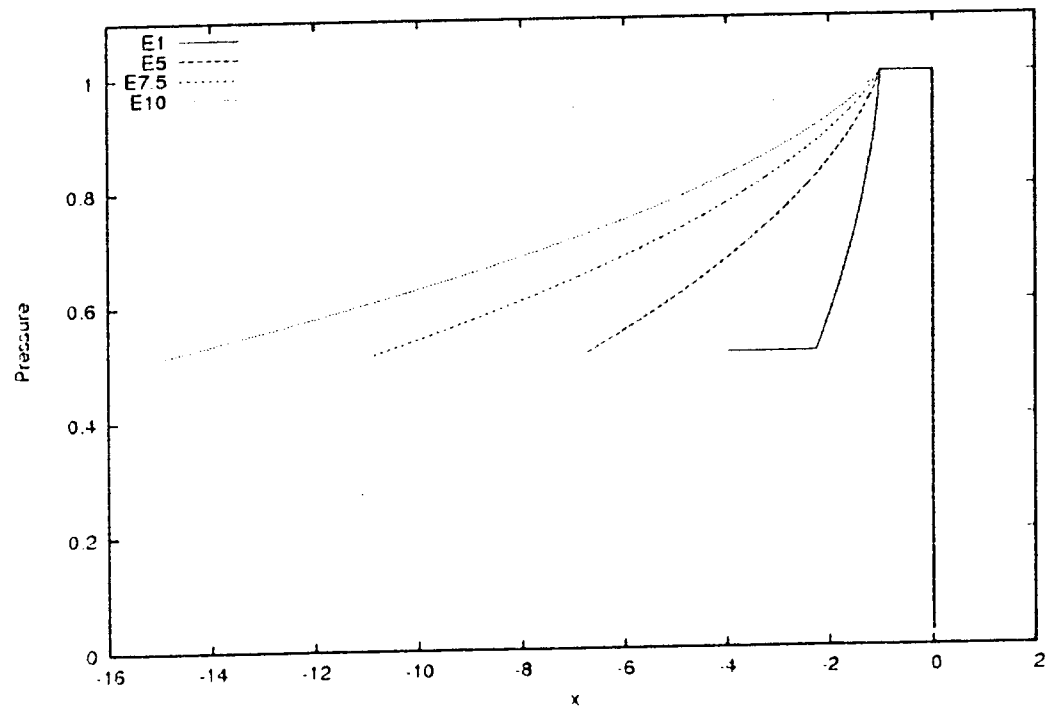

Figure 4.4-ZND profiles for Q = 10.3875 at the stability boundary specified by *Table 4.1*

Table 4.1 - Stability boundary for various values of E and Q

E \ Q	2.789	5.000	7.500	10.3875
1	K_e = 15.94 χ = 14.92	K_e = 5.66 χ = 9.02	K_e = 2.89 χ = 7.97	K_e = 1.66 χ = 10.07
5	K_e = 2.68 χ = 12.55	K_e = 1.04 χ = 8.29	K_e = 0.54 χ = 7.44	K_e = 0.36 χ = 10.91
7.5	K_e = 1.81 χ = 12.71	K_e = 0.70 χ = 8.37	K_e = 0.35 χ = 7.24	K_e = 0.21 χ = 9.55
10	K_e =1.18 χ = 11.05	K_e = 0.45 χ = 7.17	K_e = 0.24 χ = 6.62	K_e = 0.15 χ = 9.10

4.2 - Pulsation Regimes Near the Stability Boundary

For the 16 different sets of parameters tested in this study, four distinct pulsating regimes are identified at the stability boundary: the *very high frequency, high frequency, low frequency* and *transition* regime. A summary of the pulsating characteristics of each set of parameters is given in *Table 4.2*, and the corresponding shock pressure histories shown in *Appendix F.* For low activation energy (E = 1), rapid very high frequency pulsations with a period of oscillation of less than one induction time are seen. A sample shock pressure history of the very high frequency regime is shown in *Figure 4.11* in Section 4.4. For high activation energy (E = 10), low frequency pulsations, typically with a period of greater than 18 induction times are seen. A sample shock pressure history of the very high frequency regime is shown in *Figure 4.19* in Section 4.5. For moderate activation energy (E = 5 and 7.5) and low heat release, high frequency pulsations are seen, as shown by *Figures 4.7* in Section 4.3. The shock pressure evolution of the high frequency pulsations appear similar to the very high frequency pulsations but have a period of 1-2 induction times. As heat release is further increased, a transition regime is seen, where high frequency pulsations are seen in the early time and eventually transition into a low frequency mode of pulsation. *Figure 4.5.1* shows the transition regime in which the low frequency mode of pulsation is seen in the long-time solution. Figure 4.5.2 show similar behaviour in the early time. However, in the late time solution, both the

high frequency mode and low frequency mode are present simultaneously.

Very high frequency, high frequency and low frequency modes of pulsations have been identified. The transition from high to low frequency pulsations resembles the results of Daimon and Matsuo (2007) in their numerical simulations of hydrogen detonations using realistic chemical kinetics. Thus, the two-step model appears to capture the complexities observed in unstable detonations while keeping the model very simple.

In the following sections, the physical mechanisms controlling the high, very high and low frequency regimes of pulsation will be examined.

Table 4.2 - Pulsating characteristics and period of oscillation (in terms of induction times)

E	*Q*	2.789	5.000	7.500	10.3875
1	Characteristic	Very high frequency	Very high frequency	Very high frequency	Very high frequency
	Period	0.67	0.57	0.78	0.72
5	Characteristic	High frequency	High frequency	High frequency	Transition (both modes present in long-time)
	Period (high frequency)	2.00	1.73	1.57	1.43
	Period (low frequency)				21.4
7.5	Characteristic	High frequency pulsations	Transition (both modes present in long-time)	Transition (low frequency in the long-time)	Transition (low frequency in the long-time)
	Period (high frequency)	2.02	1.71	1.58	1.46
	Period (low frequency)		19.4	23.4	27.9
10	Characteristic	Low frequency	Low frequency	Low frequency	Low frequency
	Period	18.3	23.4	28.0	34.5

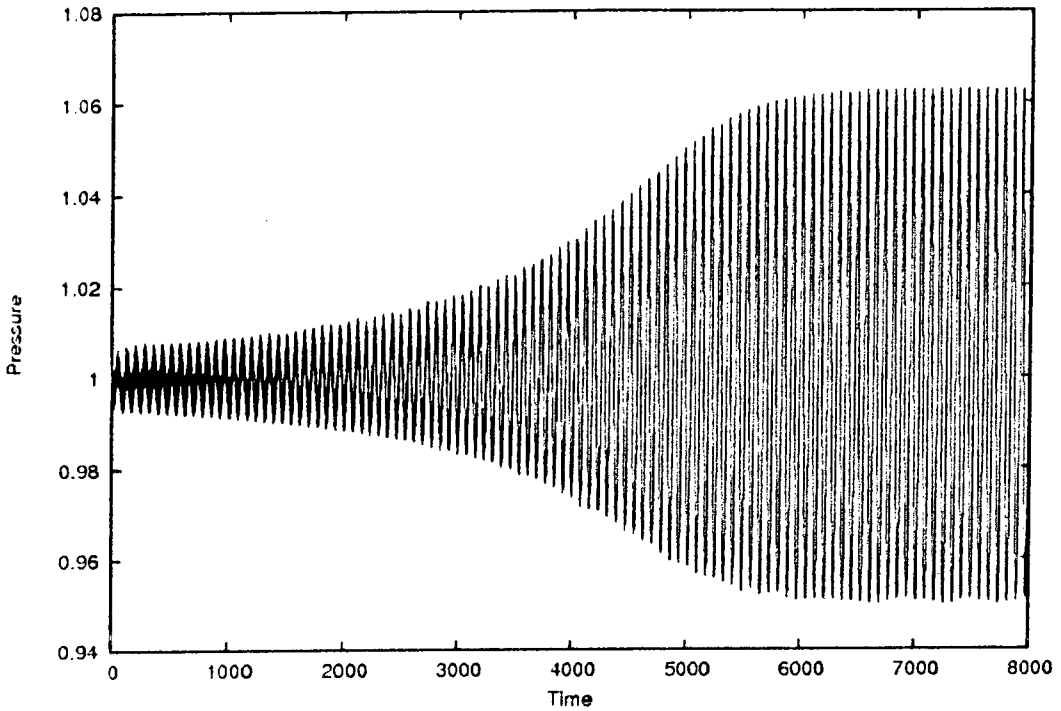

Figure 4.5.1a - Shock pressure history for Q = 10.3875, E = 7.5, K_e = 0.21

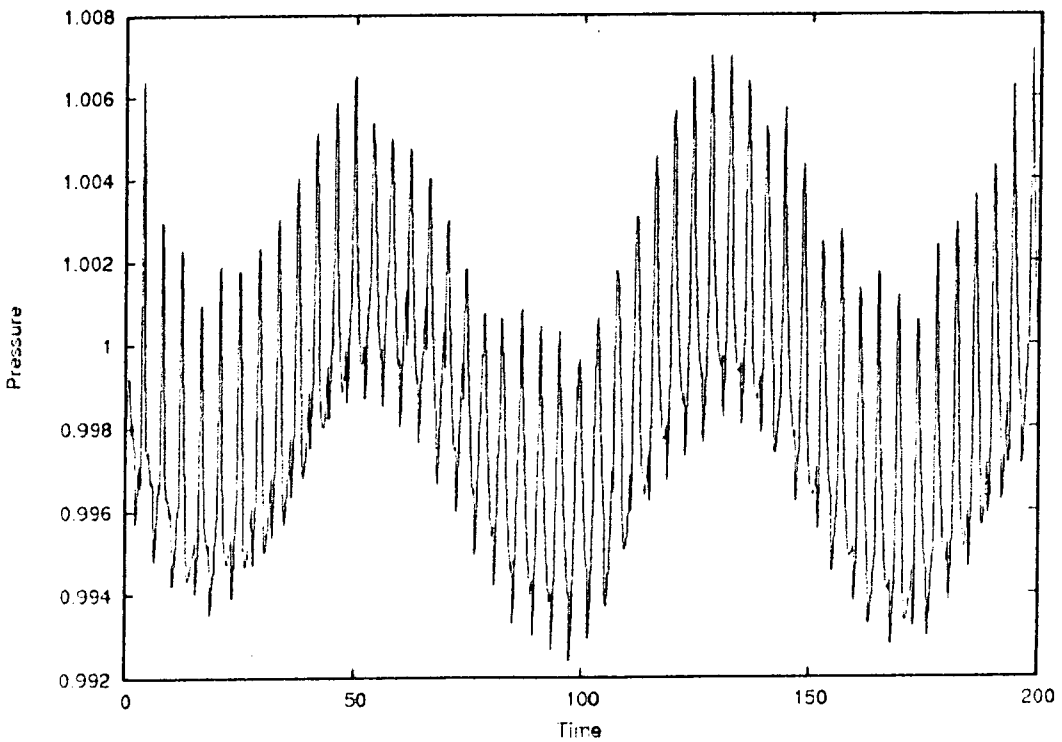

Figure 4.5.1b - Shock pressure history for Q = 10.3875, E = 7.5, K_e = 0.21

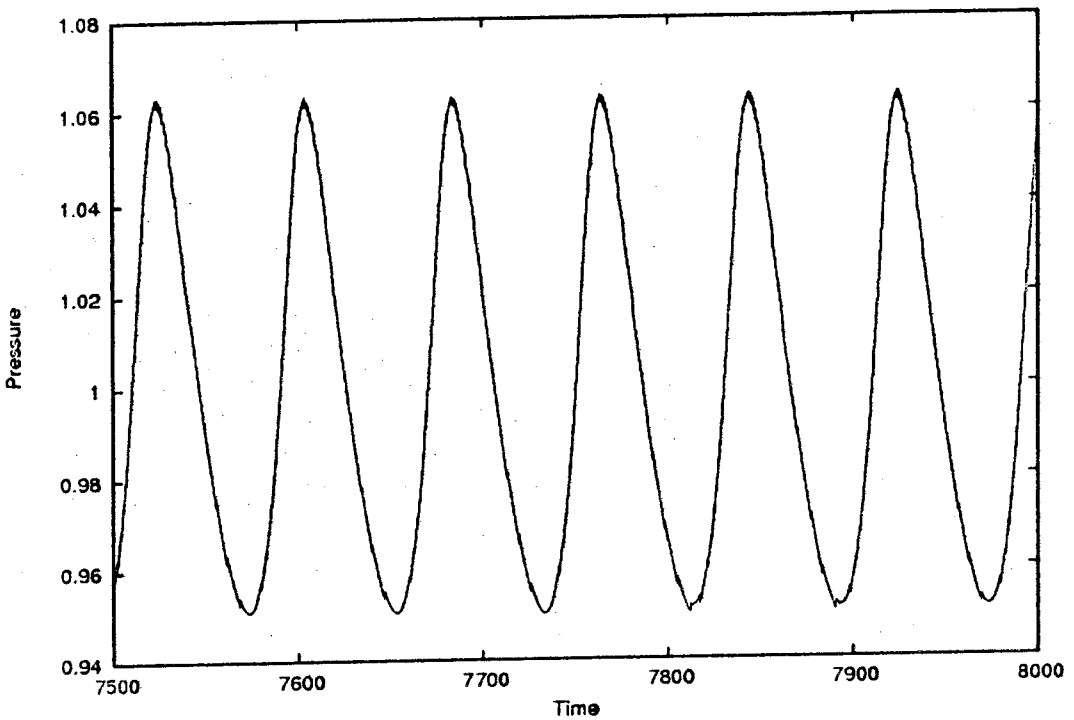

Figure 4.5.1c - Shock pressure history for Q = 10.3875, E = 7.5, K_e = 0.21

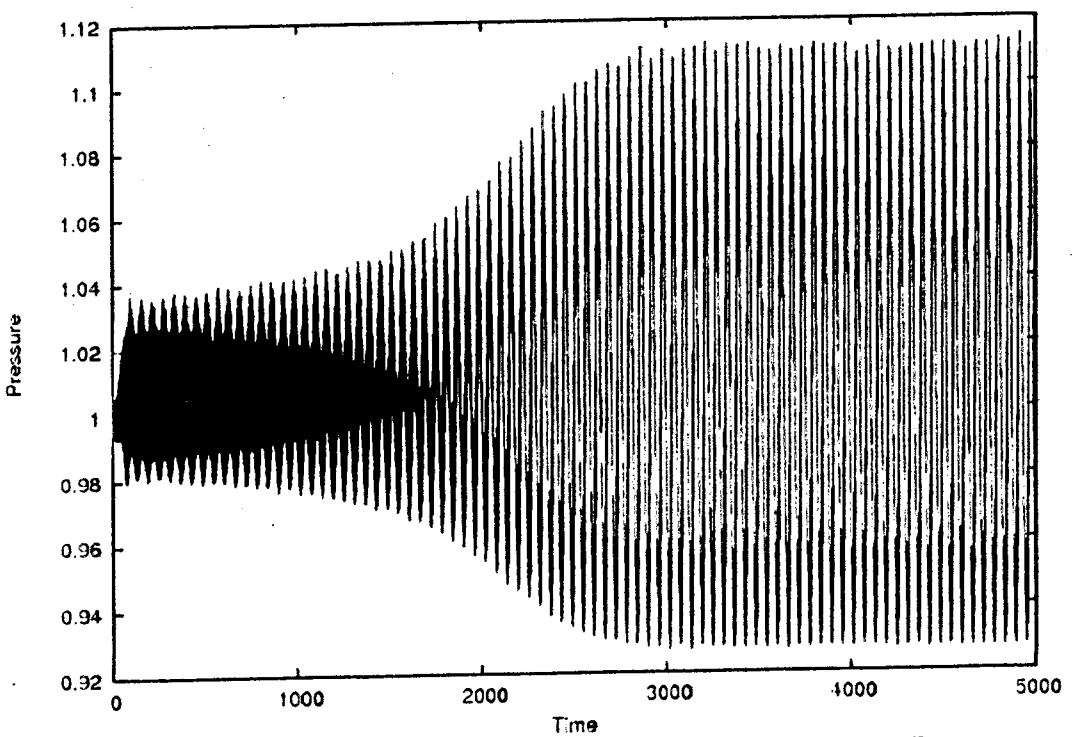

Figure 4.5.2a - Shock pressure history for Q = 10.3875, E = 5.0, K_e = 0.37

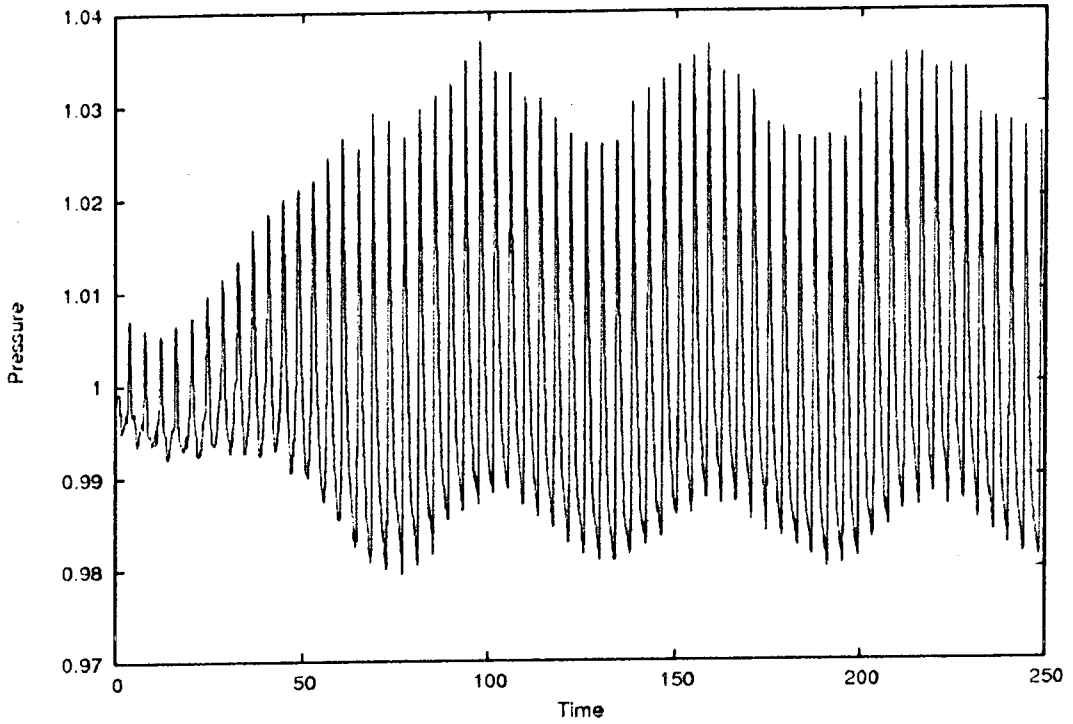

Figure 4.5.2b - Shock pressure history for Q = 10.3875, E = 5.0, K_e = 0.37

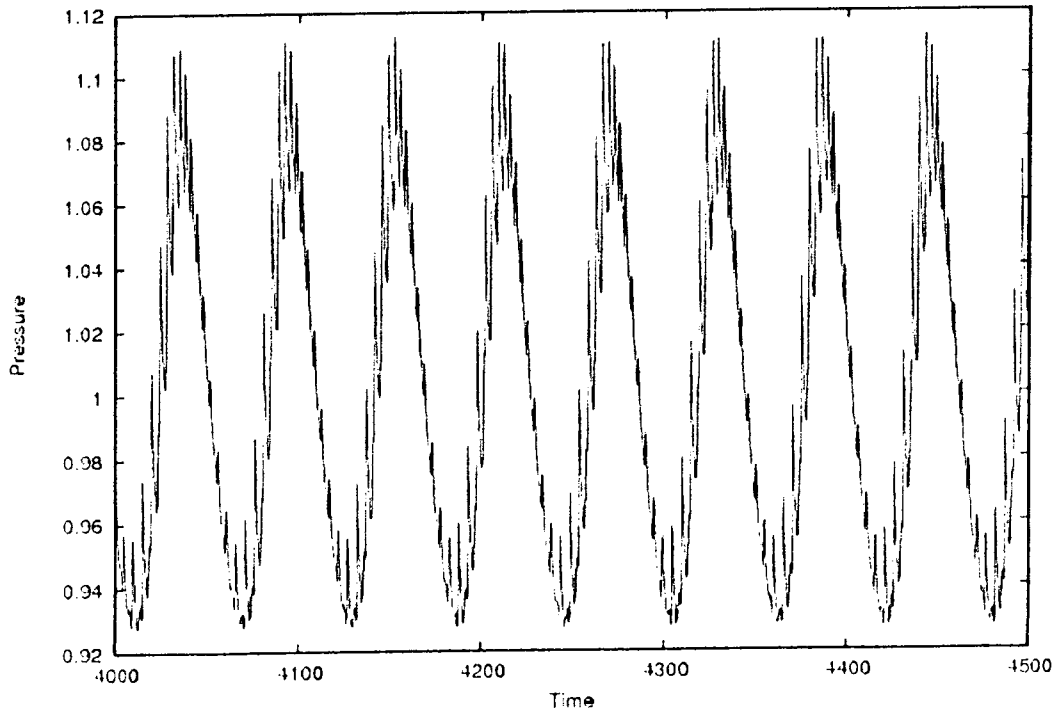

Figure 4.5.2c - Shock pressure history for Q = 10.3875, E = 5.0, K_e = 0.37

4.3 - High Frequency Pulsations

As shown in *Table 4.2*, high frequency oscillations with period of oscillation of 1-2 induction times are seen for moderate activation energy (E between 5 and 7.5) and low heat release (Q between 2.789 and 7.500). In the following section, a set of simulations with parameters E = 5, Q = 2.789, γ=1.2, ν = 0.5, and K_e = 3.20 was examined in detail. *Figure 4.6* shows the ZND profile for these parameters, and *Figure 4.7* shows the shock pressure history. *Figure 4.8* shows the family of characteristics on an x-t diagram, and *Figure 4.9* shows pressure and density profiles at various snapshots in time.

In the x-t diagram shown in *Figure 4.8*, the C+ characteristics moving to the right and the particle paths moving to the left are shown. For clarity, the reaction zone structure and the trajectory of the waves has been plotted in the CJ frame of reference so that the wave is, on average, approximately stationary.

In steady detonations, there exists a CJ point where the flow is exactly sonic relative to the leading shock, behind which the acoustic signals will never catch up to and influence the shock. Though there is no CJ point in pulsating detonations, there is a sonic surface or a limiting C+ characteristic that never reaches the shock, acting as an

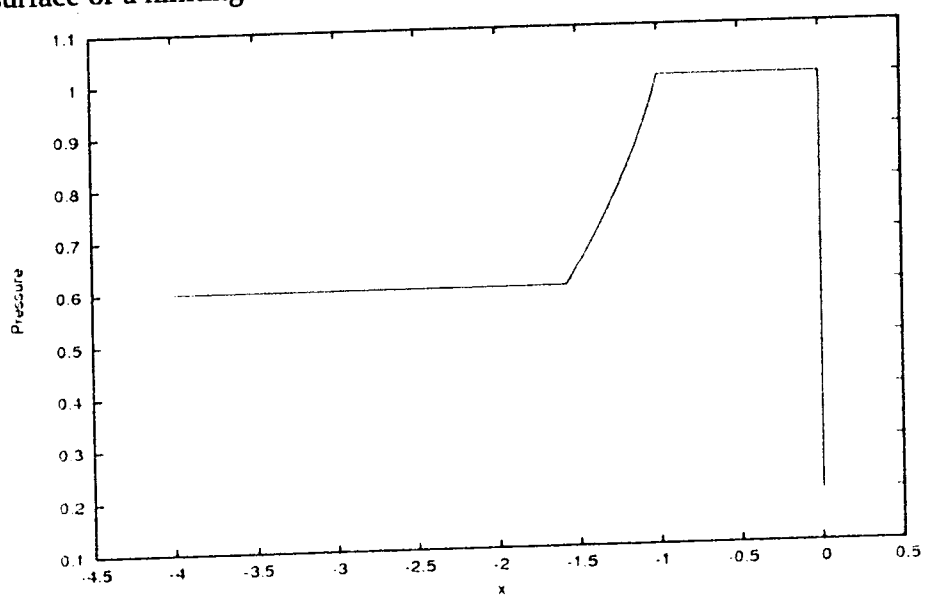

Figure 4.6 - ZND profile for E = 5, Q = 2.789, K_e = 3.20

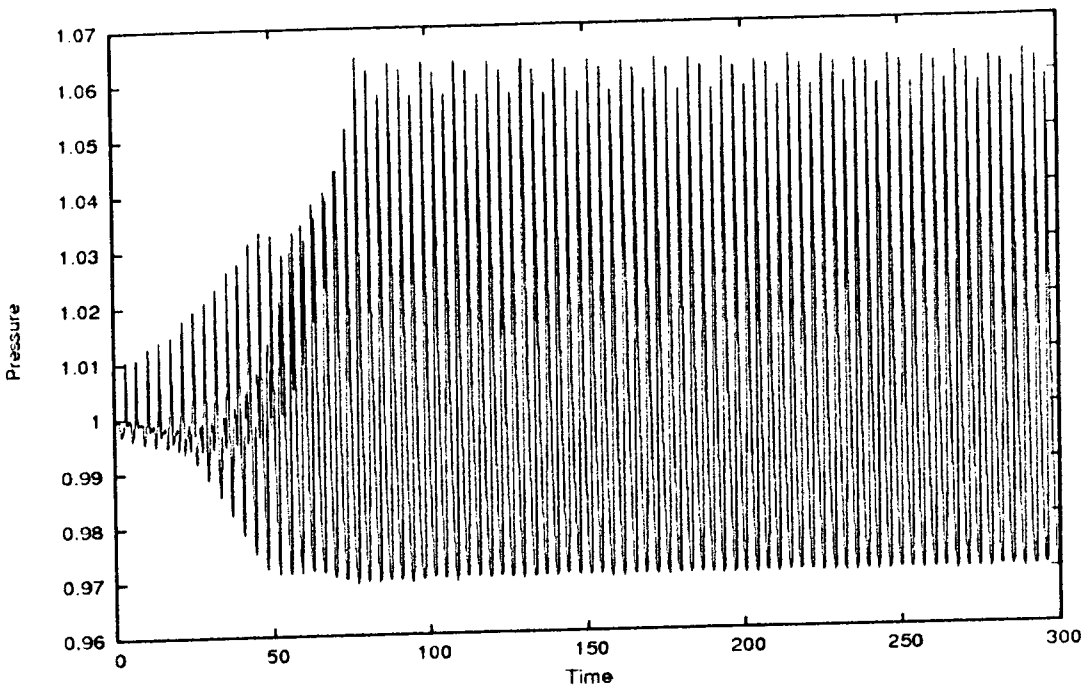

*Figure 4.7*a- Shock pressure history for $E = 5$, $Q = 2.789$, $K_e = 3.20$

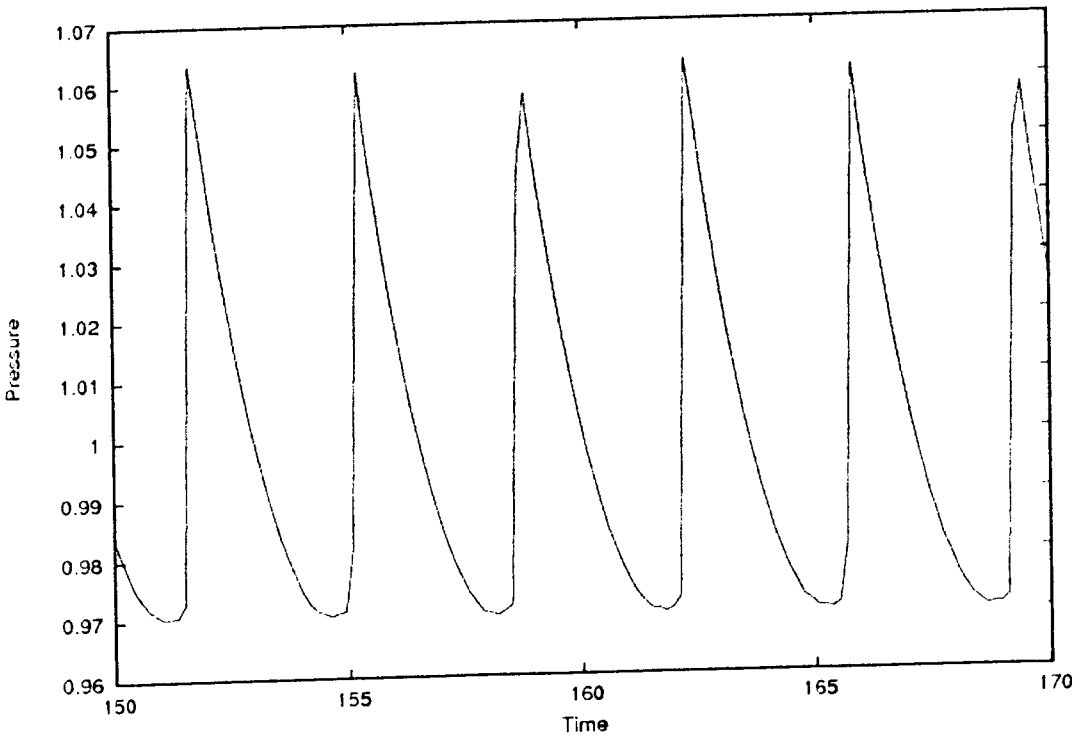

Figure 4.7b – Detail of the shock pressure history for $E = 5$, $Q = 2.789$, $K_e = 3.20$

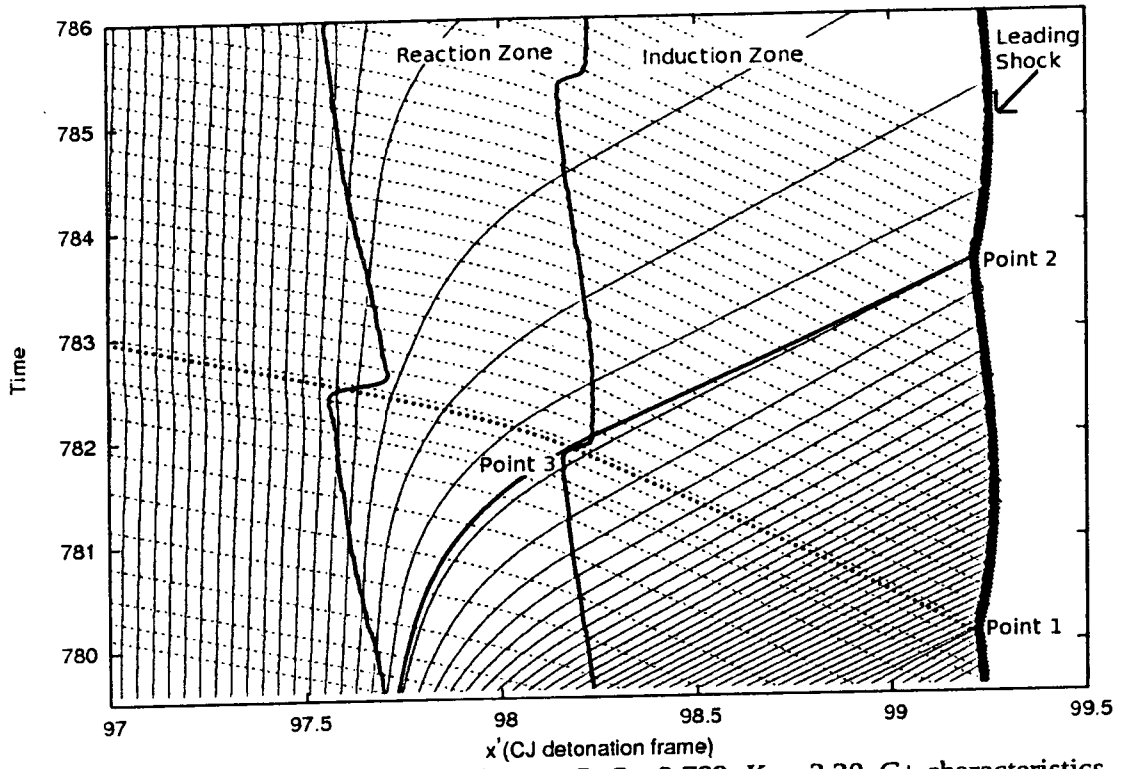

Figure 4.8 - Family of characteristics for $E = 5$, $Q = 2.789$, $K_e = 3.20$. C+ characteristics (solid curves moving to the right) and particle paths (dashed curves moving to the left) shown.

information boundary between the shock and the burnt flow. In *Figure 4.8*, C+ characteristics near the end of the reaction zone are seen leaving and re-entering the reaction zone, showing that the sonic surface does not coincide with the location of the end of the reaction zone, and that the limiting C+ characteristic is located in the burnt region behind the reaction zone. This is similar to the observations made by Kasimov and Stewart (2004), where acoustic signals near the end of the reaction zone were seen leaving and re-entering the reaction zone.

The oscillations of the leading shock is very weak with an amplitude in the shock pressure of roughly 1.06, and the induction zone is oscillating at the same period as the shock. The period of oscillation is well correlated by the time it takes for a particle to travel across the induction zone from the leading shock plus the time it takes for a C+ characteristic to travel across the induction zone toward the leading shock, as seen by

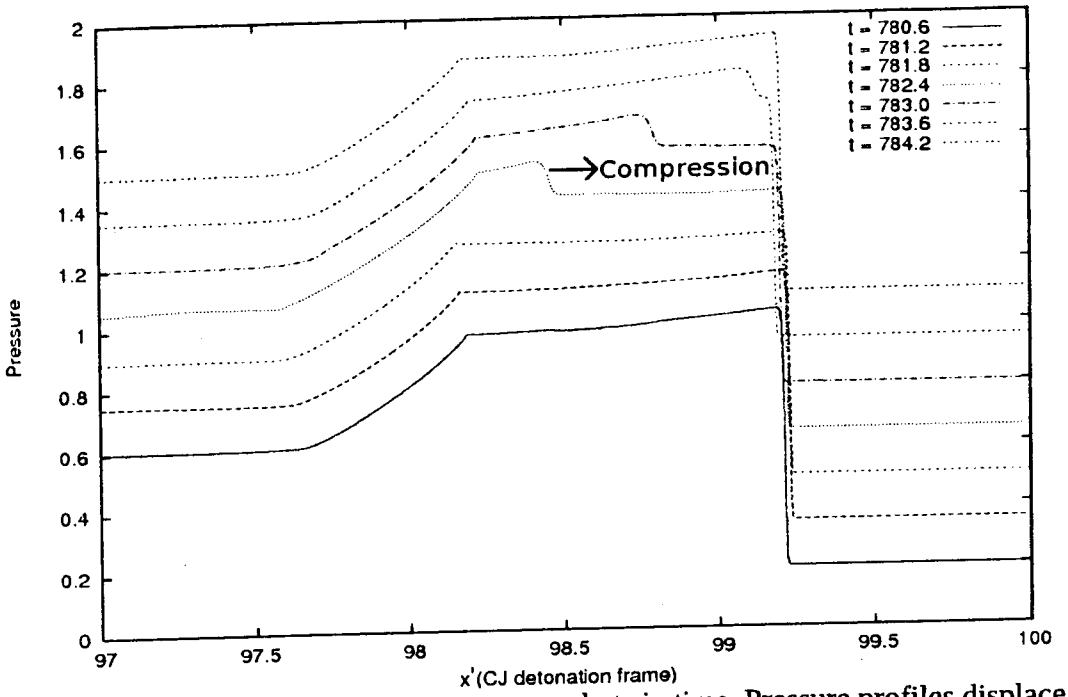

Figure 4.9a - Pressure profiles for various snapshots in time. Pressure profiles displaced by *0.15* on the pressure axis

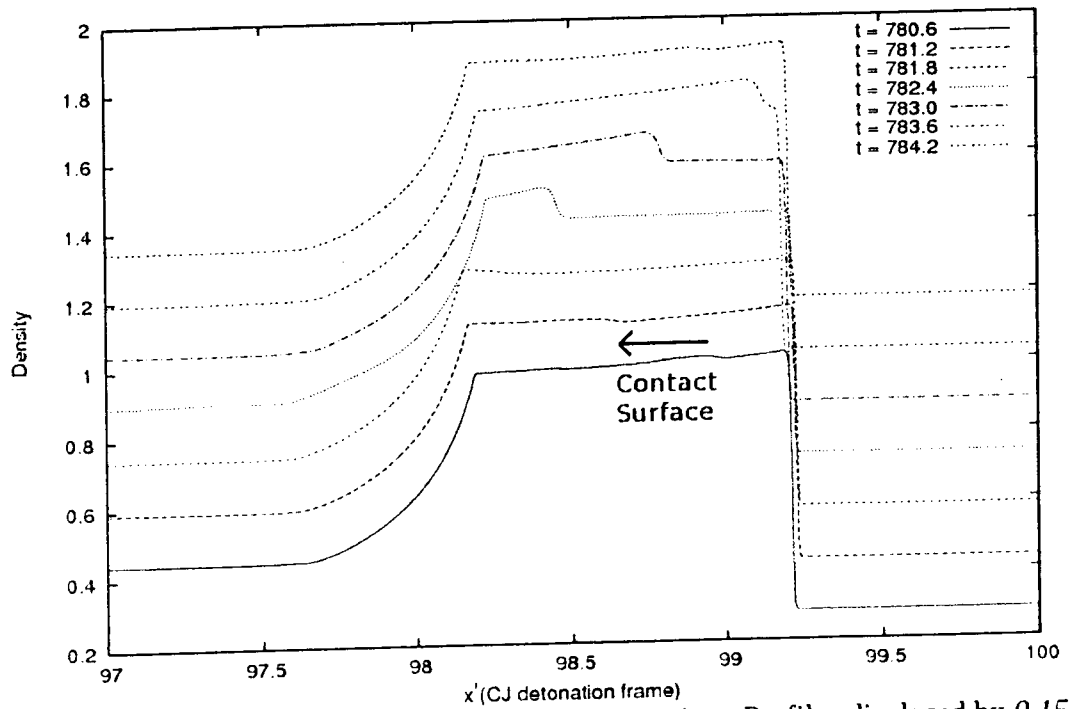

Figure 4.9b - Density profiles for various snapshots in time. Profiles displaced by *0.15* on the pressure axis

following the hot particle path from *Point 1* toward the end of the induction zone at *Point 3*, and following the C+ characteristic back toward the shock at *Point 2*.

To gain a clearer picture of the wave dynamics, the pressure profiles for this process are shown in *Figure 4.9*. Starting at t = 780.6, the hot particle travels across the induction zone until t = 781.8, when the hot particle reaches the reaction zone (seen in *Figure 4.9b*, but not in *Figure 4.9a*). At this point, a shock wave is generated at the start of the reaction zone and moves toward the leading shock, until it catches up to the leading shock, starting the cycle anew. The mechanism operating here is consistent with Toong's mechanism for a square wave detonation, where a hot particle triggers a discrete compression wave upon reaching the end of induction zone, and the expansion waves traveling along the C+ characteristics in *Figure 4.8* are decelerating the leading shock.

Note that in *Figure 4.8*, when the hot particle reaches the reaction zone, the location of the start of the reaction zone gets pulled toward the shock so that it is approximately parallel with the C+ characteristics. At the start of the reaction zone is a zone of rapid heat release. A likely mechanism here is the SWACER (Shock Wave Amplification through Coherent Energy Release) mechanism described by Yoshikawa (1980). The compression waves traveling along the C+ characteristics are traveling in phase with the zone of heat release, thus the strength of the wave will be amplified through heat release in the reaction zone.

For a larger K_e, and thus shorter reaction zone, the rate of energy release at the reaction zone will be much more rapid. According to the SWACER mechanism described above, the parameter, K_e, can then control the amount of amplification the shock wave receives. For a small value of K_e, the rate of energy release will be comparatively small, and thus the shock wave does not amplify quickly enough for instabilities to arise.

4.4 - Very High Frequency Pulsations

Table 4.2 shows that for very low activation energy, E = 1, where the reaction zone is thin at the stability boundary, very high frequency pulsations with periods of less than one induction time are seen. In order to study the very high frequency pulsations, simulations using the parameters E = 1, Q = 10.3875, γ = 1.2, υ = 0.5, and K_e = 2.100

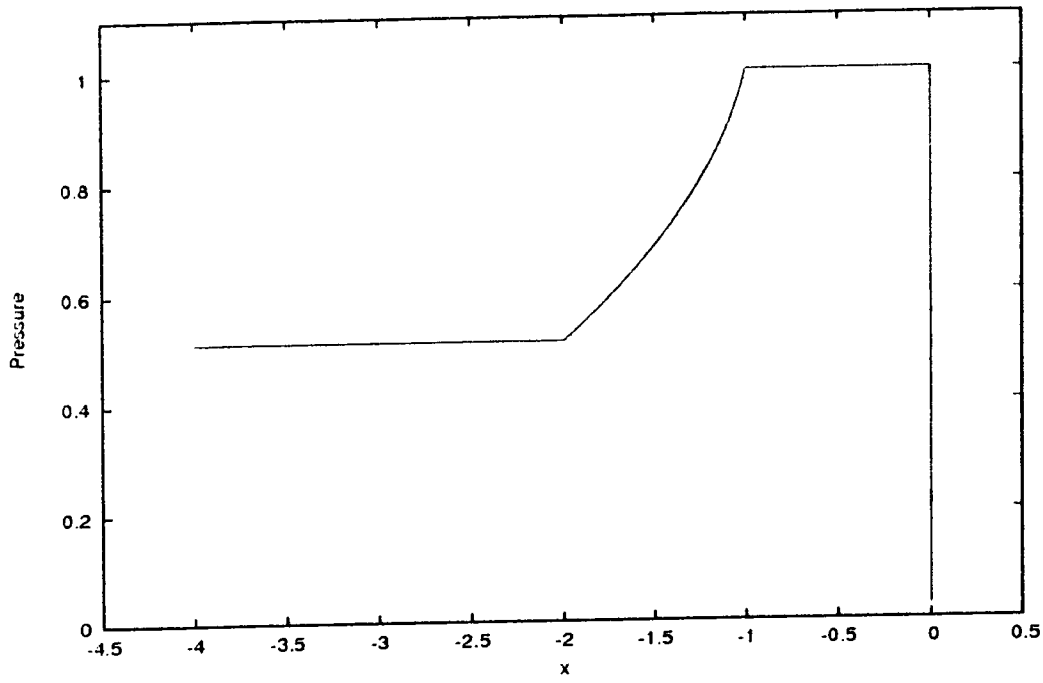

Figure 4.10 - ZND pressure profile for $E = 1$, $Q = 10.3875$, $K_e = 2.100$

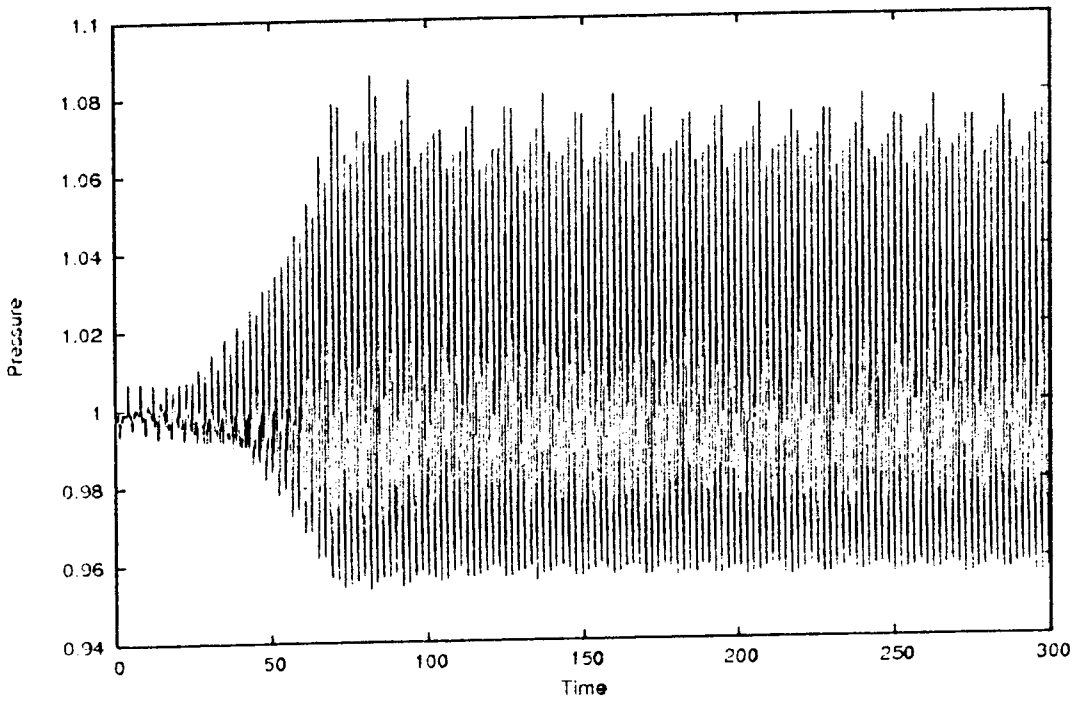

Figure 4.11a - Shock pressure history for $E = 1$, $Q = 10.3875$, $K_e = 2.100$

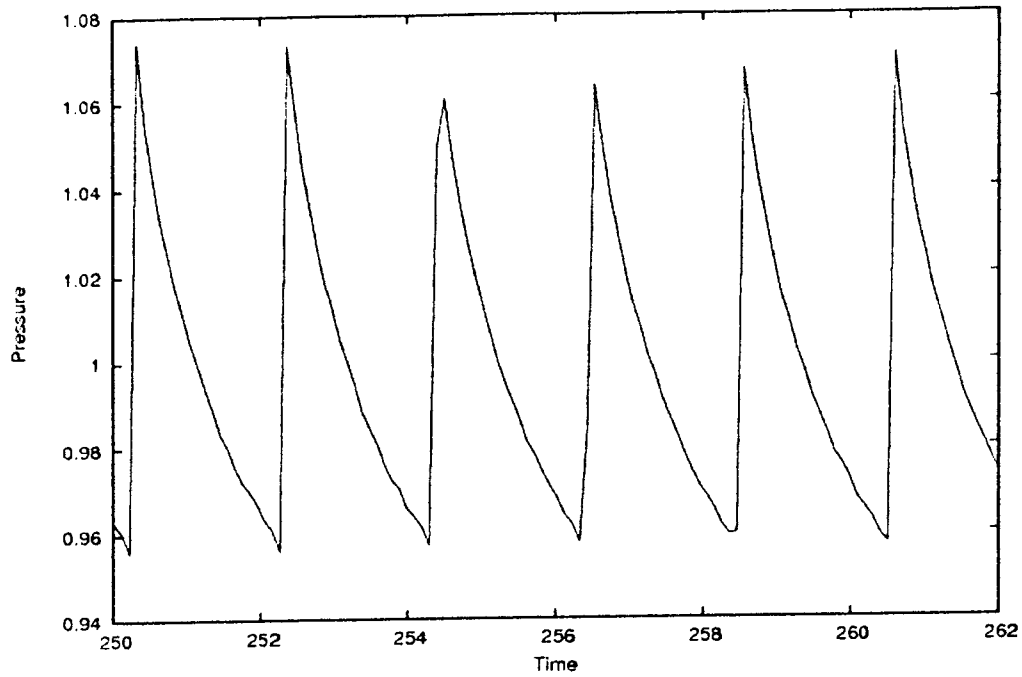

Figure 4.11b - Shock pressure history for $E = 1$, $Q = 10.3875$, $K_e = 2.100$

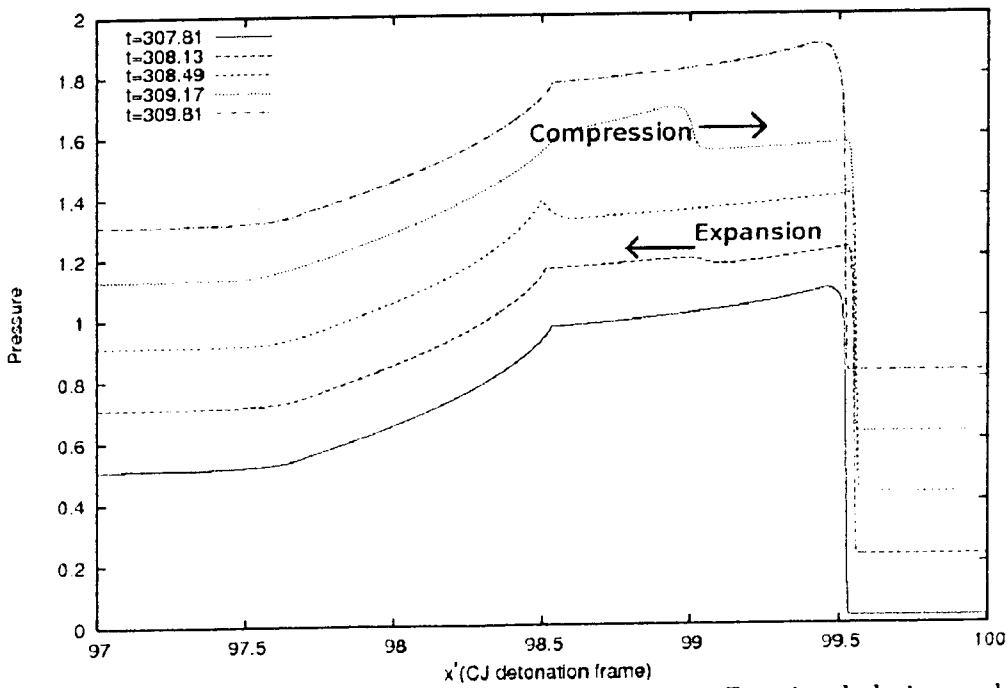

Figure 4.12 - Pressure profiles for various snapshots in time. For visual clarity, each profile is displaced by 0.2 on the pressure axis

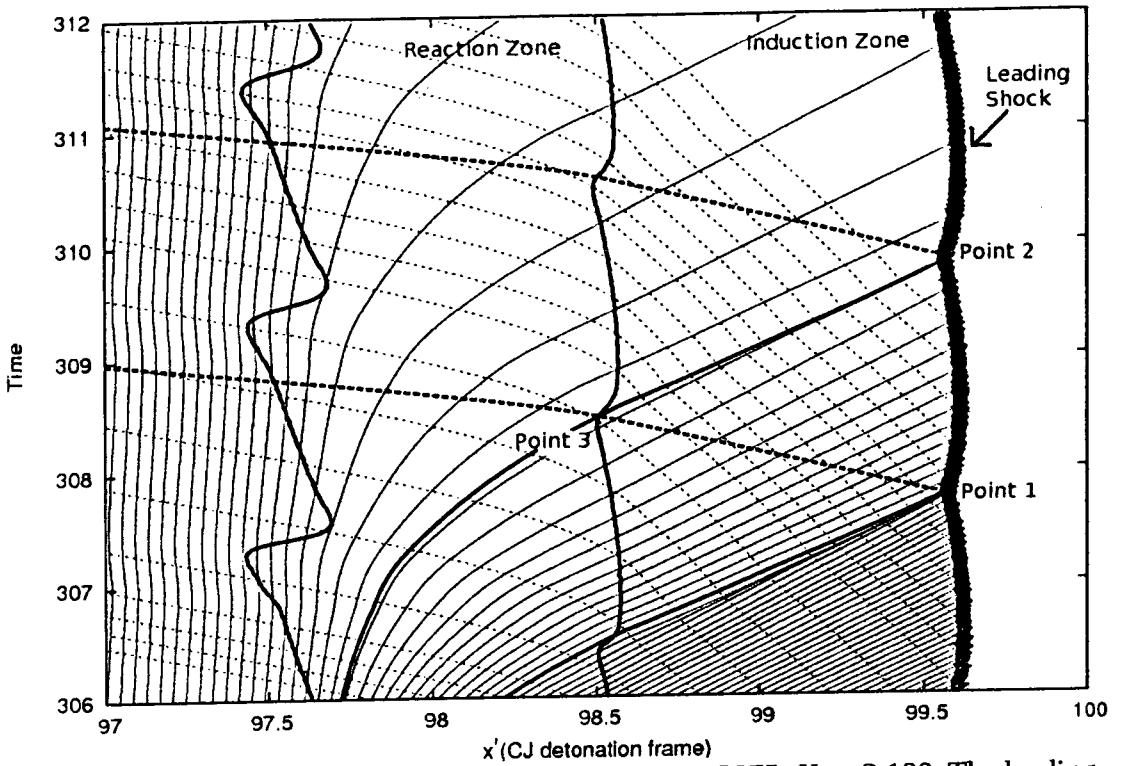

Figure 4.13 - Family of characteristics for $E = 1$, $Q = 10.3875$, $K_e = 2.100$. The leading shock, induction zone, reaction zone, C+ characteristics (moving to the right), particle paths (dashed curves moving to the left) and two C- characteristics (thick dashed curves moving to the left) are shown

were investigated in detail. *Figure 4.10* shows the ZND profile and *Figure 4.11* shows the shock pressure history. *Figure 4.12* shows pressure profiles at various snapshots in time. The family of characteristics for the high frequency cycles were constructed and shown in *Figure 4.13* on an x-t diagram.

The x-t diagram in *Figure 4.13* shows C+ characteristics traveling to the right toward the leading shock, and particle paths moving to the left toward the end of the reaction zone. Two C- characteristics are shown, starting from *Point 1* and *Point 2* at the leading shock, moving to the left.

As with *Figure* 4.8, the oscillation of the shock is very weak and the shock pressure has an amplitude of roughly 1.08. The induction zone and reaction zone end can be seen oscillating at the same period as the shock. However, as the period of oscillation is much lower than even one induction time, a mechanism different from Toong's

mechanism is likely operating. The period of oscillation appears to be correlated by the time it takes a C- characteristic to travel from the shock at *Point 1* to the induction zone at *Point 3*, and the time it takes for a C+ characteristic to travel from the *Point 3* back to the leading shock to *Point 2*.

The pressure profiles at various times can be seen in *Figure 4.12*. Starting at t = 307.81, an expansion wave forms and travels to the left, along the C- characteristic originating from *Point 1* shown in *Figure 4.13*. At t = 308.49, the expansion wave reaches the reaction zone, and a shock wave moving to the right forms. The shock wave travels across the induction zone along the C+ characteristic toward *Point 2* until it catches up to the leading shock front, where an expansion wave gets reflected, starting the cycle anew.

From *Figure 4.12* and *Figure 4.13* it appears that the expansion waves traveling along the C- coupled with the compression wave traveling along the C+ generated by the expansion wave are responsible for the very high frequency of oscillation. The compression wave is generated when the expansion wave passes into the reaction zone. As the expansion wave passes across the reaction zone, it enters a region with a different acoustic impedance, ρc. For a perfect gas, the acoustic impedance can be rewritten in

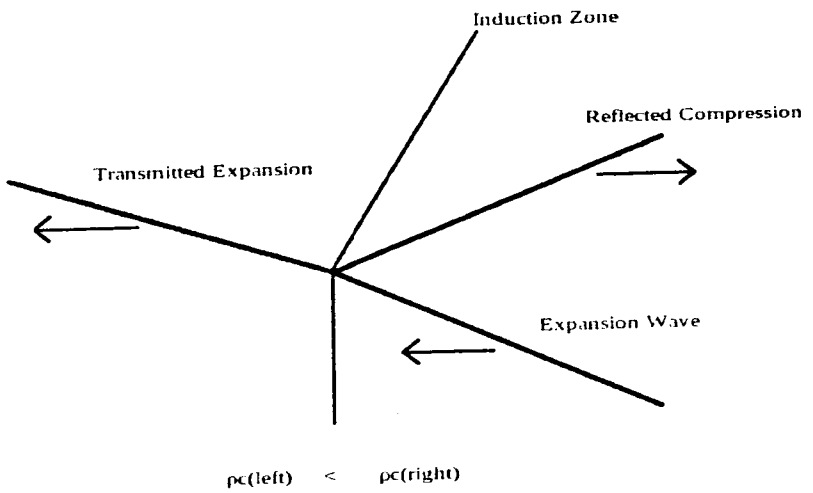

Figure 4.14 - Sketch of expansion passing into a region of lower acoustic impedance

terms of pressure and density:

$$\rho c = \rho\sqrt{\frac{\gamma P}{\rho}} = \sqrt{\gamma \rho P}$$

As heat is being released behind the induction zone, both ρ and P will be at a lower value, and hence the acoustic impedance will be lower than in the induction zone. As a result, the transmitted wave will be an expansion and the reflected wave will be a compression, as illustrated in *Figure 4.14*.

When the expansion wave along the C- at *Point 1* reaches the reaction zone, the reaction zone gets pulled toward the shock so that it is approximately parallel with the C+ characteristics, similar to the high frequency case examined previously. The compression waves traveling along the C+ characteristics then get amplified by the heat release behind the induction zone.

The effect of changing the reaction rate parameter, K_e, is the same as the high frequency case, where the lengthening of the reaction zone causes the heat release to occur at a slower rate, hence weakening the amplification received by the newly generated compression waves.

Note the arrival of the C- characteristic originating from *Point 2* to the induction zone coincides with the arrival of the hot particle originating from *Point 1*. It appears that in the case examined here, the mechanism described works in conjunction with the high frequency (or Toong's) mechanism. The expansion wave generated by the current cycle combined with the hot particle of the previous cycle arrive at the reaction zone at roughly the same time and these two effects work together to form the compression wave.

By modifying the model parameters of the detonation (for example, Q or γ) the two mechanisms can be decoupled. Detailed calculations for the conditions required for the two mechanisms to overlap can be found in *Appendix D*. *Figure 4.15, 4.16* and *4.17* show the ZND profile, shock pressure history, and the family of characteristics for parameters $E = 1$, $Q = 5.000$, $\gamma = 1.2$, $\upsilon = 0.5$, $K_e = 5.900$, where the two mechanisms are decoupled. In *Figure 4.17*, faint oscillations are seen in the reaction zone and the induction zone, and the pulsations in the shock front are too weak to be seen.

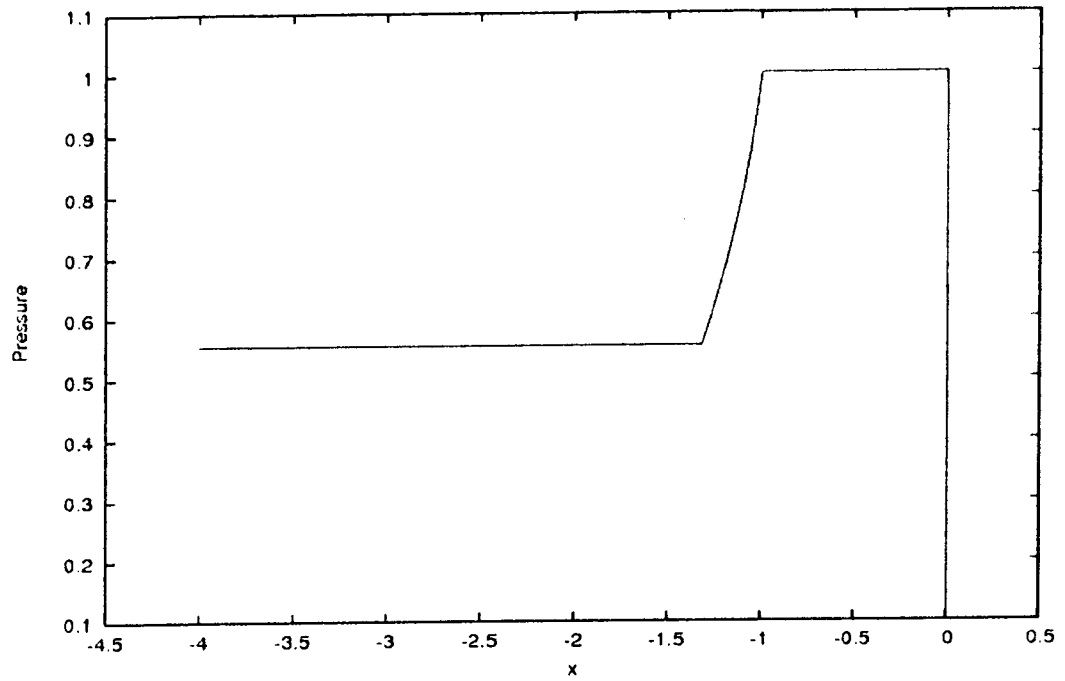

Figure 4.15 - ZND pressure profile for E = 1, Q = 5.000, K_e = 5.900

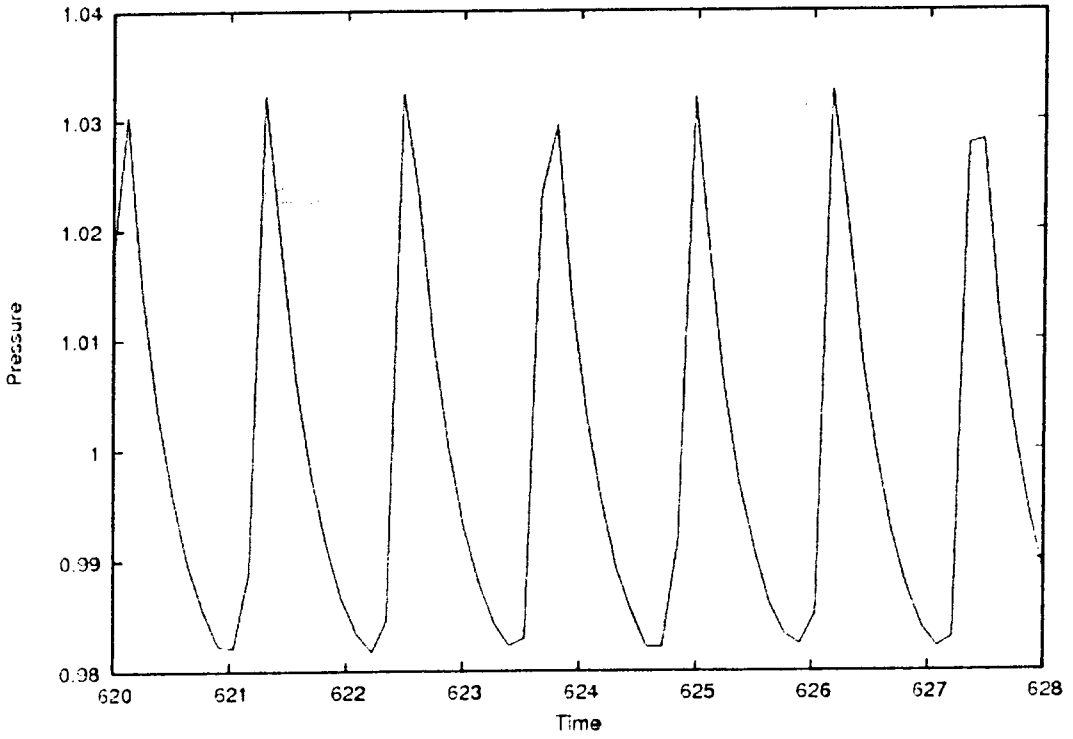

Figure 4.16 - Shock pressure history for E = 1, Q = 5.000, K_e = 5.900

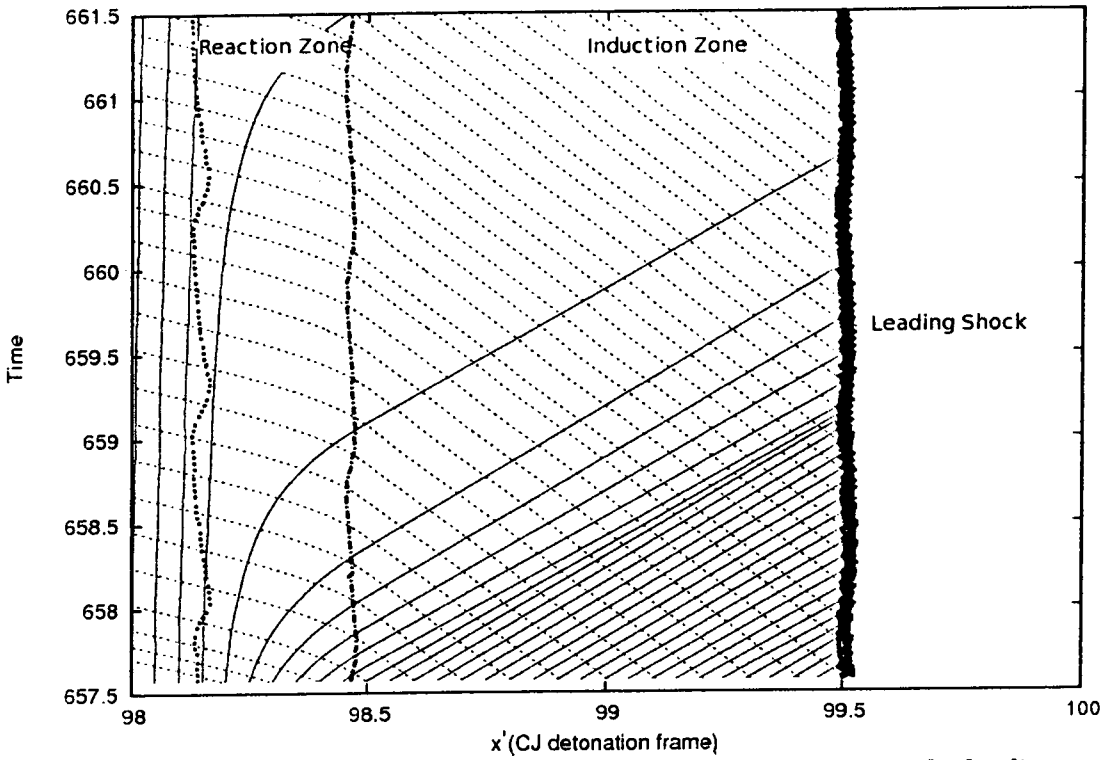

Figure 4.17 - Family of characteristics for E = 1, Q = 5.000, K_e = 5.900. The leading shock, induction zone, reaction zone, C+ characteristics (moving to the right), and particle paths (dashed curves moving to the left) are shown. Oscillations are very weak

4.5 - Low Frequency Pulsations

Table 4.2 shows that the low frequency oscillations tend to appear for high activation energy, E = 10, where the reaction zone is long at the stability boundary. In order to study the low frequency pulsations, simulations were run using the parameters E = 10, Q = 10.3875, γ = 1.2, υ = 0.5, and K_e = 0.15. *Figure 4.18* shows the ZND profile for this case, and the evolution of the shock pressure as the detonation is propagating to the right is shown in *Figure 4.19*. *Figures 4.20* and *4.21* show the family of characteristic curves on an x-t diagram. *Figure 4.20* shows the C+ characteristics together with the particle paths, while *Figure 4.21* shows the C+ characteristics together with the C- characteristics omitted from *Figure 4.20*. *Figures 4.22* and *4.23* show the pressure profile at various snapshots in time. Figure 4.24 shows a sample pressure profile

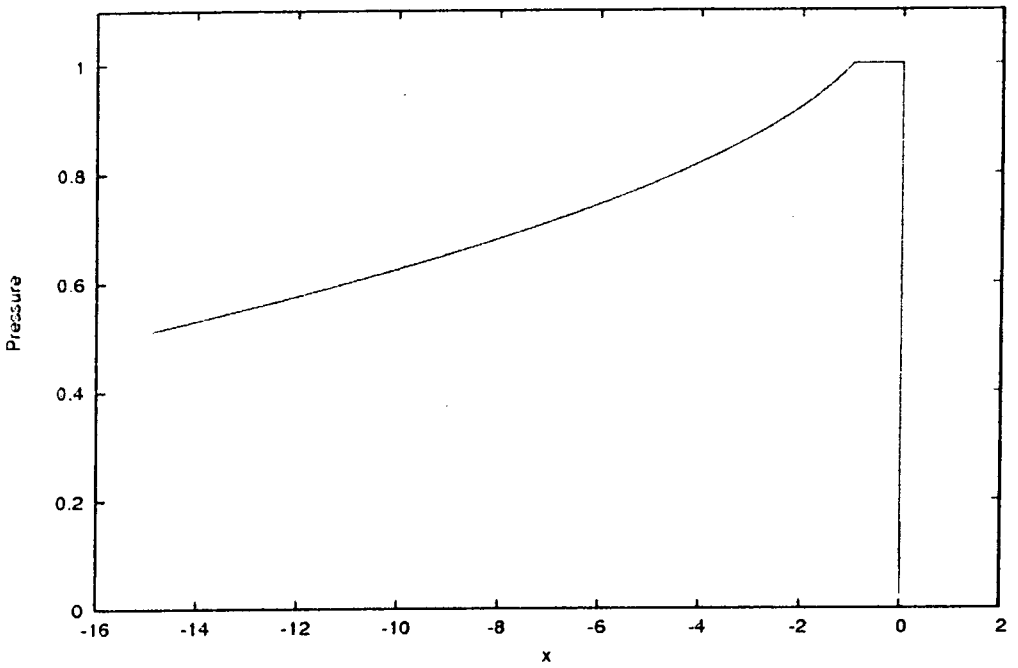

Figure 4.18 - ZND pressure profile for parameters E = 10, Q = 10.3875, K_e = 0.15

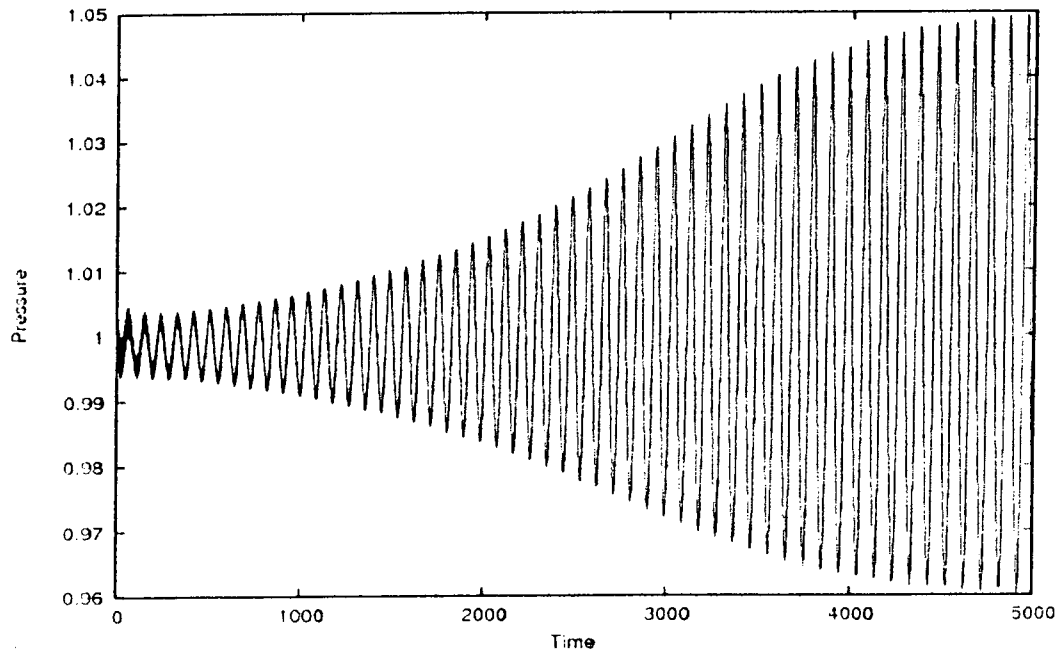

Figure 4.19a - Shock pressure history for E = 10, Q = 10.3875, K_e = 0.15

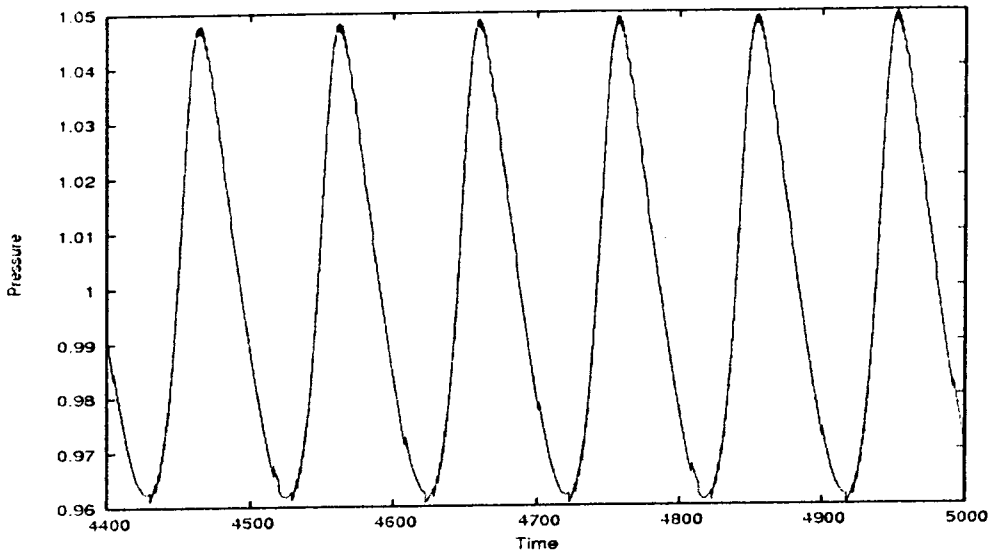

Figure 4.19b - Shock pressure history for E = 10, Q = 10.3875, K_e = 0.15

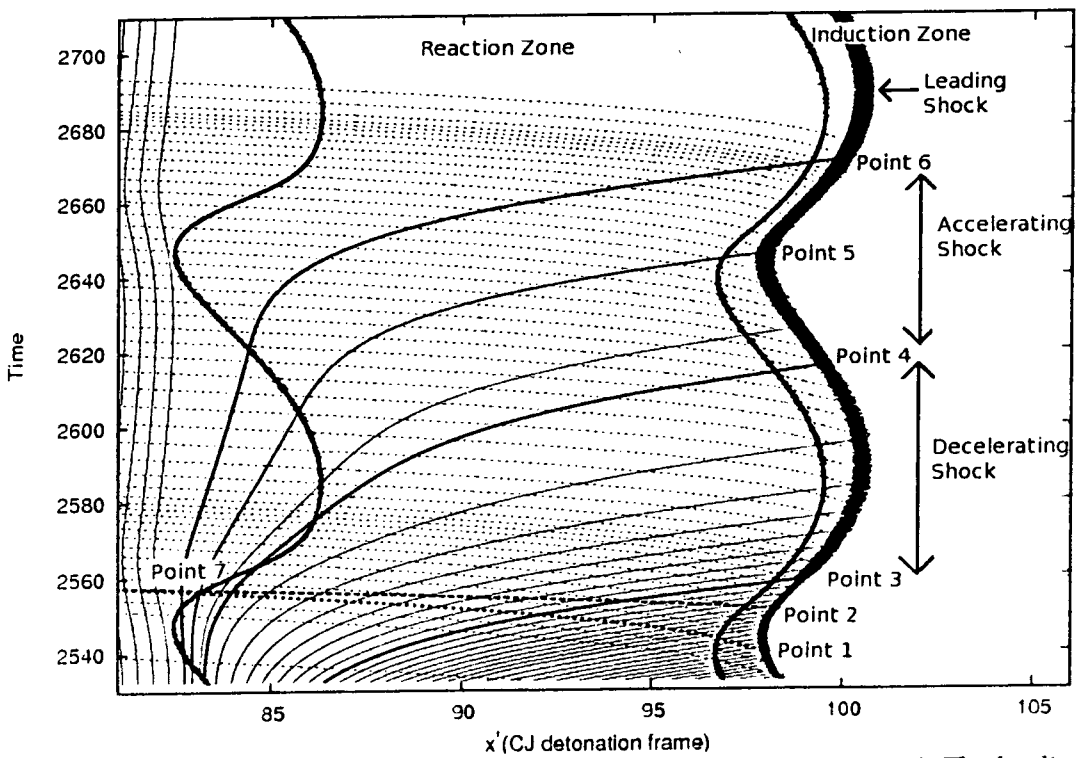

Figure 4.20 - Family of characteristics for E = 10, Q = 10.3875, K_e = 0.15. The leading shock, end of the induction zone, end of the reaction zone, C+ curves (solid curves moving to the right) and particle paths (dashed curves moving to the left) are shown. One sample C- curve (dashed curve) is shown, starting from *Point 2* and moving to the left.

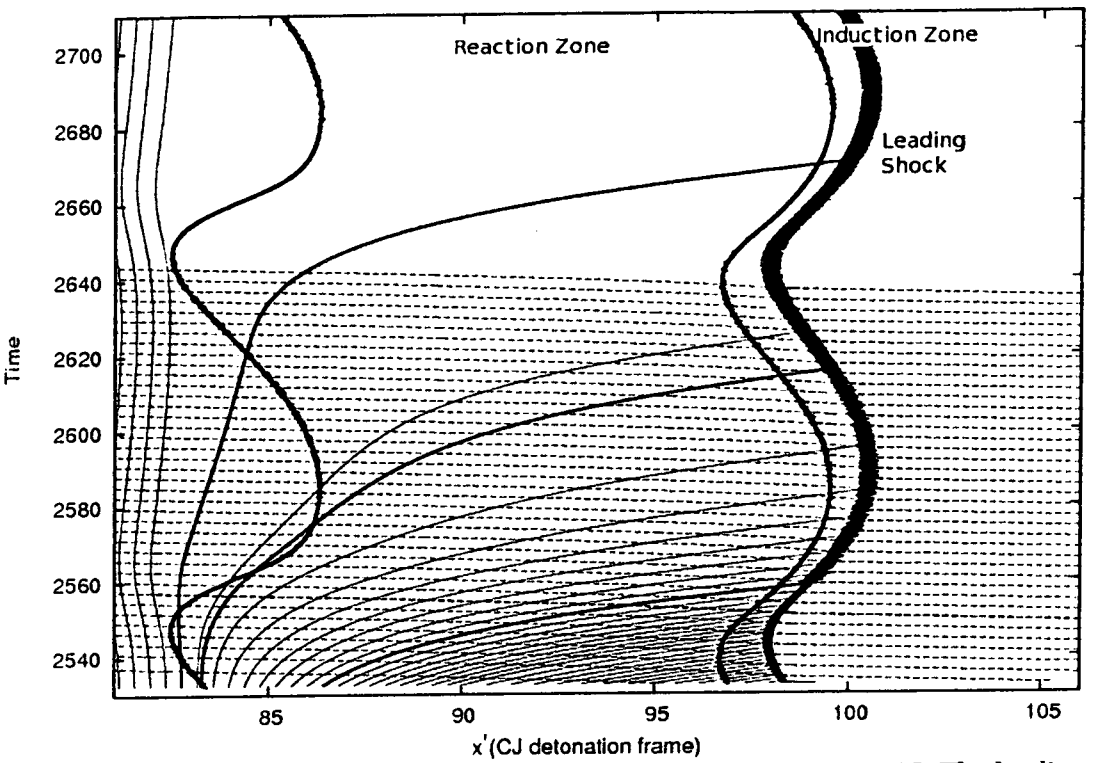

Figure 4.21 - Family of characteristics for E = 10, Q = 10.3875, K_e = 0.15. The leading shock, end of the induction zone, end of the reaction zone, C+ (solid curves moving to the right) and C- (dashed curves moving to the left) are shown

in the burnt region behind the reaction zone.

The space-time diagram of the family of characteristics for the low frequency cycles has been constructed and shown in *Figure 4.20. Figure 4.20* shows the C+ characteristics moving to the right, toward the leading shock, and the particle paths moving to the left, toward the rear of the reaction zone. One sample C- curve, starting from *Point 2*, and moving to the left, is shown.

The velocity of the leading shock front is seen to be oscillatory. Shock waves accelerate when overtaken by a compression wave and decelerate when overtaken by an expansion wave. The velocity of the shock can be inferred from *Figure 4.20* by determining its slope, *dx/dt*. The acceleration can then be determined by examining the rate of change of the slope. Between *Point 3* and *Point 4*, as labeled on *Figure 4.20*, the shock front is decelerating, since the slope *dx/dt* is decreasing. *Figure 4.22* shows

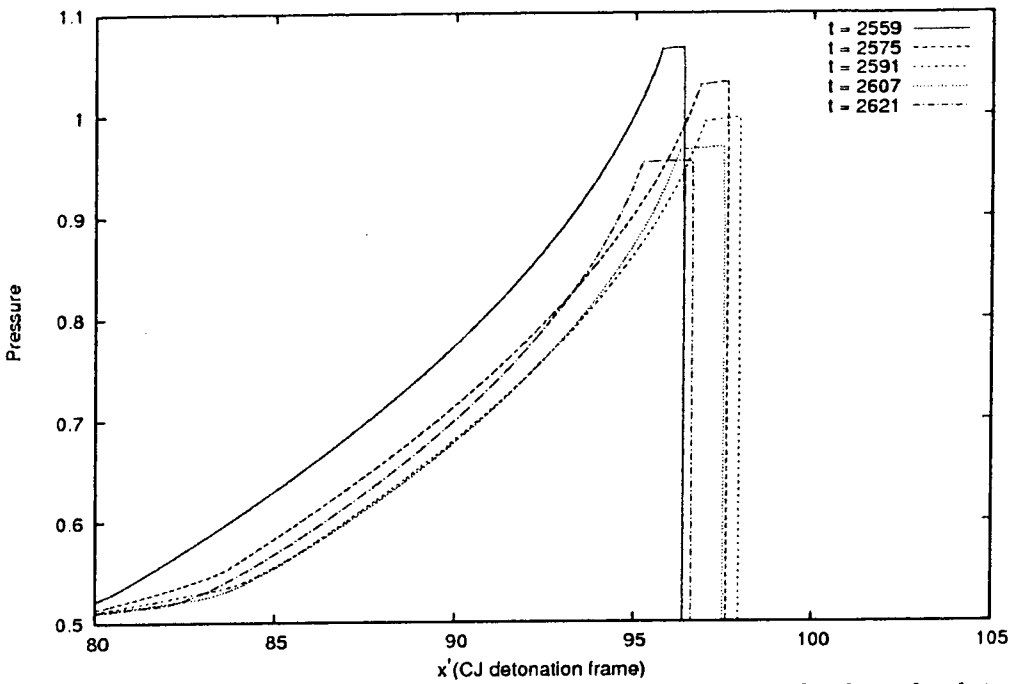

Figure 4.22a - Pressure profiles at various snapshots in time (while leading shock is decelerating)

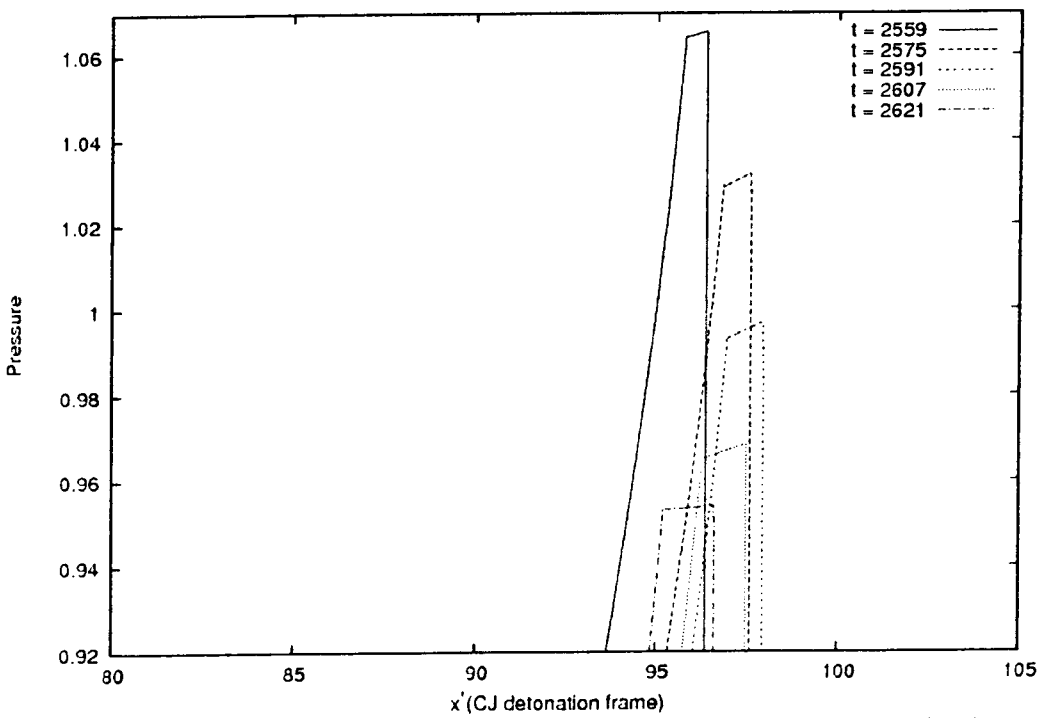

Figure 4.22b - Pressure profiles at various snapshots in time (while leading shock is decelerating)

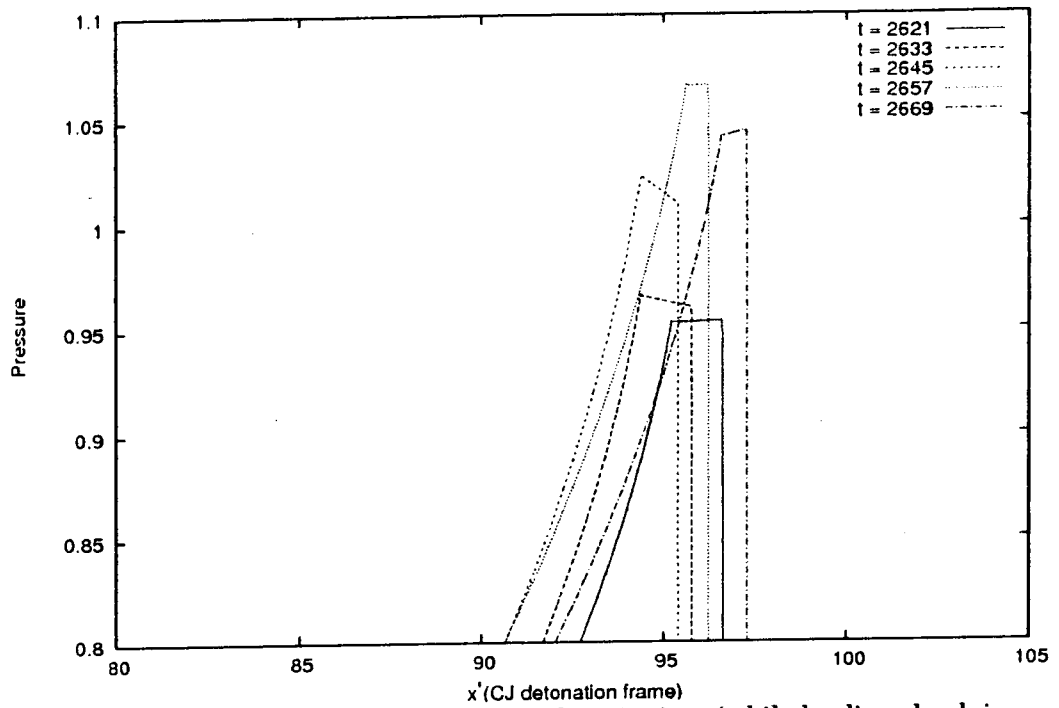

Figure 4.23 - Pressure profiles at various snapshots in time (while leading shock is accelerating)

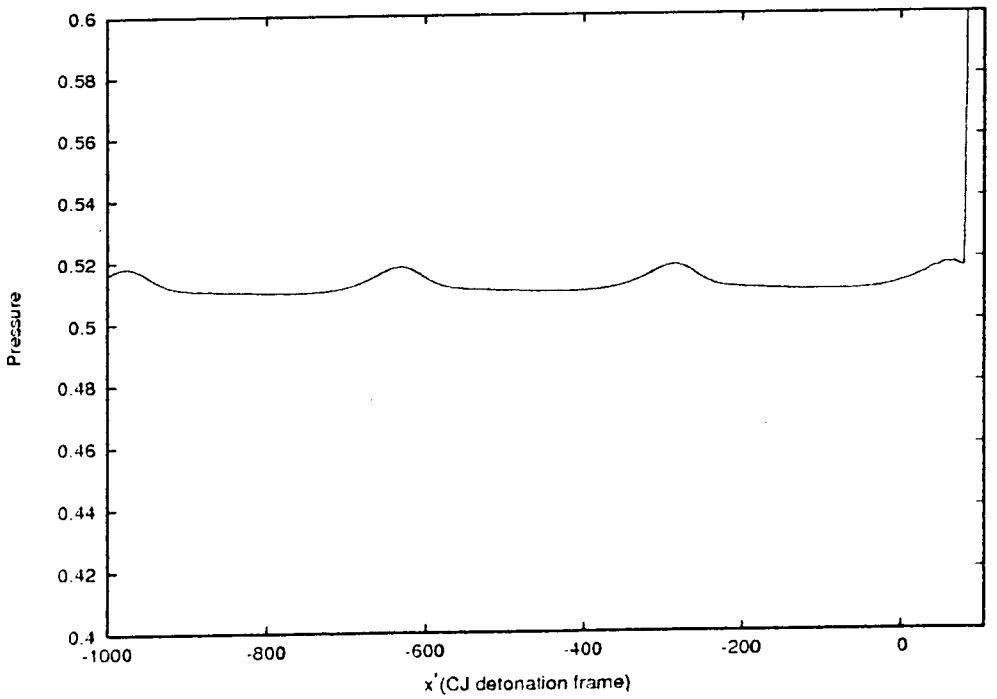

Figure 4.24 - Sample pressure profile at t = 2559 in the burnt region

pressure profiles for various snapshots in time between *Points 3* and *4*. Between *Point 4* and *Point 6*, the shock front is accelerating, since the slope *dx/dt* is increasing. *Figure 4.23* shows pressure profiles for various snapshots in time between *Points 4* and *6*. The expansion waves responsible for the deceleration can be tracked by following the C+ characteristics between *Point 3* and *Point 4*. Likewise, the compression waves causing the acceleration can be tracked by following the C+ characteristics between *Point 4* and *Point 6*. The compression and expansion waves seen traveling to the left in the burnt region in *Figure 4.24* can be tracked along the C- characteristics in *Figure 4.21* back toward the detonation. By tracking the compression and expansion waves in this manner, the origin of the pressure waves can be found to originate within the rear of the reaction zone.

The time scale for the period of oscillation can roughly be correlated by the time it takes for a C+ characteristic to reach the shock front from the rear of the reaction zone. The time scale for a particle or C- characteristic to reach the rear of the reaction zone from the shock front is comparatively small. It is thus unclear whether the particle path or the C- characteristic influence the pulsating dynamics. For example, following the particle path from *Point 1*, or the C- from *Point 2*, to the end of the reaction zone, at *Point 7*, then following the C+ from *Point 7* back toward the leading shock to *Point 5* both give a time scale comparable to the period of oscillation.

The observations made on the *x-t* diagram shown in *Figure 4.20* suggest that the mechanism for the low frequency pulsations may be similar to Toong's mechanism and the high frequency pulsations examined previously. In *Figure 4.20*, a series of compression waves, corresponding to a shortening of the induction zone, is followed by a series of expansion waves originating from the rear of the reaction zone. In the high frequency cases, these compression waves are discrete, originating from a single point. However, in the low frequency case, the compressions and expansions occur over a broader, continuous region. In the high and very high frequency cases, the period of oscillation is correlated by the time it takes for a particle path or C- to travel across the induction zone plus the time it takes for a C+ to travel from the start of the reaction zone back toward the leading shock. The low frequency case differs in that the period of

oscillation is correlated by the time it takes for the characteristics to traverse the entire reaction length rather than just the induction length, hence the much longer period of oscillation.

As discussed above, the low frequency pulsations are seen for high activation energy, corresponding to a lower value for the induction to reaction length ratio at the stability limit. Thus, the low frequency pulsations correspond to ZND structures with longer reaction zones. In this case, the transit time for the waves across the reaction zone is large relative to the induction zone transit times. In the high frequency oscillations, the opposite is true. The high frequency pulsations occur for a low activation energy, corresponding to ZND structures with shorter reaction lengths at the stability boundary. In this case, the pulsations evolve over the induction time scale.

4.6 - Relevance of Current Study to Real Detonations

In the current study, the pulsating dynamics were studied using an idealized two-step model. *Tables 4.3 (*Radulescu, personal correspondence), *4.4* (Austin et al. 2005) and *4.5* (Radulescu 2003) show representative values of E, Q, the ratio of the induction to reaction lengths, and the ratio of the induction to reaction times for real mixtures. *Table 4.3-4.5* show that real mixtures typically have E ~ 5-10 and Q ~ 2-10. The range of E and Q investigated in this study correspond closely to the range of parameters found in real mixtures.

Tables 4.4-4.5 show that real mixtures typically have large values of Δ_i/Δ_e corresponding to narrow reaction zones. According to the results of this work, for large Δ_i/Δ_e, one would expect high frequency pulsations. However, in real mixtures, not only is the reaction zone narrow, but the activation energy is high and real mixtures tend to be further away from the stability boundary. Hence, real mixtures tend to be more unstable than the cases studied in this work. Also, in practice, the multi-dimensional instability leads to transverse instabilities and cellular structures. Although neither the cases far away from the stability boundary nor the complex multi-dimensional instability observed in real mixtures have been investigated, this work provides analysis of the simplest

Table 4.3 - Parameters for real mixtures (Radulescu, personal correspondence)

Mixture	E	Q
$C_2H_2 + 2.5\ O_2$	5.3	7.3
$C_2H_2 + 9.5\ O_2$	5.6	4.6
$C_2H_2 + 2.5\ O_2$ + 50% Ar	5.1	3.6
$C_2H_2 + 2.5\ O_2$ + 70% Ar	5.1	2.5
$C_2H_2 + 2.5\ O_2$ + 75% Ar	5.1	2.2
$C_2H_2 + 2.5\ O_2$ + 85% Ar	5.2	1.8
C_2H_2 + 2.5 Air	7.8	4.3
$2\ H_2 + O_2$ + 40% Ar	4.5	2.4
$2\ H_2 + O_2$ + 70% Ar	4.6	1.7
$2\ H_2 + O_2$	5.1	3.4
$2\ H_2$ + Air	8.1	3.3
H_2 + Air	32.1	3.0
$C_3H_8 + 5\ O_2$	8.7	12.3
C_3H_8 + Air	1.4	4.7
$CH_4 + 2\ O_2$	11.1	7.8
CH_4 + 2 Air	13.2	4.2

Table 4.4 - Parameters for real mixtures (taken from Austin et al. 2005)

Mixture	E	Q	Induction/Reaction length
$2\ H_2 + O_2$ + 12 Ar	5.2	3.78	0.8
$2\ H_2 + O_2$ + 17 Ar	5.4	2.46	0.9
$2\ H_2 + O_2$ + 3.5 Ar	6.2	8.96	2.5
$2\ H_2 + O_2$ + 5.6 Ar	6.9	7.68	2.8
$H_2 + N_2O + 1.33\ N_2$	11.1	10.16	4.6
$H_2 + N_2O + 1.77\ N_2$	11.5	9.85	4.9
$C_2H_4 + 3\ O_2 + 8\ N_2$	12.4	9.8	6.1
$C_2H_4 + 3\ O_2 + 10.5\ N_2$	12.1	10.47	6.5
$C_3H_8 + 5\ O_2 + 9\ N_2$	12.7	11.8	8.0

Table 4.5 - Parameters for real mixtures (taken from Radulescu 2003)

Mixture	E	Induction/Reaction time
$CH_4 + 2\ O_2$	10.9	32.1
$C_3H_8 + 5\ O_2$	9.8	6.5
$C_2H_2 + 2.5\ O_2$	5.3	7.9
$C_2H_2 + 2.5\ O_2 + 22\%$ Ar	5.1	6.1
$C_2H_2 + 2.5\ O_2 + 50\%$ Ar	5.1	3.7
$C_2H_2 + 2.5\ O_2 + 60\%$ Ar	5.1	2.9
$C_2H_2 + 2.5\ O_2 + 65\%$ Ar	5.1	2.5
$C_2H_2 + 2.5\ O_2 + 70\%$ Ar	5.1	2.2
$C_2H_2 + 2.5\ O_2 + 75\%$ Ar	5.1	1.7
$2\ H_2 + O_2 + 25\%\ N_2$	5.2	1.4
$C_2H_2 + 2.5\ O_2 + 81\%$ Ar	5.1	1.4
$2\ H_2 + O_2$	4.9	1.4
$C_2H_2 + 2.5\ O_2 + 85\%$ Ar	5.2	1.1
$2\ H_2 + O_2 + 40\%$ Ar	4.2	0.6

modes of instability, and gives a starting point in understanding the dynamics of unstable detonations.

Chapter 5

Conclusion and Recommendations

In this study, the one-dimensional pulsating detonations were computed using a simplified two-step chain branching model. Using the two-step model, the dynamics of the induction zone and the main heat release zone were isolated and studied independently. In previous work on the one-step model, only low frequency pulsations have been observed. The two-step model is able to capture both the high frequency and low frequency modes of pulsations seen in realistic detonations, likely due to the presence of a clearly defined induction zone. The current work provided a method of examining the pulsating dynamics through the reconstruction of the families of characteristics. By tracking the trajectories of the pressure waves and particle paths, the physical behaviour of the pulsations can more easily be studied.

The present work clarified the underlying dynamics responsible detonation front pulsations. Four regimes of pulsations have been identified: the low frequency, high frequency, very high frequency and transition regimes.

The very high frequency instability involves a coupling between the weak compression waves originating from the end of the induction zone, and the reflected expansion wave originating from the shock front. The period of oscillation is well correlated by the sum of the time scales of the reflected expansion wave to move across the induction zone from the leading shock and the compression wave to move from the start of the reaction zone to the leading shock. The heat release rate determines the amount of amplification received by the compression wave originating from the start of the reaction zone, thus playing an important role in controlling the instability of the detonation. For slow heat release rates (and hence high reaction length to induction length ratios), the shock amplification received is small and thus the detonation becomes stable.

The instability of the high frequency mode is governed by a mechanism consistent

with Toong's mechanism for the square wave model. Similarly to Toong's mechanism, the period of oscillation is correlated by the sum of the time it takes for a compression wave to travel across the induction zone toward the shock, and the time it takes for a particle to travel from the shock toward the end of the induction zone. The heat release rate plays a similar role in governing instability as the very high frequency case. The heat release rate controls the amount of amplification received by the compression wave, and hence the stability of the detonation.

For the low frequency mode, where the reaction zone is much longer at the stability boundary than the high and very high frequency cases, the family of characteristics revealed that a broad region of compression waves were followed by a region of expansion waves, corresponding to a shortening of the induction zone and a lengthening of the detonation reaction zone respectively. The period of oscillation can be estimated by the time it takes for a particle path or C- characteristic to traverse the entire detonation length from the shock, plus the time it takes for a C+ characteristic to travel to the leading shock from the end of the reaction zone. However, it is unclear whether the C- or the particle path plays the more important role in determining the instability. The low frequency mode differs from the two higher frequency modes of pulsations in that the instability occurs across the entire reaction zone structure, whereas in the high frequency case, the instability occurs across only the induction zone.

In this work, numerical tools for studying the one-dimensional pulsating detonations have been developed for a two-step model for parameters corresponding to real mixtures. The existing method may be modified and the analysis repeated for simpler or more complicated models. Further insight can be obtained from implementing simpler models, for example Fickett's (1985) simplified analog for reactive flow, in which only two families of characteristics are present. The use of more complex models may be more appropriate for complex problems. For example, the current model is unable to idealize the behaviour of double structure detonations seen in supernovae (Fink et al. 2007) and gaseous nitromethane mixtures (Sturtzer et al. 2004), where the exothermic reactions occur in two separate steps. For this more complicated problem, another model must be implemented.

The current analysis is limited to the one-dimensional pulsating instability. However, in practice, the instability occurs in multiple dimensions and gives rise to cellular structures. The multi-dimensional instability can be studied by extending the present formulation to two dimensions. A tool can be implemented to visualize the unsteady motion of characteristic surfaces in 2D to study the wave dynamics in cellular detonations.

References

Alpert RL and Toong TY, *Periodicity in exothermic hypersonic flows about blunt projectiles*, Astronaut. Acta **17** (1972), 539-560

Austin JM, Pintgen F, and Shepherd JE, *Reaction zones in highly unstable detonations.* Proc. Combust. Inst. **30** (2005), 1849-1857

Bourlioux A, Majda AJ and Roytburd V, *Theoretical and numerical structure for unstable one- dimensional detonations.* SIAM J. Appl. Math. **51** (1991), 303-343

Buckmaster J and Neves J, *One-dimensional detonation stability: the spectrum for infinite activation energy.* Phys. Fluids **31** (1988), 3571-3576

Clavin P , and He L, *Stability and nonlinear dynamics of one-dimensional overdriven detonations in gases*, J. Fluid Mech. **306** (1996), 353-378

Clavin P, He L and Williams FA, *Multidimensional stability analysis of overdriven gaseous detonations.* Phys. Fluids **9** (1997), 3764-3785

Daimon Y and Matsuo A, *Detailed features of one dimensional detonations.* Phys. Fluids **15** (2002) 112-122

Daimon Y and Matsuo A, *Unsteady features on one-dimensional hydrogen-air detonations.* Phys. Fluids **19** (2007), 116101

Doering W, *On detonation processes in gases.* Ann. Phys. **43** (1943), 421-436

Erpenbeck JJ, *Stability of steady-state equilibrium detonations.* Phys. Fluids **9** (1962) 604-614

Fickett W, *Stability of the square-wave detonation in a model system.* Physica D **16** (1985) 358-370

Fickett W and Davis WC, "Detonation: Theory and Experiment." Dover Publications Inc., Mineola, New York, 1979

Fickett W and Wood WW, *Flow calculations for pulsating one-dimensional detonations.* Phys. Fluids **9** (1964) 903-916

Fink M, Hillebrandt W, Ropke FK, *Double-detonation supernovae of sub-Chandrasekhar mass white dwarfs.* Astron. Astrophys. **476** (2007) 1133-1143

Flynn MR, Kasimov AR, Nave JC, Rosales RR, Seibold B, *Self-sustained nonlinear waves in traffic flow.* Physical Review E **79** (2009) 056113

Gulen SC, Thompson PA, Cho HJ, *An experimental-study of reflected liquefaction shock-waves with near-critical downstream states in a test fluid of large molar heat-capacity.* J. Fluid Mech. **277** (1994) 163-196

Kasimov AR, *A stationary circular hydraulic jump, the limits of its existence and its gasdynamic analogue.* J.f Fluid Mech. **601** (2008) 189-198

Kasimov AR and Stewart DS, *On the dynamics of self-sustained one-dimensional detonations: A numerical study in the shock-attached frame.* Phys. Fluids **16** (2004) 3566-3578

Law CK, "Combustion Physics." Cambridge University Press, 2006

Lee JHS, "The Detonation Phenomenon." Cambridge University Press, 2008

Lee HI and Stewart DS, *Calculation of linear detonation instability: one-dimensional instability of planar detonations.* J. Fluid Mech., **216** (1990), 103–132

Lehr HF, *Experiments on shock-induced combustion.* Astronaut. Acta **17** (1972), 589-597

Leipmann HW and Roshko A, "Elements of Gasdynamics." John Wiley and Sons, Inc, New York, 1957

[a]Ng HD, Higgins AJ, Kiyanda CB, Radulescu MI, Lee JSH, Bates KR, Nikiforakis N, *Nonlinear dynamics and chaos analysis of one-dimensional pulsating detonations.* Combustion Theory and Modelling **9** (2005) 159-170

[b]Ng HD, Radulescu MI, Higgins AJ, Nikiforakis N, Lee JHS, *Numerical investigation of the instability for one dimensional Chapman–Jouguet detonations with chain-branching kinetics,* Combustion Theory and Modelling , **9** (2005), 385–401

Oran ES, *Astrophysical combustion.* Proc. of the Comb. Inst. **30** (2005) 1823-1840

Powers JM, Paolucci S, *Accurate spatial resolution estimates for reactive supersonic flow with detailed chemistry.* AIAA **43** (2005) 1088-1099

Quirk JJ (1998) AMRITA: A Computational Facility (for CFD Modeling). In "29th Computational Fluid Dynamics", von Karman Inst. Lecture Series, edited H. Deconinck

Radulescu MI, *The propagation and failure mechanism of gaseous detonations: experiments in porous-walled tubes.* Ph.D. Dissertation, McGill University, 2003

Roe PL, *Approximate Riemann Solvers, Parameter Vectors, and Difference Schemes.* J. Comput. Phys **43** (1981), 357-372

Sharpe GJ, *Linear Stability of idealized detonations.* Proc. R. Soc. Lond. A **453** (1997), 2603-2625

Sharpe GJ and Falle SAEG, *One-dimensional numerical simulations of idealized detonations.* Proc. R. Soc. Lond. A, **455** (1999), 1203-1214

Shchelkin KI, Troshin YK. trans. Kuvshinoff BW, Holtschlag L, "Gasdynamics of Combustion." Mono Book Corp. Baltimore, 1965

Short M, *A nonlinear evolution equation for pulsating Chapman–Jouguet detonations with chain- branching kinetics,* J. Fluid Mech. **430** (2001), 381–400

Short M, *An asymptotic derivation of the linear stability of the square-wave detonation using the Newtonian limit,* Proc. Royal Soc. Lond. A, **452** (1996), 2203-2224

Short M and Sharpe GJ, *Pulsating instability of detonations with a two-step chain-branching reaction model: theory and numerics.* Combustion Theory and Modelling, **7** (2003), 401–416.

Short M, and Quirk JJ, *On the nonlinear stability and detonability limit of a detonation wave for a model three-step chain-branching reaction.* J. Fluid Mech. **339** (1997), 89-119

Strehlow RA, *Gas phase detonations: recent developments,* Combust. Flame, **12** (1968) 81-101

Strogatz SH, "Nonlinear dynamics and Chaos: with applications to physics, biology, chemistry, and engineering." Perseus Books Pub. Reading, 1994

Sturtzer MO, Lamoureux N, Matignon C, Desbordes D, Presles HN, *On the origin of the double cellular structure of the detonation in gaseous nitromethane and its mixtures with oxygen.* Shock Waves **14** (2005) 45-51

Tumin A, *Initial-value problem for small disturbances in an idealized one-dimensional detonation,* Phys. Fluids, **19** (2007), 106105

von Neumann J, "Theory of detonation waves." ed. Taub AJ, in John von Neumann, collected works. MacMillan, New York, 1942

Whithan GB, "Linear and Nonlinear Waves." Wiley-Interscience, New York, 1974

Yoshikawa N, *Coherent shock wave amplification in photochemical initiation of gaseous detonations.* Ph.D. Dissertation, McGill University, 1980

Zaidel RM, *The stability of detonation waves in gaseous mixtures,* Dokl. Akad. Nauk SSSR, **136** (1961), 1142-1145

Zel'dovich IB, *On the theory of the propagation of detonation in gaseous systems,* Zh. Eksp. Teor. Fiz., **10** (1940) 542-568

Appendix A

Comparison of Different Scalings

It is desirable to compare the results obtained in this work with the results of Short and Sharpe (2003). However, the scalings used in the two studies were different, so it is necessary to find expressions that allow us to interchange between the two scalings. The following details the conversions needed to compare the results used in the two studies.

A.1 - Activation Energy and Heat Release

In this work, the activation energy and heat release were scaled by the post-shock temperature:

$$E=\frac{\tilde{E}}{R\tilde{T}_s}, Q=\frac{\tilde{Q}}{R\tilde{T}_s} \tag{A.1}$$

However, in Short and Sharpe (2003), the quantities have been scaled by the upstream quiescent temperature:

$$\bar{E}=\frac{\tilde{E}}{R\tilde{T}_o}, \bar{Q}=\frac{\tilde{Q}}{R\tilde{T}_o} \tag{A.2}$$

where $\bar{E}$ and $\bar{Q}$ are the dimensionless activation energy and heat release used by Short and Sharpe.

Knowing the parameters in terms of the scalings used in (A.2), one can then find the parameters in terms of the scalings used in this study, through the relation:

$$E=\frac{\tilde{T}_o}{\tilde{T}_s}\bar{E}, Q=\frac{\tilde{T}_o}{\tilde{T}_s}\bar{Q} \tag{A.3}$$

Knowing $\bar{Q}$, the CJ Mach number can be obtained (see Fickett and Davis 1979):

$$M_{CJ}=\sqrt{(1+\frac{\gamma^2-1}{\gamma}\bar{Q})+\sqrt{(1+\frac{\gamma^2-1}{\gamma}\bar{Q})^2-1}} \tag{A.4}$$

Knowing M_{CJ}, the ratio $\frac{\tilde{T}_o}{\tilde{T}_s}$ can be obtained through the Rankine Hugoniot jump conditions (see Leipmann and Roshko):

$$\frac{\tilde{T}_s}{\tilde{T}_o}=1+\frac{2(\gamma-1)}{(\gamma+1)^2}\frac{\gamma M_{CJ}^2+1}{M_{CJ}^2}(M_{CJ}^2-1) \tag{A.5}$$

Knowing the heat release and γ, the CJ Mach number, and hence the ratio $\tilde{T}_o/\tilde{T}_s$ can be found, thus giving a way to convert from the scalings used by Short and Sharpe to the scalings used in this study.

For example, Short and Sharpe used the parameters $\bar{Q}=4, \gamma=1.4$, which, from (A.4) gives $M_{CJ} = 2.711$, and then from (A.5) gives $T_s/T_o=2.355$. In terms of the scalings of this work, this gives a non-dimensional heat release of $Q=1.6988$.

A.2 - Reaction Rate Parameter, K_e

Due to the differences in the way time and velocity is scaled, the reaction rate parameter, K_e will also be scaled differently. The rate law for the reaction zone is:

$$\frac{D\lambda_e}{Dt}=(1-H(1-\lambda_i))K_e(1-\lambda_e)^\nu$$

In both works, the scaling used for length is the same (the induction zone length). In Short and Sharpe, the velocity is scaled by the detonation velocity, $\tilde{D}$. In this work, the scaling used for velocity is $\sqrt{\tilde{P}_s/\tilde{\rho}_s}$.

The scalings for K_e can be compared by the expression:

$$\frac{K_e}{\bar{K}_e}=\frac{\tilde{D}}{\sqrt{\tilde{P}_s/\tilde{\rho}_s}} \tag{A.6}$$

where $\bar{K}_e$ represents the reaction rate parameter in terms of the work of Short and Sharpe, and K_e is the reaction rate parameter in terms of this work.

For a perfect gas, $\tilde{c}=\sqrt{\frac{\gamma \tilde{p}}{\tilde{\rho}}}$. Using this, (A.6) can be rearranged in terms of more familiar variables:

$$\frac{K_e}{\bar{K}_e}=\frac{\sqrt{\gamma}\,\tilde{D}}{\tilde{c}_o}\frac{\tilde{c}_o}{\tilde{c}_s} \tag{A.7}$$

$$\frac{K_e}{\bar{K}_e}=M_{CJ}\sqrt{\gamma}\sqrt{\frac{\tilde{T}_o}{\tilde{T}_s}} \tag{A.8}$$

All of the parameters in (A.8) can be found knowing the non dimensional heat release.

In terms of the parameters used in Short and Sharpe, where $\bar{Q}=4, \gamma=1.4,$ the ratio in (A.6) becomes:

$$\frac{K_e}{\bar{K}_e}=2.090$$

For example, in Short and Sharpe, for $E = 10$, the stability boundary was found to be $\bar{K}_e=0.198$. In terms of the scalings used in this study, the stability boundary is $K_e=0.414$.

Appendix B

AMRITA Driver Script

The AMRITA script used for the numerical simulations of this study is contained here. In the contained script, the "utilize 2steplib" command directs AMRITA's solver to utilize the routines contained within the folder "2steplib". The code for the routines within this folder is contained in Appendix C.

A sample AMRITA script used to reconstruct the family of characteristics, with parameters $E = 10$, $Q = 10.3875$, $v = 0.5$, $\gamma = 1.2$ follow.

E10char

```
fold::amrita { 2step model 1D detonation dynamics
  fold::amrita { preliminaries
  ArraySizes {
    NGIxJ = 800000
    NGIJ  = 700000
  }
  }
  fold::amrita { define procedures
    fold::amrita { SetupZNDwave
      proc SetupZNDwave {
          fold::amrita { parameters
            fold::amrita { Physical detonation parameters
              gamma    =   1.2   # ratio of specific heats
              d [0:?]  =   1.6   # overdrive
              Q [0:50] =    8    # exothermic overall heat release
              E [0:100] =   3    # initiation activation energy
              ETA      =  0.8    # Reaction order
              Ke       =   2     # Reaction constant
            }
            fold::amrita { Grid and refinement parameters
              lmax     =    5    # maximum number of grid levels
              rI       =    2    # refinement ratio
              ptol     =   0.5   # packing tolernace
              Npts[0:?] =   64   # mesh points in half-reaction length
              im       =  400    # base grid points
              Zitol    =  0.0    # refinement tolerance on size of Zi
              Zetol    =  0.9999 # refinement tolerance on size of Ze
              Ptol     =  1.0    # refinement tolerance for pressure gradient
              Dtol1    =  1.1    # density based refinement tolerances:
              Dtol2    =  0.0001
              Dtol3    =  0.1
            }
            fold::amrita { Misc.
```

```
        dx       =    1.0    # fix half-reaction length
        Xd       =   100.0   # fix position of detonation
        piston_face=  -1E10    # trick interp with -infinity
        profiles "= znd    # directory for output of znd profiles
        chan     = 40        # fortran channel for output of znd files
      }
    }
  } -> %priv::
  fold::amrita { body of procedure
    fold::amr_sol'Domain {
     fold::amrita { get lscale
      set lscale #= 1.0/$Npts
      do l=$lmax,1,-1
       set lscale #= $lscale*$rl
      end do

     }
     lscale $lscale
     patch <1,+,w$im,h1>
    }
    fold::amr_sol'SolutionField {
     fold::amrita { fix problem specific quantities
       specify Q    ::= $Q
       specify E    ::= $E
       specify GAMMA ::= $gamma
       specify ETA  ::= $ETA
       specify Ke   ::= $Ke
     }
     fold::amrita { get W'znd
       fold::amrita { get znd
         ComputeZndProfile {
           <- %priv::
           rtn     = znd
           profiles = $profiles
           model   = 2ie
           Xc      = 4
           Zc      = 0.01
         }
       }
       Xd    ::= X[]-$Xd
       set zndfile = $amrita::cwd/$znd
       W'znd  ::= <RHO= interp($zndfile.RHO,Xd[]),\
                  U  = interp($zndfile.U  ,Xd[]),\
                  P  = interp($zndfile.P  ,Xd[]),\
                  Zi = interp($zndfile.Zi ,Xd[]),\
                  Ze = interp($zndfile.Ze ,Xd[])>
       fold::amrita { get initial density and pressure
         Dens ::= interp($zndfile.RHO,Xd[])
         Pres ::= interp($zndfile.P,Xd[])
         minmax Dens[] -> rho0, rhoshk
         minmax Pres[] -> P0, Pshk
         set Study::rho0 = $rho0
         set Study::P0   = $P0
```

```
          }
        }
        setfield W'znd
      }
      fold::amr_sol'BoundaryConditions {
        fold::amrita { get W'piston
          W'piston ::= <RHO= interp($znd.RHO,$piston_face),\
                       U  = interp($znd.U  ,$piston_face),\
                       P  = interp($znd.P  ,$piston_face),\
                       Zi = interp($znd.Zi ,$piston_face),\
                       Ze = interp($znd.Ze ,$piston_face)>
        }
        Ebdy domain: extrapolate
        Wbdy domain: prescribe W'piston
      }
      fold::amr_sol'RefinementCriteria {
        #setflags [ooo|oxo|ooo] abs(Zi[])>$Zitol && (RHO[]>$Dtol1*$rho0)
        setflags [ooo|oxo|ooo] abs(Ze[])<$Zetol && (RHO[]>$Dtol1*$rho0)
        setflags [ooo|xxx|ooo] abs(RHO[+i]-RHO[])>$Dtol2 && abs(Zi[]>0.99)
        setflags [ooo|xxx|ooo] abs(RHO[+i]-RHO[])>$Dtol3
        setflags [ooo|xxx|ooo] abs(P[+i]-P[])>$Ptol
      }
      fold::amr_sol'MeshAdaption {
        adaption  on
        lmax     $lmax
        rI       $rI
        ptol     $ptol
      }
      makefield {G$lmax}
    }
  end proc
}
fold::amrita { GetInput
  proc GetInput {
     fold::amrita { parameters
       case  = E10char
       data  = default
       chars = default
       tokp  = Study::
     }
   }
   fold::amrita { body of procedure
     tokenpath +-> $tokp -> %caller::
     fold::amrita { get physical parameter set
     switch on $case
       default:
         fold::amrita { Carlos's initial parameters
           set gamma = 1.2
           set d     = 1.0
           set Q     = 10.3875
           set E     = 10.0
           set ETA   = 0.5
           set Ke    = 0.2
```

```
        }
    end switch
    }
    fold::amrita { set other input data
    switch on $data
      default:
        fold::amrita { Carlos's test parameters
          set Npts   = 256
          set im     = 8000
          set lmax   = 8
          set nphases = 500
          set ncycles = 100
          set nsteps  = 10
          set cfl    = 0.4
          set ilim   = 7
          set delt   = 0.02
          set Zitol    =   0.0   # refinement tolerance on size of Zi
          set Zetol    =   0.9999   # refinement tolerance on size of Ze
          set Ptol     =   1.0   # refinement tolerance for pressure gradient
          set Dtol1    =   1.1   # density based refinement tolerances:
          set Dtol2    =   0.0001
          set Dtol3    =   0.1
          set Xtol     =   10.0  # refinement behind reaction zone
        }
  end switch
  }
  fold::amrita { set Characteristic data
    switch on $chars
      default:
        fold::amrita { Characteristic starting points
          set chan  = 30
          set nchars= 200
          do i = 1,$nchars-90 #chars in the back
            set bc$i #= 30 + 5*$i
          end do
          do i = 1,$nchars
            set pc$i #= 79.9+0.1*$i
          end do
          do i = 1,$nchars
            set mc$i #= 9190+10*$i
          end do
          do i = 1,$nchars
            set uc$i #= 4450 + 10*$i
          end do
          set nc1  = 0
          set nc2  = 10
          set nc3  = 100
        }
    end switch
  }
  set study   = $case
  set phistory = chars/Phist.dat
  set ihistory = chars/Ihist.dat
```

```
      set ps      = ps/Phist.ps
    }
  end proc
}
fold::amrita { FindUplusC
  proc FindUplusC {
    fold::amrita { parameters
      code   = code
      package = uplusc
      chan   = 30
      xc     = 0
    }
  }
  fold::amrita { body of procedure
    if(missing::amrso("$code/$package")) then
      fold::amrita { build it
        pushcwd $code
          fold::amrf77 { here
            fold> amrso=$package
            fold::amrf77 { SUBROUTINE FIND_UPLUSC
                SUBROUTINE FIND_UPLUSC
                fold::amrf77 { variable declarations
                    AMRITA_TYPING
                    AMRDBL XC, X1, X2, UPC, UPC1, UPC2
                    AMRINT I, CHAN
                }
                CALL AMR_GET_TOKEN('AMRINT:chan',CHAN)
                CALL AMR_GET_TOKEN('AMRDBL:xc',XC)
                READ(CHAN,*,END=100) X1, UPC1
                DO I=1,999999
                  READ(CHAN,*,END=100) X2, UPC2
                  IF (X1.LE.XC.AND.X2.GT.XC) THEN
                    UPC=(XC-X1)/(X2-X1)
                    UPC=UPC*(UPC2-UPC1)+UPC1
                    GOTO 200
                  ENDIF
                  X1   = X2
                  UPC1 = UPC2
                ENDDO
              100  UPC = 0.0
              200  CLOSE(CHAN)
                  CALL AMR::SET_TOKEN('AMRDBL::char::upc',UPC)
                  RETURN
                  END
            }
          }
        popcwd
      }
    endif
    export chan,xc
    call $code/$package`::find_uplusc
    import char::{upc}
}
```

```
    end proc
  }
  fold::amrita { FindUminusC
    proc FindUminusC {
       fold::amrita { parameters
         code   = code
         package = uminusc
         chan   = 30
         xc     = 0
       }
     }
     fold::amrita { body of procedure
       if(missing::amrso("$code/$package")) then
         fold::amrita { build it
           pushcwd $code
             fold::amrf77 { here
               fold> amrso=$package
               fold::amrf77 { SUBROUTINE FIND_UMINUSC
                   SUBROUTINE FIND_UMINUSC
                   fold::amrf77 { variable declarations
                       AMRITA_TYPING
                       AMRDBL XC, X1, X2, UMC, UMC1, UMC2
                       AMRINT I, CHAN
                   }
                   CALL AMR_GET_TOKEN('AMRINT:chan',CHAN)
                   CALL AMR_GET_TOKEN('AMRDBL:xc',XC)
                   READ(CHAN,*,END=100) X1, UMC1
                   DO I=1,999999
                     READ(CHAN,*,END=100) X2, UMC2
                     IF (X1.LE.XC.AND.X2.GT.XC) THEN
                       UMC=(XC-X1)/(X2-X1)
                       UMC=UMC*(UMC2-UMC1)+UMC1
                       GOTO 200
                     ENDIF
                     X1  = X2
                     UMC1 = UMC2
                   ENDDO
               100  UMC = 0.0
               200  CLOSE(CHAN)
                   CALL AMR::SET_TOKEN('AMRDBL::char::umc',UMC)
                   RETURN
                   END
               }
             }
           popcwd
         }
       endif
       export chan,xc
       call $code/$package`::find_uminusc
       import char::{umc}
     }
   end proc
}
```

```
fold::amrita { FindUparticle
  proc FindUparticle {
     fold::amrita { parameters
       code    = code
       package = uparticle
       chan    = 30
       xc      = 0
     }
   }
   fold::amrita { body of procedure
     if(missing::amrso("$code/$package")) then
       fold::amrita { build it
         pushcwd $code
           fold::amrf77 { here
             fold> amrso=$package
             fold::amrf77 { SUBROUTINE FIND_UPARTICLE
                 SUBROUTINE FIND_UPARTICLE
                 fold::amrf77 { variable declarations
                     AMRITA_TYPING
                     AMRDBL XC, X1, X2, UPARTICLE, UPARTICLE1, UPARTICLE2
                     AMRINT I, CHAN
                 }
                 CALL AMR_GET_TOKEN('AMRINT:chan',CHAN)
                 CALL AMR_GET_TOKEN('AMRDBL:xc',XC)
                 READ(CHAN,*,END=100) X1, UPARTICLE1
                 DO I=1,999999
                   READ(CHAN,*,END=100) X2, UPARTICLE2
                   IF (X1.LE.XC.AND.X2.GT.XC) THEN
                     UPARTICLE=(XC-X1)/(X2-X1)
                     UPARTICLE=UPARTICLE*(UPARTICLE2-UPARTICLE1)+UPARTICLE1
                     GOTO 200
                   ENDIF
                   X1  = X2
                   UPARTICLE1 = UPARTICLE2
                 ENDDO
             100  UPARTICLE = 0.0
             200  CLOSE(CHAN)
                 CALL AMR::SET_TOKEN('AMRDBL::char::uparticle',UPARTICLE)
                 RETURN
                 END
             }
           }
         popcwd
       }
     endif
     export chan,xc
     call $code/$package`::find_uparticle
     import char::{uparticle}
   }
  end proc
 }
}
utilize 2steplib
```

```
  plugin amr_sol
  ReactiveEulerEquations {
    model = 2ie
    space = 1D
  }
  fold::amrita { load solver
    fold::amrita { build solver?
      if(&missing::amrso("code/2step")) then
        fold::amrita { yes
          BasicCodeGenerator {
            scheme  = roe'3cb
            solver  = 2step
          }
        }
      endif
    }
    fold::amrita { set solver parameters
      set solver::PHI  = 1
      set solver::Pact = 0.3
      export solver::{PHI,Pact}
    }
    solver code/2step
}
fold::amrita { generate characteristics
  GetInput
  fold::amrita { Initialize characteristic C+ and C- files
    do i=1,$nchars
      set pfile$i "= chars/pchar\$pc$i
      expand pfile$i
    enddo
    do i=1,$nchars
      set mfile$i "= chars/mchar\$mc$i
      expand mfile$i
    enddo
    do i=1,$nchars
      set ufile$i "= chars/uchar\$uc$i
      expand ufile$i
    enddo
    set t0 = 0
}
foreach KE (0.150)
    echo $KE
    fold::amrita { create characteristics for this case
      set Study::Ke = $KE
      pushcwd results/$study/Ke$Study::Ke
      SetupZNDwave <- Study::
      fold::amrita { setup logfile
        logfile logs/log
      }
      fold::amrita { march and generate pressure records
      do n=1,$nphases
        fold::amrita { generate spatial profiles
          foreach Q (P,RHO,U,Zi,Ze)
```

```
        printfile profiles/$Q$n
          along y=0 print {G} X[],$Q[]
        printfile
      end foreach
    }
    echo $n
    do ns=1,$ncycles
      march 1 steps with dt=$delt
      def RefinementCriteria
        set rxnzone "= first Ze[] < $Zetol
        along y = 0 locate $rxnzone -> Xr #Xr is location of reaction zone
        setflags [ooo|xxx|ooo] X[] > $Xr-$Xtol && (RHO[]>$Dtol1*$Study::rho0)
        setflags [ooo|xxx|ooo] abs(RHO[+i]-RHO[])>$Dtol2 && abs(Zi[]>0.99)
        setflags [ooo|xxx|ooo] abs(RHO[+i]-RHO[])>$Dtol3
        setflags [ooo|xxx|ooo] abs(P[+i]-P[])>$Ptol
      end def
      fold::amrita { record shock pressure
        set shock_loc "= last P[]>1.1*$Study::P0
        set window #= $ilim/$Npts
        along y=0 locate $shock_loc -> Xshk
        along y=0 maximum X[],P[] for ($Xshk-X[])< $window -> loc, val
        time -> t
        set xf1a #= $loc - $znd::D0*$t
        set xf1b #= $Xshk - $znd::D0*$t
        fold::print { save to file
          fold> file.=$phistory
          $loc $val $t $xf1a $xf1b
        }
      }
      fold::amrita { record end of induction location
        #xf2a is shock location, xf2b is induction end, xf2c is reaction end
        set ind_loc "= last Zi[] > 0
        set ind_end "= first Zi[] > 0
        set rxn_end "= first Ze[] < 0.9999
        set iwindow #= $ilim/$Npts
        along y=0 locate $ind_loc -> Xind
        along y=0 locate $ind_end -> Xend
        along y=0 locate $rxn_end -> Rend
        along y=0 maximum X[],Zi[] for ($Xshk-X[]) < $window -> loc,val
        time -> t
        set xf2a #= $loc - $znd::D0*$t
        set xf2b #= $Xend - $znd::D0*$t
        set xf2c #= $Rend - $znd::D0*$t
        fold::print { save to file
          fold> file.=$ihistory
          $loc $t $xf2a $xf2b $xf2c
        }
    }
    fold::amrita { update characteristic paths
      fold::amrita { generate spatial profiles
        C ::= sqrt(GAMMA[]*P[]/RHO[])
        PCHAR ::= U[]+C[]
        foreach Q (PCHAR)
```

```
        printfile profiles/uplusc
          along y=0 print {G} X[],$Q[]
        printfile
      end foreach
      MCHAR ::= U[]-C[]
      foreach Q (MCHAR)
        printfile profiles/uminusc
          along y=0 print {G} X[],$Q[]
        printfile
      end foreach
      UCHAR ::= U[]
      foreach Q(UCHAR)
        printfile profiles/uparticle
          along y=0 print {G} X[],$Q[]
        printfile
      end foreach
    }
    do i = 1,$nchars
      set xc = \$pc$i
      expand xc
      fold::amrita { get U+C at current xc
        chan($chan,f,r) profiles/uplusc
        FindUplusC chan=$chan, xc=$xc
      }
      fold::amrita { Update charateristic position
        set pc$i #= $char::upc*($t-$t0)+$xc
      }
      fold::amrita { Update characteristic path file
          set pfile = \$pfile$i
          expand pfile
          set xc = \$pc$i
          expand xc
          set xcs1 #= $xc-$loc
          set xcs2 #= $xc-$znd::D0*$t
          fold::print { Update characteristic path file
            fold> file.=$pfile
            $t $xc $xcs1 $xcs2
          }
    }
  end do
  do i = 1,$nchars
    set xc = \$mc$i
    expand xc
    fold::amrita { get U-C at current xc
      chan($chan,f,r) profiles/uminusc
      FindUminusC chan=$chan, xc=$xc
    }
    fold::amrita { Update charateristic position
      set mc$i #= $char::umc*($t-$t0)+$xc
    }
    fold::amrita { Update characteristic path file
        set mfile = \$mfile$i
        expand mfile
```

```
                    set xc = \$mc$i
                    expand xc
                    set xcs1 #= $xc-$loc
                    set xcs2 #= $xc-$znd::D0*$t
                    fold::print { Update characteristic path file
                      fold> file.=$mfile
                      $t $xc $xcs1 $xcs2
                    }
                  }
                end do
                do i = 1,$nchars
                  set xc = \$uc$i
                  expand xc
                  fold::amrita { get U at current xc
                    chan($chan,f,r) profiles/uparticle
                    FindUparticle chan=$chan, xc=$xc
                  }
                  fold::amrita { Update charateristic position
                    set uc$i #= $char::uparticle*($t-$t0)+$xc
                  }
                  fold::amrita { Update characteristic path file
                      set ufile = \$ufile$i
                      expand ufile
                      set xc = \$uc$i
                      expand xc
                      set xcs1 #= $xc-$loc
                      set xcs2 #= $xc-$znd::D0*$t
                      fold::print { Update characteristic path file
                        fold> file.=$ufile
                        $t $xc $xcs1 $xcs2
                      }
                  }
                end do
                set t0 = $t
              }
            enddo
          end do
          popcwd
          }
        }
    end foreach
  }
}
```

Appendix C

Modified Routines in AMRITA

The existing AMRITA routines used by Short and Quirk (1997) for the three-step chain branching model was adapted and modified for the two-step model. The modified routines for the two-step model used by AMRITA are outlined here.

ComputeZndProfile.amr is the AMRITA procedure used to initialize the simulation by computing the ZND profile and the pre-exponential factor of the induction zone, K_i. The equations were modified so that the integration is carried out using the equations of the two-step model.

ReactiveEulerEquations.amr is the equation set used by AMRITA, and gives a mapping of how the physical variables (e.g. pressure, density, velocity) are extracted from the computational domain. Further details can be found in the AMRITA VKI lecture series (Quirk 1998). The equation set defined by ReactiveEulerEquations.amr were modified for the two-step model.

PartialDerivatives.amr, SourceTerms.amr and Startup.amr are procedures used by AMRITA's flow solver. The fluxes calculated in PartialDerivatives.amr, equations of SourceTerms.amr and the variables used in Startup.amr were rewritten to fit the two-step model.

AmritaUtilize.amr

```
proc AmritaUtilize
  fold::amrita { body of procedure
    autopath <stdlib> ++$amrita::thisdir/bcg/2ie
    autopath <stdlib> ++$amrita::thisdir/stdlib
  }
end proc
```

ComputeZndProfile.amr

```
proc ComputeZndProfile {
   fold::amrita { parameters
     model   = 1a
     code    = code
```

```
      package  = znd
      chan     = 20      # base output channel
      d        = 1.2     # overdrive
      Npts     = 100     # number of points in half-reaction
      Xc       = 4       # X cut-off point
      Zc       = 0.00001 # Z cut-off point
      io       = znd
      profiles"= $io
      header   = znd
      doc
      profile "= $io/$header
      rtn
    }
  } <-> znd::
  fold::amrita { body of procedure
    fold::amrita { check symmetry
      switch on $amrita:EquationSet::symmetry
        case slab:
        default:
          error ZndProfile is restricted to slab symmetry
          exit
      end switch
    }
    switch on $model
      case 2ie:
        fold::amrita { two-step chain-branching
          export znd::{d,Npts,Zc,Xc,chan}
          fold::amrita { open channels
            foreach q (RHO, U, P, Zi, Ze, T)
              chan($chan,f,w) $profiles/$znd::header\.$q
              set chan += 1
            end foreach
            if(token(rtn)) then
              set ^$rtn = $profiles/$znd::header
            end if
          }
          fold::amrita { build package?
            if(missing::amrso("code/$package")) then
              fold::amrita { yes
                pushcwd $code
                fold::amrf77 { compile package
                  fold>amrso=$package
                  fold::amrf77 { GEN_PROFILES
                  C
                  C    GENERATE ZND PROFILES FOR THREE-STEP CHAIN-BRANCHING
KINETICS
                  C
                      SUBROUTINE GEN_PROFILES
                  fold::amrf77 { variable declarations
                      AMRITA_TYPING
                      AMRDBL K,Knew,INTEGRATE
                      AMRDBL Ki,Kb,Kc,Ke,Xscl
                      AMRINT AMR::LOGFILE,CHAN
```

```
                }
                C
                C   GET INPUT VARIABLES
                C
                    RKi = -1
                    CALL AMR::GET_TOKEN('AMRDBL:znd::d',ODF)          /* OVERDRIVE
*/
                    CALL AMR::GET_CONST('amrita:EquationSet:expr::Ke',Ke)  /* Reaction Constant
*/
                    CALL AMR::GET_CONST('amrita:EquationSet:expr::E',E)    /* Activation Energy
*/
                    CALL AMR::GET_CONST('amrita:EquationSet:expr::Q',Q)    /* Heat Release
*/
                    CALL AMR::GET_CONST('amrita:EquationSet:expr::ETA',ETA) /* Reaction order
*/
                    CALL AMR::GET_CONST('amrita:EquationSet:expr::GAMMA',G) /* RATIO OF
SPECIFIC HEATS    */
                    CALL AMR::GET_TOKEN('AMRINT:znd::Npts',Npts)          /* NUMBER OF
POINTS IN PROFILE */
                    CALL AMR::GET_TOKEN('AMRINT:znd::chan',CHAN)          /* BASE OUTPUT
CHANNEL NUMBER  */
                    CALL AMR::GET_TOKEN('AMRDBL:znd::Zc',Zc)             /* CUT-OFF POINT
FOR REACTION  */
                    CALL AMR::GET_TOKEN('AMRDBL:znd::Xc',Xc)             /* X CUT-OFF
POINT          */
                    CALL AMR::GET_TOKEN('?AMRDBL:znd::RKi',RKi)          /* Reference value
for RKi    */

                    WRITE(AMR::LOGFILE(),*) 'GENERATING 3 REACTION ZND PROFILE'
                    WRITE(AMR::LOGFILE(),*) '--------------------------'
                    WRITE(AMR::LOGFILE(),*) ' '
                    WRITE(AMR::LOGFILE(),*) 'f  =',ODF
                    WRITE(AMR::LOGFILE(),*) 'E =',E
                    WRITE(AMR::LOGFILE(),*) 'Q =',Q
                    WRITE(AMR::LOGFILE(),*) 'ETA =',ETA
                    WRITE(AMR::LOGFILE(),*) 'Ke =',Ke
                    WRITE(AMR::LOGFILE(),*) 'GM =',G
                    WRITE(AMR::LOGFILE(),*) 'Np =',Npts

                    DCJ=1.+(G*G-1.)*Q/G
                    DCJ=SQRT(DCJ-SQRT(DCJ*DCJ-1.))
                    DCJ=SQRT(((G-1.)*DCJ*DCJ+2.)/(2.*G*DCJ*DCJ-G+1.))
                    DM=SQRT(ODF)*DCJ

                    WRITE(AMR::LOGFILE(),*) ' '
                    WRITE(AMR::LOGFILE(),*) 'Mcj=',DCJ
                    WRITE(AMR::LOGFILE(),*) 'Ms =',DM

                    Pvn = (2.0 D0*G*DM*DM-(G-1.0 D0))/(G+1.0 D0)
                    GG  = (G+1.0 D0)/(G-1.0 D0)
                    Dvn = (GG*Pvn+1.0 D0)/(GG+Pvn)
                    Ds  = DM*SQRT(DVn/PVn)
                    WRITE(*,*) DS
```

```
c -- evaluate reaction constants -------

      DMS = SQRT(((G-1.)*DM*DM+2.)/(2.*G*DM*DM-G+1.))
      A = (G*DMS*DMS+1.)/(G+1.)
      B = DMS*DMS*2.*G*(G-1.)/((1.-A)*(1.-A)*(G+1.))

      PCJ = A+(1-A)*SQRT(ABS(1.-B*Q))
      UCJ = (1.-PCJ)/(G*DMS)+DMS
      VCJ = UCJ/DMS
         PRINT*,PCJ,1.0/VCJ
      DX   = 0.001 D0
      RS   = 1.0 D0
      Ftol = 0.05 D0
      Ytol = 1.0 D-4

  100 CONTINUE

      X     = 0.0 D0
      NSTEPS = 0

c -- initial values

      VR = 1.
      UR = DMS
      PR = 1.
      FR = 1.
      YR = 0.
      TR = PR*VR

c -- store initial values

 10    VRL = VR
       URL = UR
       PRL = PR
       FRL = FR
       YRL = YR
       TRL = TR

 200 CONTINUE
     CALL AMR::SET_TOKEN('AMRDBL:znd::K',K)
     CALL AMR::SET_TOKEN('AMRDBL:znd::nu',1.0 D0)
C
C    PRODUCE THE PROFILES
C
     DXtarget= 1.0 D0/FLOAT(256)
     Xtarget =-DXtarget/2.0 D0
     Xold    =-DXtarget
     X       = 0.0 D0
     Nprof   = 1
     Dinf    = 1.0 D0/Dvn
     Uinf    = 0.0 D0
     Pinf    = 1.0 D0/Pvn
```

```
      Finf   = 1.0 D0
      Yinf   = 0.0 D0
      D0     = Ds*SQRT(G)
      Ki     = URL/(EXP(-E/TRL))*SQRT(G)
      IF(RKi.GT.0) THEN
        Xscl   = Ki/RKi
      ELSE
        Xscl   = 1
      ENDIF
      PRINT*,Xscl
      WRITE(CHAN,*)  -Xold*Xscl,Dinf
      WRITE(CHAN+1,*) -Xold*Xscl,Uinf
      WRITE(CHAN+2,*) -Xold*Xscl,Pinf
      WRITE(CHAN+3,*) -Xold*Xscl,Finf
      WRITE(CHAN+4,*) -Xold*Xscl,Yinf
      WRITE(CHAN+5,*) -Xold*Xscl,Pinf/Dinf

c -- initial values

      VR = 1.
      UR = DMS
      PR = 1.
      FR = 1.
      YR = 0.
      TR = PR*VR

c -- store initial values

  300 CONTINUE
      VRL = VR
      URL = UR
      PRL = PR
      FRL = FR
      YRL = YR
      TRL = TR

      QR = Q*(YR)

      IF (FR.GT.0.D0) THEN
        FX1 = -(Ki*EXP(-E/TR))/UR/SQRT(G)
        YX1 = 0
      ELSE
        FX1 = 0
        YX1 = MAX(0.0 D0,(Ke*(1-YR)**ETA)/UR/SQRT(G))
      END IF
      QX1 = Q*YX1
      PX1 = -(B/2.)*(1.-A)*QX1/SQRT(ABS(1.-B*QR))
      UX1 = -PX1/(G*DMS)
      VX1 = -PX1/(G*DMS*DMS)

      VR = VR+DX*VX1
      UR = UR+DX*UX1
      PR = PR+DX*PX1
```

```
      FR = MAX(0.0 D0,FR+DX*FX1)
      YR = YR+DX*YX1
      TR = PR*VR

      QR = Q*(YR)

      IF (FR.GT.0.D0) THEN
        FX2 = -(Ki*EXP(-E/TR))/UR/SQRT(G)
        YX2 = 0
      ELSE
        FX2 = 0
        YX2 = MAX(0.0 D0,(Ke*(1-YR)**ETA)/UR/SQRT(G))
      END IF
      QX2 = Q*YX2
      PX2 = -(B/2.)*(1.-A)*QX2/SQRT(ABS(1.-B*QR))
      UX2 = -PX2/(G*DMS)
      VX2 = -PX2/(G*DMS*DMS)
      VR = VRL+(VX1+VX2)*DX/2.
      UR = URL+(UX1+UX2)*DX/2.
      PR = PRL+(PX1+PX2)*DX/2.
      FR = MAX(0.0 D0,FRL+(FX1+FX2)*DX/2.)
      YR = YRL+(YX1+YX2)*DX/2.
      TR = PR*VR
      X  = X+DX
      XX = X
      IF((X.GT.Xtarget).AND.(Xold.LT.Xtarget)) THEN
        WRITE(CHAN,*)   -XX*Xscl,1./VR
        WRITE(CHAN+1,*) -XX*Xscl,(Ds-UR)*SQRT(G)
        WRITE(CHAN+2,*) -XX*Xscl,PR
        WRITE(CHAN+3,*) -XX*Xscl,FR
        WRITE(CHAN+4,*) -XX*Xscl,YR
        WRITE(CHAN+5,*) -XX*Xscl,PR*VR
        Xtarget = Xtarget+DXtarget
        Nprof   = Nprof+1
      ENDIF
      Xold = X
      IF(YR.LE.1.D0) GO TO 300
      IF(X.LT.Xc) GO TO 300
        XX = X+DX
        WRITE(CHAN,*)   -XX*Xscl,1./VCJ
        WRITE(CHAN+1,*) -XX*Xscl,(Ds-UCJ)*SQRT(G)
        WRITE(CHAN+2,*) -XX*Xscl,PCJ
        WRITE(CHAN+3,*) -XX*Xscl,0
        WRITE(CHAN+4,*) -XX*Xscl,1
        WRITE(CHAN+5,*) -XX*Xscl,PCJ*VCJ
        Nprof   = Nprof+1

      CALL AMR::SET_TOKEN('AMRDBL:znd::Xd',X)
      CALL AMR::SET_TOKEN('AMRDBL:znd::Ki',Ki)
      CALL AMR::SET_TOKEN('AMRDBL:znd::D0',D0)
      CALL AMR::SET_TOKEN('AMRDBL:znd::Ds',Ds)
      DO N=0,5
        CLOSE(CHAN+N)
```

```
                    END DO
                    RETURN
                    END
                  }
                }
                popcwd
              }
            endif
          }
          call $code/$package`::gen_profiles
          import znd::{Xd,Ki,Ds,D0}
          specify Ki ::= $znd::Ki
        }
      default:
        error can't compute znd profile for $model reaction model
    end switch
  }
end proc
```

ReactiveEulerEquations.amr

```
proc ReactiveEulerEquations {
   fold::amrita { parameters
     space = one-dimensional
     symmetry {slab|cylindrical|spherical} = slab
     model = 2ie          # reaction model
     gamma = 1.2          # ratio of specific-heats
     Q    = 3       # heat release in exothermic zone
     E    = 3       # activation energy of induction zone
     ETA   = 0.5     # rate reaction order
     Ki    = 1.0     # pre-exponential factor
     Ke    = 1.0     # rate constant for exothermic zone
     add2W
     bcg
   }
 } -> znd::
 switch on $model
   case 2ie:
     fold::amrita'm_2ie { two-step induction/exothermic model
       switch on $space
         case 1D:one-dimensional:
           fold::amrita'space1D { 1D EquationSet
             def EquationSet
               name    $amrita::proc0
               space   one-dimensional
               symmetry $symmetry
               neqns   6
               notation RHO,U,P,Zi,Ze,GAMMA
               notation Q,Ki,Ke,ETA,E
               problem specific GAMMA,Q,Ki,Ke,ETA,E
               def SolutionVector
                 require RHO,U,P,Zi,Ze,GAMMA,Q
```

```
            hint precompute P
            W[1] ::= RHO[]
            W[2] ::= RHO[]*U[]
            W[3] ::= 0
            W[4] ::= P[]/(GAMMA[]-1)+0.5*RHO[]*U[]**2\
                  -RHO[]*(Ze[]*Q[])
            W[5] ::= RHO[]*Zi[]
            W[6] ::= RHO[]*Ze[]
            RHO  ::= W[1]
            U    ::= W[2]/W[1]
            P    ::= (GAMMA[]-1)*(W[4]-0.5*(W[2]*W[2])/W[1]+W[6]*Q[])
            Zi   ::= W[5]/W[1]
            Ze   ::= W[6]/W[1]
            specify GAMMA::= $gamma
            specify Q    ::= $Q
            specify ETA  ::= $ETA
            specify Ki   ::= $Ki
            specify Ke   ::= $Ke
            specify E    ::= $E
          end def
        end def
      }
    case 2D:two-dimensional:
      fold::amrita'space2D { 2D EquationSet
        def EquationSet
          name     $amrita::proc0
          space    two-dimensional
          symmetry $symmetry
          neqns    6
          notation RHO,U,V,P,Zi,Ze,GAMMA
          notation Q,Ki,Ke,ETA,E
          problem specific GAMMA,Q,Ki,Ke,ETA,E
          def SolutionVector
            require RHO,U,V,P,Z,GAMMA,Q
            hint precompute P
            notation RHO,U,P,Zi,Ze,GAMMA
            notation Qi,Q,Ki,Ke,ETA,E
            problem specific GAMMA,Q,Ki,Ke,ETA,E
            def SolutionVector
            require RHO,U,V,P,Zi,Ze,GAMMA,Q
            hint precompute P
            W[1] ::= RHO[]
            W[2] ::= RHO[]*U[]
            W[3] ::= RHO[]*V[]
            W[4] ::= P[]/(GAMMA[]-1)+0.5*RHO[]*(U[]**2+V[]**2)\
                  +RHO[]*(Ze[]*Q[])
            W[5] ::= RHO[]*Zi[]
            W[6] ::= RHO[]*Ze[]
            RHO  ::= W[1]
            U    ::= W[2]/W[1]
            V    ::= W[3]/W[1]
            P    ::= (GAMMA[]-1)*(W[4]-0.5*(W[2]*W[2])/W[1]\
                  -W[6]*Q[])
```

```
                Zi  ::= W[5]/W[1]
                Ze  ::= W[6]/W[1]
                specify GAMMA::= $gamma
                specify Q   ::= $Q
                specify ETA ::= $ETA
                specify Ki  ::= $Ki
                specify Ke  ::= $Ke
                specify E   ::= $E
              end def
            end def
          }
        default:
          error "$space" space unknown by ReactiveEulerEquations!
      end switch
    }
  end switch
end proc
```

PartialDerivatives.amr

```
proc PartialDerivatives
  CodeManifest addfile=$amrita::thisfile
  fold::print {
   ***********************************************************************
   *  THE FOLLOWING ROUTINES ARE EOS/REACTION MODEL DEPENDENT  *
   ***********************************************************************
   *
   *    P = (GMz-1)*(D*i-D*Q*y)
   *
   *
   *    FN_P:  COMPUTE PRESSURE AS A FUNCTION OF
   *    DENSITY, INTERNAL ENERGY AND MASS FRACTIONS
   *
   *
       AMRDBL FUNCTION FN_P(D,i,Z)
       AMRITA_TYPING
  #include "$amrita:bcg::commonblk"
       AMRDBL D,i,Z(NMF)
       FN_P = (GMz-1.0 D0)*(D*i+D*Q*Z(2))
       RETURN
       END
   *
   *
   *    FN_Pi: COMPUTE RATE OF CHANGE OF PRESSURE
   *    W.R.T. INTERNAL ENERGY
   *
   *
       AMRDBL FUNCTION FN_Pi(D,i,Z)
       AMRITA_TYPING
  #include "$amrita:bcg::commonblk"
       AMRDBL D,i,Z(NMF)
       FN_Pi = (GMz-1.0 D0)*D
       RETURN
```

```
        END
       *
       *
       *    FN_Pr: COMPUTE RATE OF CHANGE OF PRESSURE
       *    W.R.T. DENSITY
       *
       *
        AMRDBL FUNCTION FN_Pr(D,i,Z)
        AMRITA_TYPING
      #include "$amrita:bcg::commonblk"
        AMRDBL D,i,Z(NMF)
        FN_Pr = (GMz-1.0 D0)*(i+(Q)*Z(2))
        RETURN
        END
      *
      *
      *    FN_Pz: COMPUTE RATE OF CHANGE OF PRESSURE
      *    W.R.T. MASS FRACTION N
      *
      *
        AMRDBL FUNCTION FN_Pz(N,D,i,Z)
        AMRITA_TYPING
     #include "$amrita:bcg::commonblk"
        AMRDBL D,i,Z(NMF)
        IF(N.EQ.1) FN_Pz= 0
        IF(N.EQ.2) FN_Pz=(GMz-1.0 D0)*D*Q
        RETURN
        END
  }
end proc
```

SourceTerms.amr

```
proc SourceTerms
  CodeManifest addfile=$amrita::thisfile
  AddIntegrationStep {
    step = source (aka Ls) : SOURCE_TERMS(IM,JM,NG,DT,S,W)
  }
  fold::print {
    *
    *
    *    SOURCE_TERMS:
    *
    *
        SUBROUTINE SOURCE_TERMS(IM,JM,NG,DT,S,W)
        AMRITA_TYPING
   #include "$amrita:bcg::commonblk"
        AMRDBL S(NW,amrCpatch(IM,JM,NG))
        AMRDBL W(NW,amrCpatch(IM,JM,NG))
        CALL SOURCES(IM,JM,NG,DT,S,W)
        CALL S_UPDATE(IM,JM,NG,S,W)
        RETURN
```

```
      END
*
*
*     SOURCES: CALCULATE SOURCE TERMS
*
*
      SUBROUTINE SOURCES(IM,JM,NG,DT,S,W)
      AMRITA_TYPING
#include "$amrita:bcg::commonblk"
      AMRDBL S(NW,amrCpatch(IM,JM,NG))
      AMRDBL W(NW,amrCpatch(IM,JM,NG))
      AMRINT EQN
      AMRDBL Win(NW)
      AMRDBL Sout(NW),Kscale
      DO I=1,IM
        DO J=1,JM
          DO EQN=1,NEQN
            Win(EQN) = W(EQN,I,J)
          END DO
          Kscale = 1.0 D0
          CALL CALCULATE_SOURCE(Win,Sout,DT,Kscale)
          DO EQN=1,NEQN
            S(EQN,I,J) = Sout(EQN)
          END DO
        END DO
      END DO
      RETURN
      END
*
*
*     CALCULATE_SOURCE:
*
*
      SUBROUTINE CALCULATE_SOURCE(WW,SS,DT,Kscale)
      AMRITA_TYPING
#include "$amrita:bcg::commonblk"
      AMRDBL  WW(NW)
      AMRDBL WWs(NW)
      AMRDBL  SS(NW)
      AMRDBL Kscale
      AMRINT EQN
      DO EQN=1,NEQN
        SS(EQN)  = 0.0 D0
        WWs(EQN) = WW(EQN)
      END DO
      P = (GMz-1.0 D0)*(WW(4)-0.5*(WW(2)*WW(2)+WW(3)*WW(3))/WW(1)\
            +WW(6)*Q)
      IF(P.GT.Pact) THEN
        DTs  = DT/Ns
        DO N=1,Ns
          f    = WW(5)/WW(1)
          y    = WW(6)/WW(1)
          T    = (GMz-1.0D0)*(WW(4)-0.5*(WW(2)*WW(2)+WW(3)*WW(3))\
```

```
                /WW(1)+WW(6)*Q)/WW(1)
            IF (f.LE.0.D0) THEN
*             Induction time over, only need update main heat release
              DyDt  = Ke*(1-MIN(y,1.D0))**(ETA)
              ys    = y+DyDt*0.5D0*DTs
              ys    = MIN(ys,1.D0)
              T     = (GMz-1.0 D0)*(WW(4)-0.5*(WW(2)*WW(2)+WW(3)*WW(3))\
                /WW(1)+WW(1)*ys*Q)/WW(1)
              DyDt  = Ke*(1-MIN(ys,1.D0))**(ETA)
              ys    = y+DyDt*DTs
              ys    = MIN(ys,1.D0)
              SS(6) = WW(1)*(ys-y)
              WW(6) = WW(6)+SS(6)
            ELSE
*             Induction time not over and main heat release not started:
              DfDt  = -Ki*EXP(-E/T)
              fs    = f+DfDt*DTs
              fs    = MAX(fs,0.D0)
              SS(5) = WW(1)*(fs-f)
              WW(5) = WW(5)+SS(5)
            ENDIF
          END DO
          DO N=1,NEQN
            SS(N) = WW(N)-WWs(N)
          END DO
        ENDIF
        RETURN
        END
  }
end proc
```

Startup.amr

```
proc Startup Iflux, Jflux
  CodeManifest addfile=$amrita::thisfile
  set amrita:bcg::startup =  INIT_REACTIVE_EULER_CODE
  fold::print {
    *
    *
    *    INIT_REACTIVE_EULER_CODE: GRAB REQUIRED CONSTANTS
    *
    *
       SUBROUTINE INIT_REACTIVE_EULER_CODE
       AMRITA_TYPING
  #include "$amrita:bcg::commonblk"
       AMRINT AMR::LOGFILE
       CALL LOG_BCG_ID
       CALL AMR::GET_CONST('amrita:EquationSet:expr::GAMMA',GMz)
       CALL AMR::GET_CONST('amrita:EquationSet:expr::Q',Q)
       CALL AMR::GET_CONST('amrita:EquationSet:expr::E',E)
       CALL AMR::GET_CONST('amrita:EquationSet:expr::Ki',Ki)
       CALL AMR::GET_CONST('amrita:EquationSet:expr::Ke',Ke)
```

```
      CALL AMR::GET_CONST('amrita:EquationSet:expr::ETA',ETA)
      PHI  = 1  /* parameter for limiter function  */
      NU   = 1  /* enforce slab symmetry           */
      Ns   = 1  /* sub-cycle source terms Ns times */
      Pact = 0.1 /* pressure switch for source terms */
      CALL AMR::GET_TOKEN('?AMRDBL:solver::PHI', PHI)
      CALL AMR::GET_TOKEN('?AMRDBL:solver::NU', NU)
      CALL AMR::GET_TOKEN('?AMRDBL:solver::Pact',Pact)
      CALL AMR::GET_TOKEN('?AMRINT:solver::Ns', Ns)
      WRITE(AMR::LOGFILE(),*) 'GAMMA  = ',GMz
      WRITE(AMR::LOGFILE(),*) 'Q      = ',Q
      WRITE(AMR::LOGFILE(),*) 'E      = ',E
      WRITE(AMR::LOGFILE(),*) 'Ki     = ',Ki
      WRITE(AMR::LOGFILE(),*) 'Ke     = ',Ke
      WRITE(AMR::LOGFILE(),*) 'ETA    = ',ETA
      WRITE(AMR::LOGFILE(),*) 'NU     = ',NU
      WRITE(AMR::LOGFILE(),*) 'PHI    = ',PHI
      WRITE(AMR::LOGFILE(),*) 'Pact   = ',Pact
      WRITE(AMR::LOGFILE(),*) 'Ns     = ',Ns
      CALL FLUSH(AMR::LOGFILE())
      RETURN
      END
  }
end proc
```

Appendix D

Resonating Mechanisms of the Very High Frequency Pulsations

For the very high frequency pulsations described in Section 4.4, it was seen that Toong's mechanism overlapped with the very high frequency mechanism. A rough sketch of the overlap of the two mechanisms is illustrated on a x-t diagram in *Figure D.1*. As seen in *Figure D.1*, this resonating behaviour occurs when the transit time of a particle path across the induction zone is equal to the sum of the transit times of two C- characteristics and a C+ characteristic across the induction time. The following details the conditions required for resonation to occur.

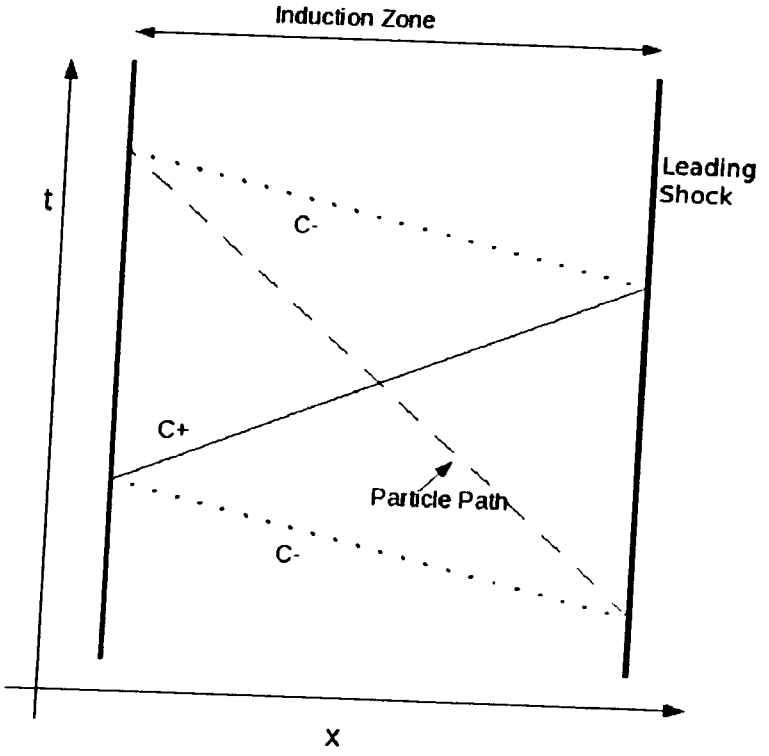

Figure D1 - Rough sketch of two mechanisms working in resonation. Particle path and C- arrive at the end of the induction zone at the same time.

Let t_-, t_+ and t_0 be the non-dimensional transit times for the C-, C+ and particle paths respectively to travel the length of the induction zone. The above three transit times in non-dimensional parameters (keeping in mind that the non-dimensional length of the induction zone is 1, and that the state across the induction zone is the same as the post-shock state) can be expressed as:

$$t_-=\left|\frac{1}{u_s-c_s}\right| \tag{D.1}$$

$$t_+=\left|\frac{1}{u_s+c_s}\right| \tag{D.2}$$

$$t_0=\left|\frac{1}{u_s}\right| \tag{D.3}$$

Since u_s is negative, and the flow is subsonic across the induction zone (and hence c_s is larger than u_s), (D.1)-(D.3) can be rewritten:

$$t_-=\frac{-1}{u_s-c_s} \tag{D.4}$$

$$t_+=\frac{1}{u_s+c_s} \tag{D.5}$$

$$t_0=\frac{-1}{u_s} \tag{D.6}$$

The condition for resonance to occur is:

$$2t_-+t_+=t_0 \tag{D.7}$$

Substituting (D.4)-(D.6) into (D.7), we get:

$$\frac{-2}{u_s-c_s}+\frac{1}{u_s+c_s}=\frac{-1}{u_s} \tag{D.8}$$

The left hand side simplifies to:

$$\frac{-2(u_s+c_s)+(u_s-c_s)}{(u_s-c_s)(u_s+c_s)}=\frac{-u_s-3c_s}{(u_s-c_s)(u_s+c_s)} \tag{D.9}$$

which gives:

$$\frac{-u_s-3c_s}{(u_s-c_s)(u_s+c_s)}=\frac{-1}{u_s}$$

$$(u_s+3c_s)u_s=1(u_s-c_s)(u_s+c_s)$$

$$u_s^2+3u_s c_s=u_s^2-c_s^2$$

$$\frac{-u_s}{c_s}=\frac{1}{3} \tag{D.10}$$

According to (D.10), resonance occurs when the local Mach number of the induction zone is 1/3.

For $\bar{Q}=50, \gamma=1.2$, (A.4) and (A.5) give:

$$M_{CJ}=\frac{D_{CJ}}{c_o}=6.21617, Q=10.3875$$

corresponding to the parameters of the results in Section 4.4. Knowing M_{CJ}, the local Mach number of the induction zone can be calculated:

$$\frac{u_s}{c_s}=\frac{u_s}{u_o}\frac{u_o}{c_o}\frac{c_o}{c_s} \tag{D.11}$$

Since the values of u were calculated in the reference frame of the leading shock, u_o is the detonation velocity, D_{CJ}, and u_o/c_o is simply M_{CJ}. u_s/u_o can be calculated knowing M_{CJ} using the Rankine Hugoniot jump condition, (2.17). The ratio, c_o/c_s can also be obtained from the Rankine Hugoniot jump relation (Liepmann and Roshko 1957):

$$\frac{c_o}{c_s}=\left(1+\frac{2(\gamma-1)}{(\gamma+1)^2}\frac{\gamma M_{CJ}^2+1}{M_{CJ}^2}(M_{CJ}^2-1)\right)^{-1/2} \tag{D.12}$$

According to (D.11), the local Mach number of the induction zone in the very high frequency results of Section 4.4 is u_s/c_s = 0.3242, very closely approximating the condition for resonance, given by (D.10).

Appendix E

Calculation of the Thermicity

The calculation of the thermicity discussed in Section 4.1 is detailed here. The thermicity is used to calculate the reaction length, and thus the stability parameter, χ. Here, we use Ng et. al's (2005) definition of the reaction zone length:

$$\Delta_e = \frac{u_{CJ}}{\dot{\sigma}_{max}} \tag{E.1}$$

where $\dot{\sigma}$ is the thermicity, defined as:

$$\dot{\sigma} = \frac{(\gamma-1)}{\gamma}\frac{\tilde{Q}}{RT_o}\frac{D\lambda_e}{Dt} \tag{E.2}$$

The maximum thermicity, $\dot{\sigma}_{max}$ is:

$$\dot{\sigma}_{max} = \frac{(\gamma-1)}{\gamma}\frac{\tilde{Q}}{RT_o}\left(\frac{D\lambda_e}{Dt}\right)_{max} \tag{E.3}$$

$\left(\frac{D\lambda_e}{Dt}\right)_{max}$ can be found by inspecting equation (2.8). Since λ_i and λ_e range from 0 to 1, this occurs when $\lambda_i = 0$ and $\lambda_e = 0$, where $(1 - H(\lambda_i)) = 1$ and $(1 - \lambda_e)^\nu = 1$.

$$\frac{D\lambda_e}{D\tilde{t}} = (1-H(\lambda_i))K_e(1-\lambda_e)^\nu$$

$$\left(\frac{D\lambda_e}{D\tilde{t}}\right)_{max} = K_e \tag{E.4}$$

(E.1) then reduces to:

$$\Delta_e = \frac{\gamma u_{CJ}}{(\gamma-1)(\tilde{Q}/RT_o)K_e} \tag{E.5}$$

In Section 4, $\gamma = 1.2$, and Q = 2.789, 5.000, 7.500, and 10.3875. *Table E1* gives the parameters required to compute (E.5) for each value of Q.

Table E1 - Parameters required to compute (E.5) at each Q

Q	2.789	5.000	7.500	10.3875
$\tilde{Q}/RT_o$	4	9.119	19.314	50
u_{CJ}	0.7121	0.9534	1.1678	1.3743

Appendix F

Shock Pressure Histories at the Stability Boundary

In Chapter 4, a parametric study was performed to obtain the stability boundary for a wide range of parameters. The following contains the shock pressure histories at the stability boundary for the 16 sets of parameters investigated.

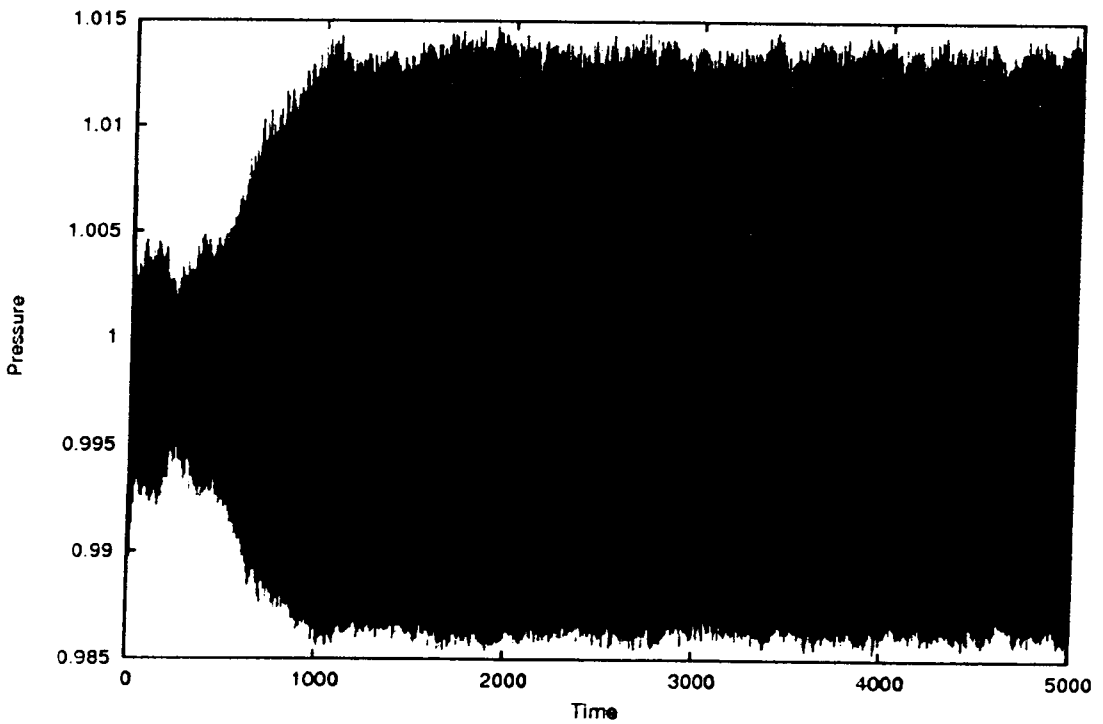

Figure F.1a - Shock pressure history for Q = 2.789, E = 1, K_e = 15.94

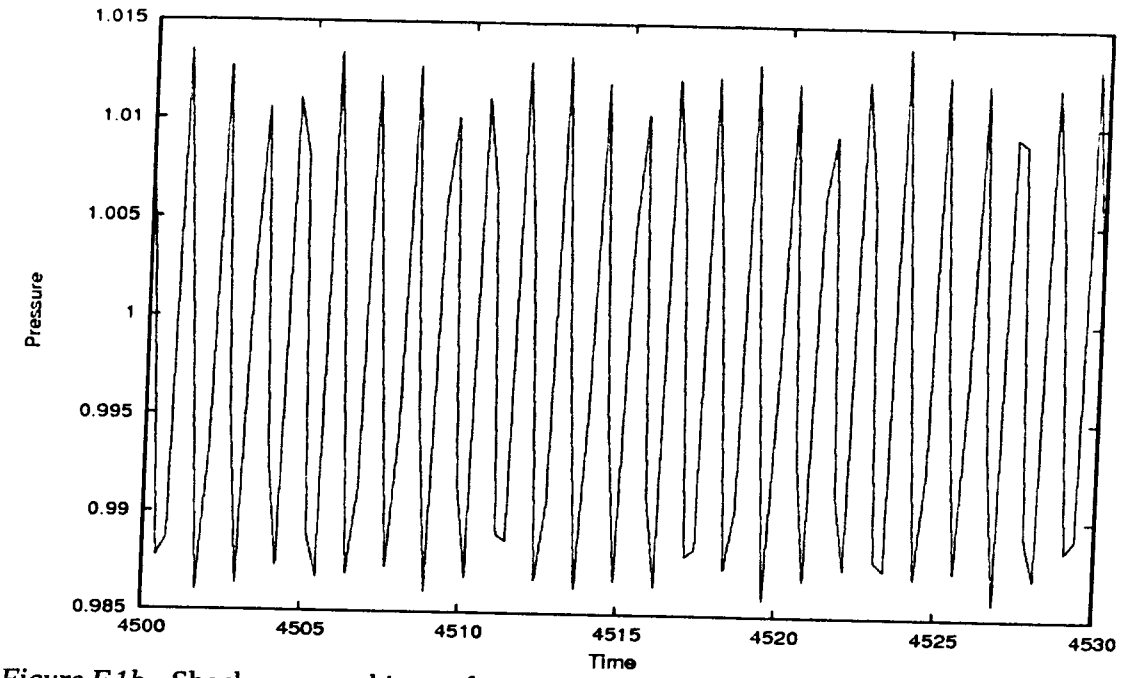

Figure F.1b - Shock pressure history for Q = 2.789, E = 1, K_e = 15.94

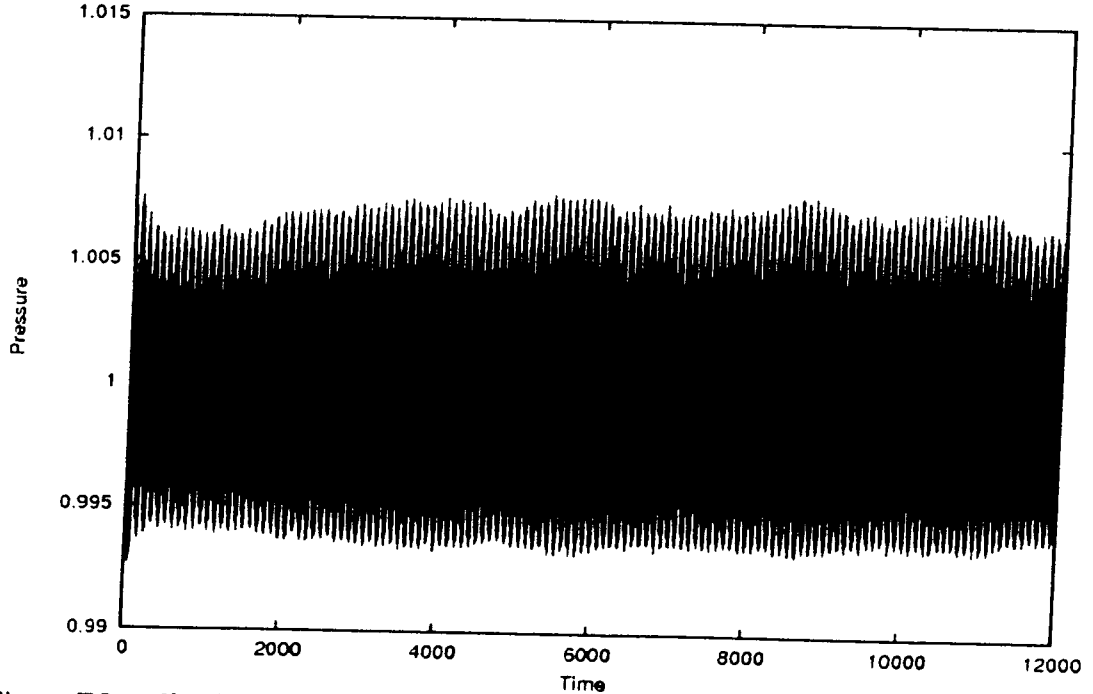

Figure F.2a - Shock pressure history for Q = 2.789, E = 5, K_e = 2.68

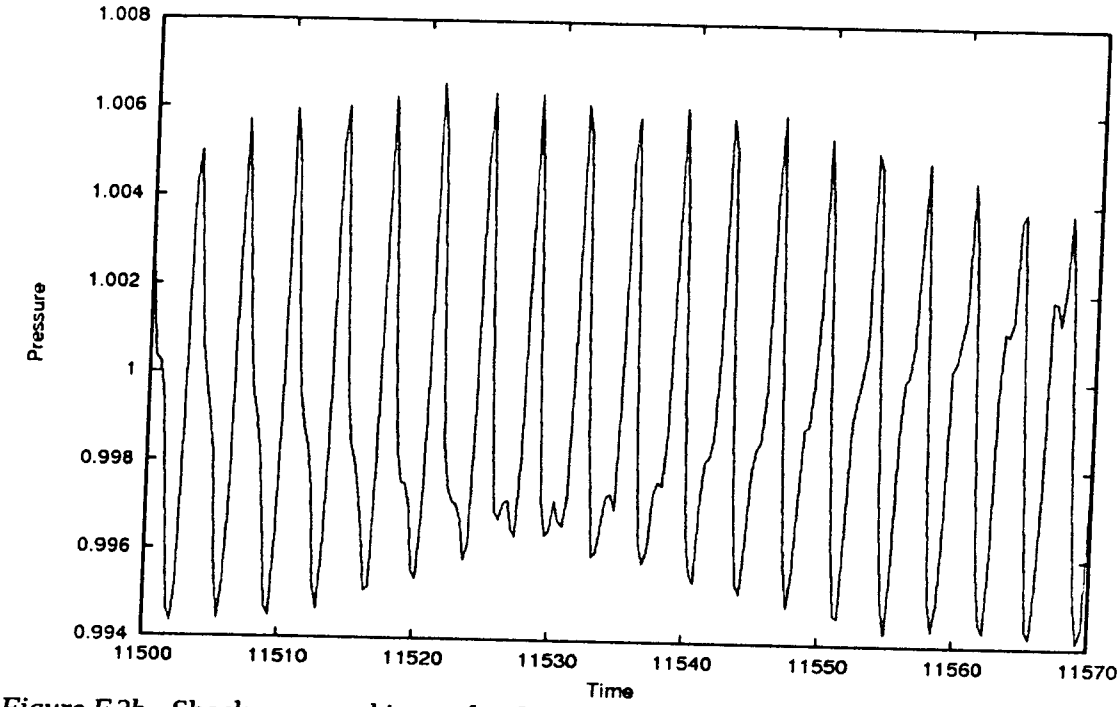

Figure F.2b - Shock pressure history for Q = 2.789, E = 5, K_e = 2.68

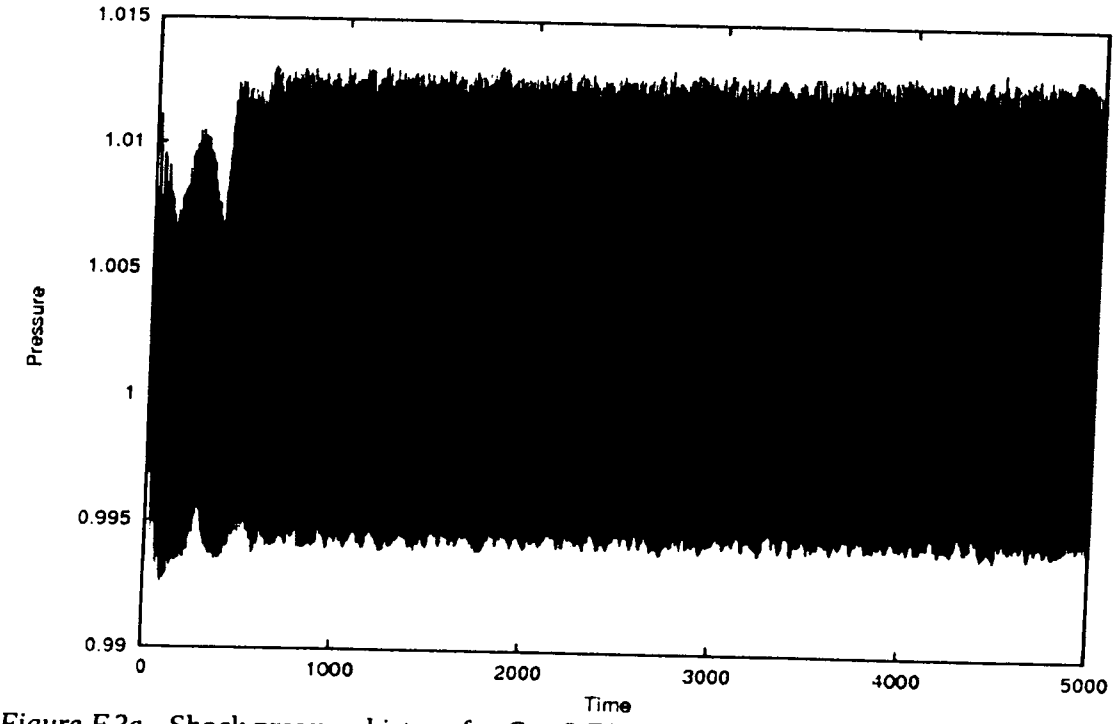

Figure F.3a - Shock pressure history for Q = 2.789, E = 7.5, K_e = 1.81

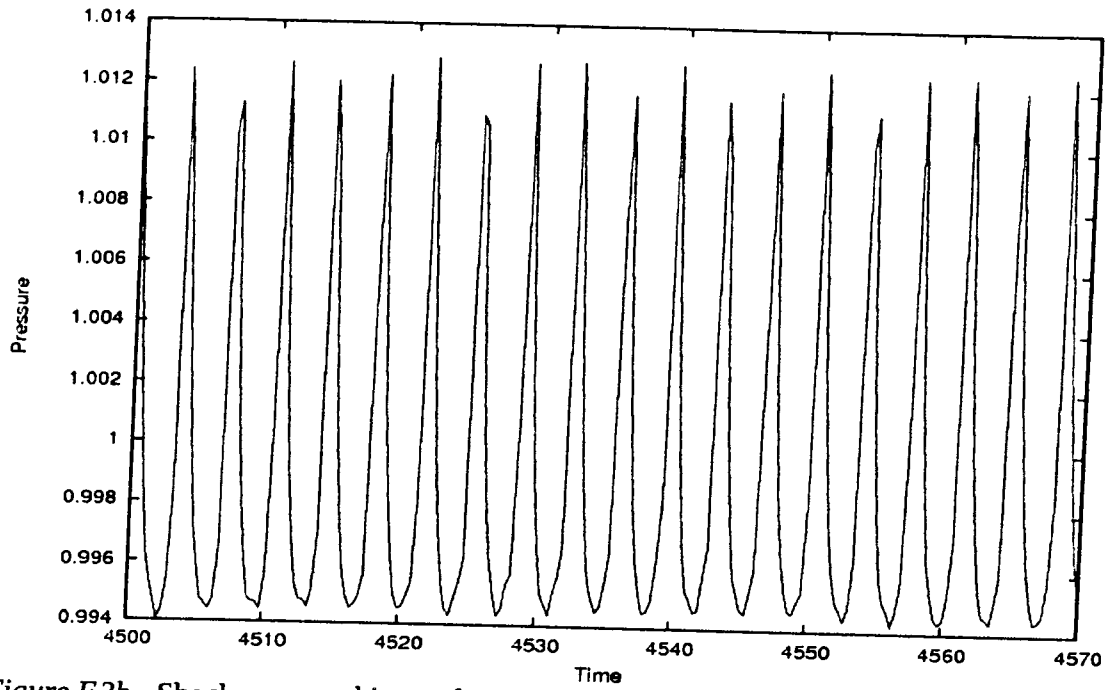

Figure F.3b - Shock pressure history for $Q = 2.789$, $E = 7.5$, $K_e = 1.81$

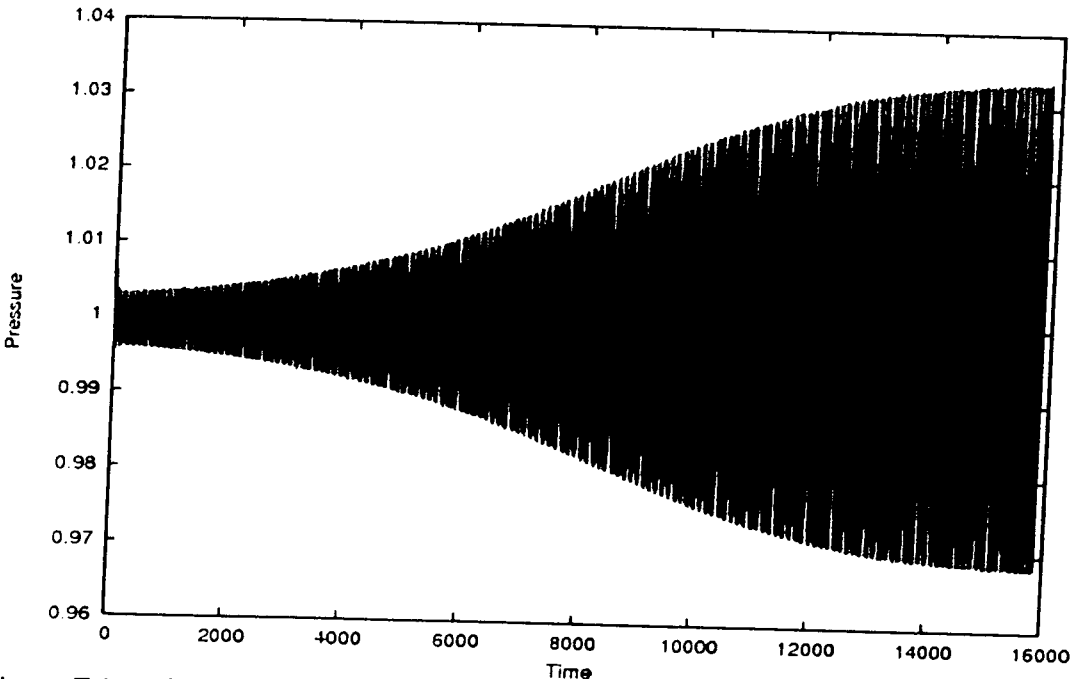

Figure F.4a - Shock pressure history for $Q = 2.789$, $E = 10$, $K_e = 1.18$

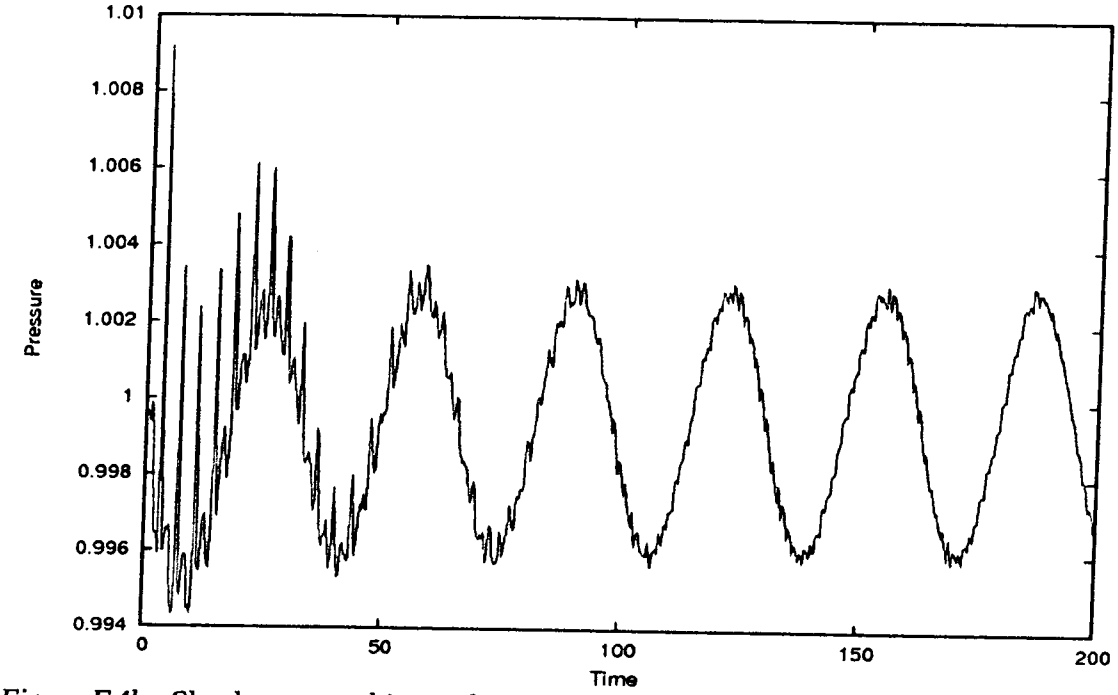

Figure F.4b - Shock pressure history for Q = 2.789, E = 10, K_e = 1.18

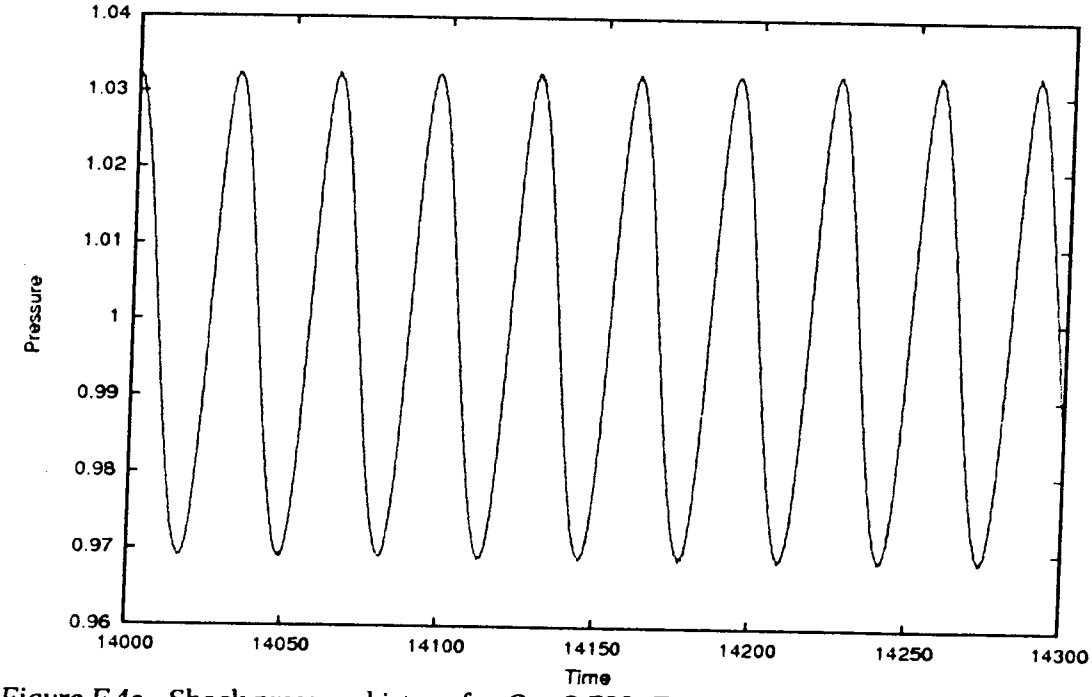

Figure F.4c - Shock pressure history for Q = 2.789, E = 10, K_e = 1.18

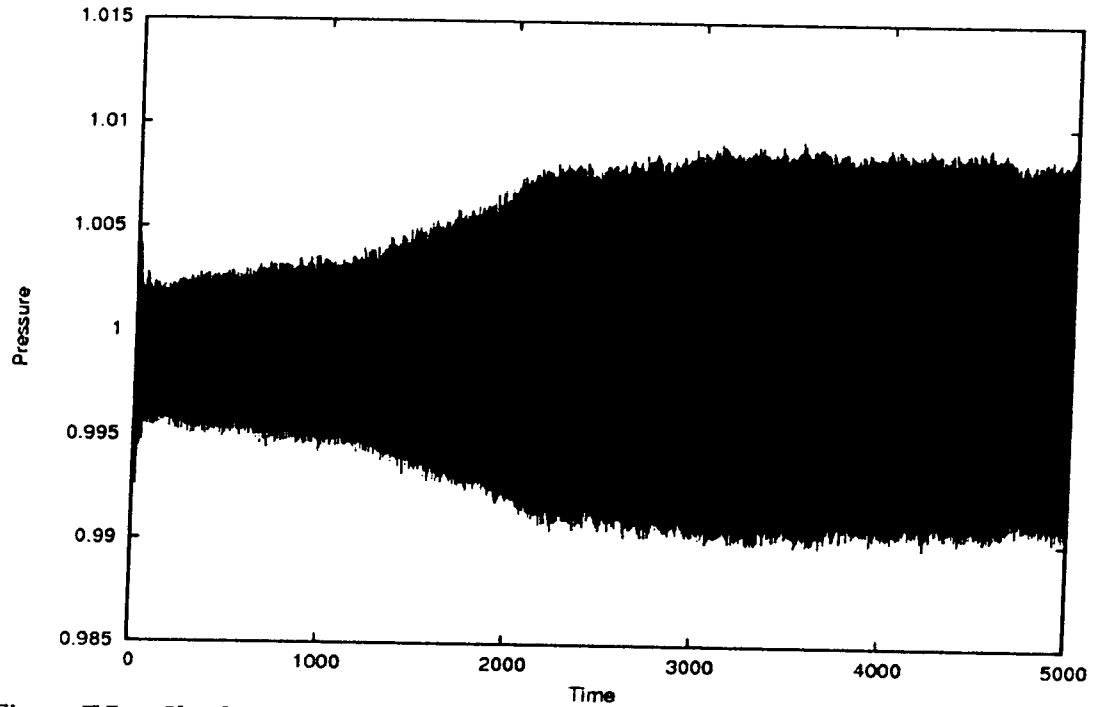

Figure F.5a - Shock pressure history for Q = 5.000, E = 1, K_e = 5.66

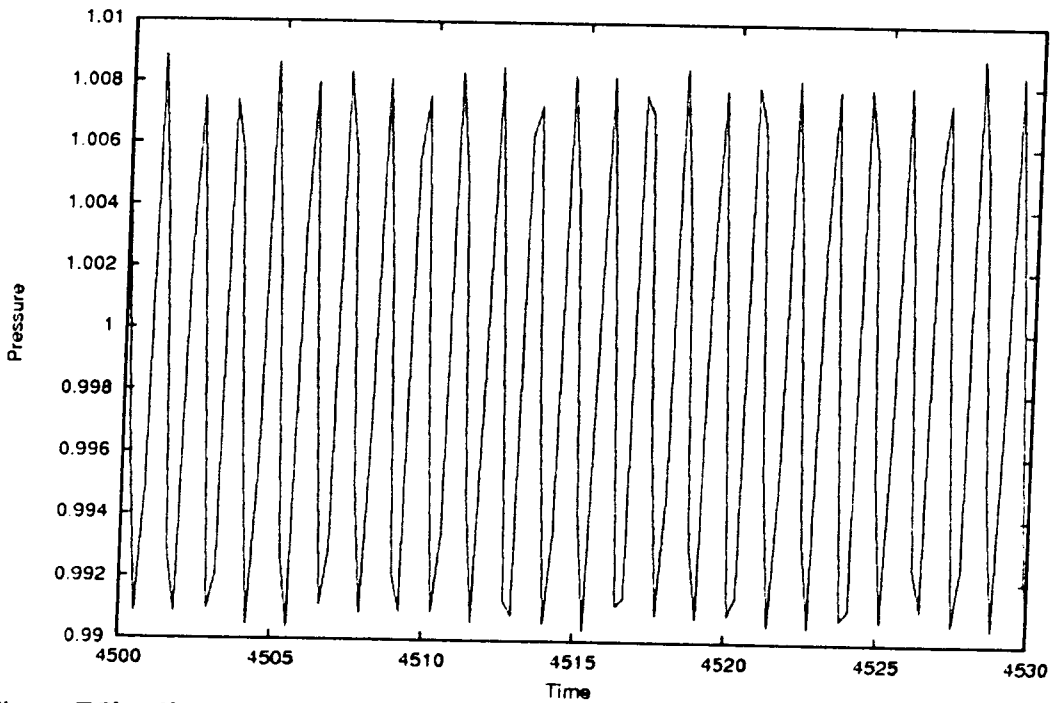

Figure F.5b - Shock pressure history for Q = 5.000, E = 1, K_e = 5.66

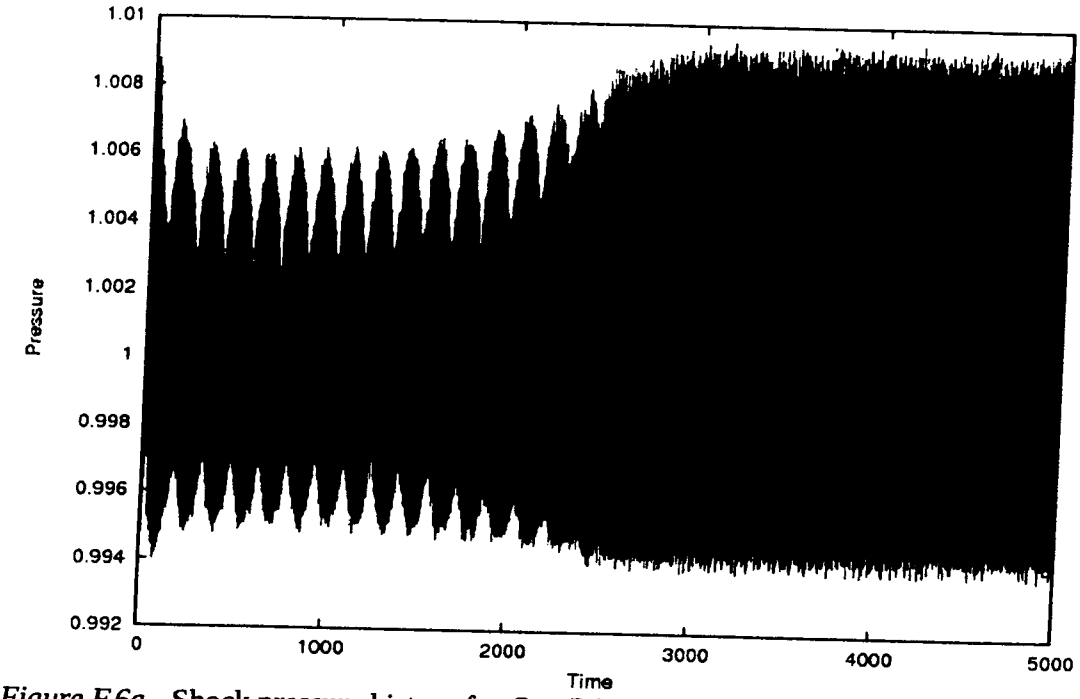

Figure F.6a - Shock pressure history for Q = 5.000, E = 5, K_e = 1.04

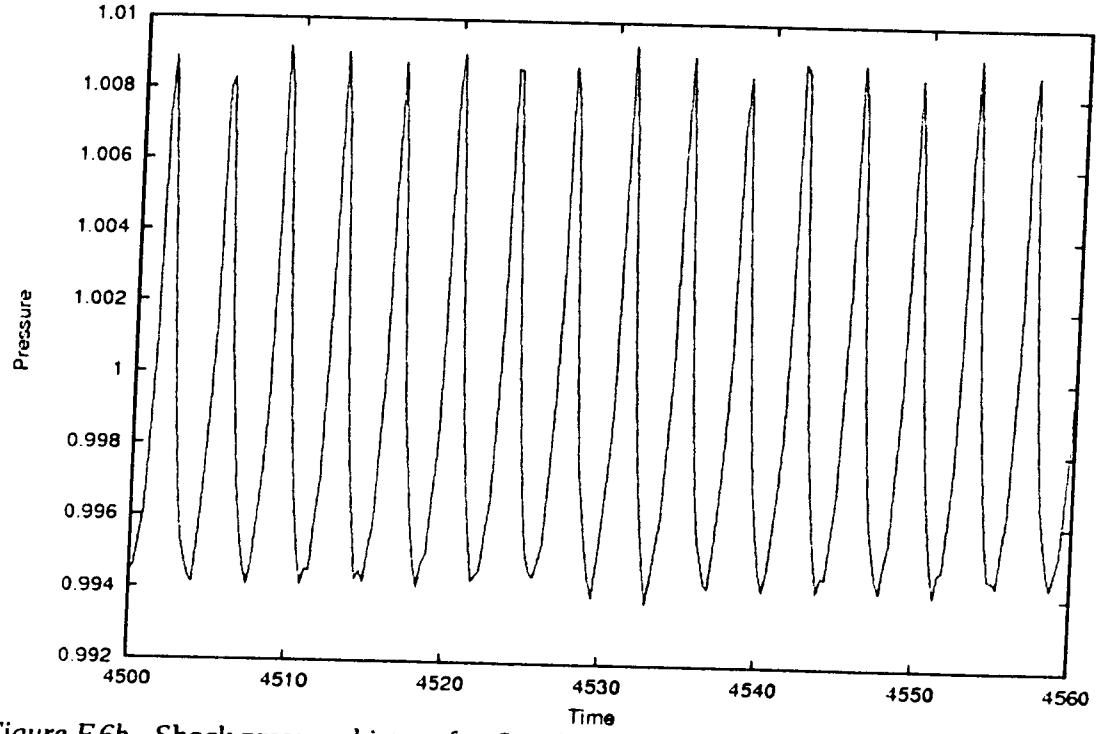

Figure F.6b - Shock pressure history for Q = 5.000, E = 5, K_e = 1.04

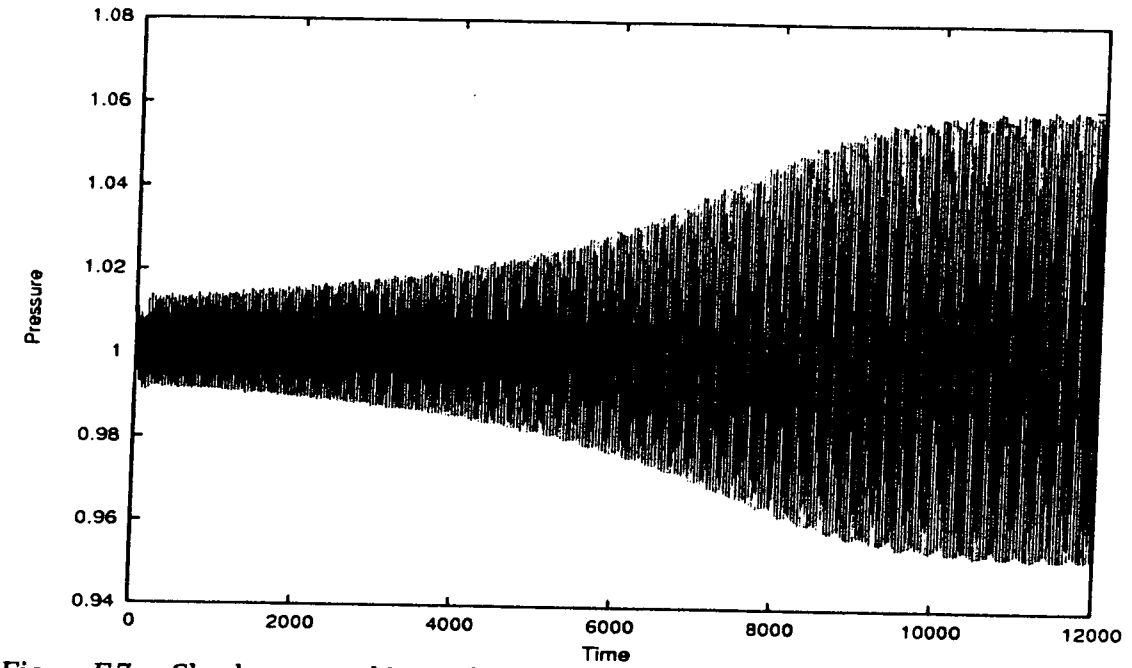

Figure F.7a - Shock pressure history for Q = 5.000, E = 7.5, K_e = 0.70

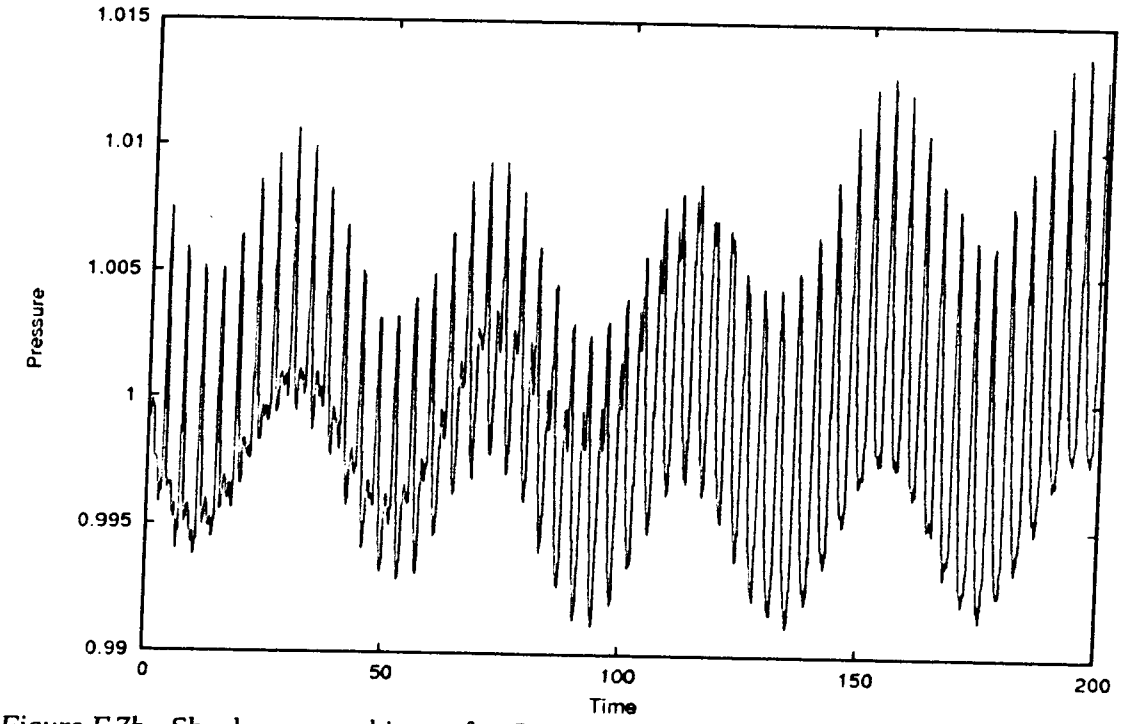

Figure F.7b - Shock pressure history for Q = 5.000, E = 7.5, K_e = 0.70

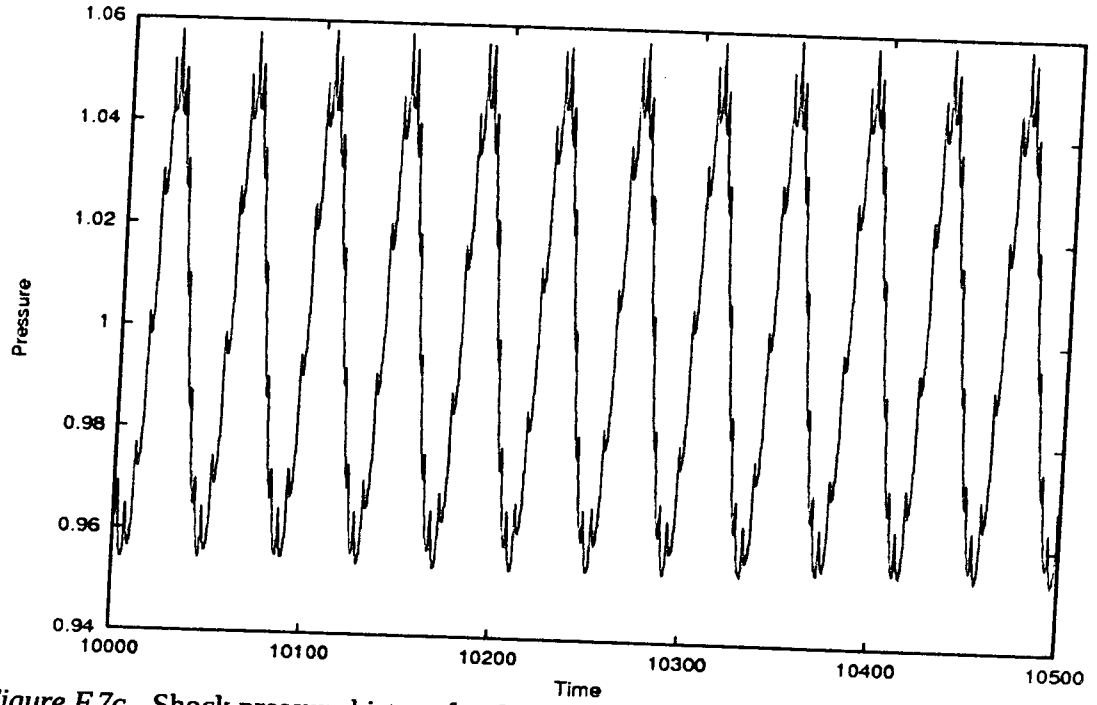

Figure F.7c - Shock pressure history for Q = 5.000, E = 7.5, K_e = 0.70

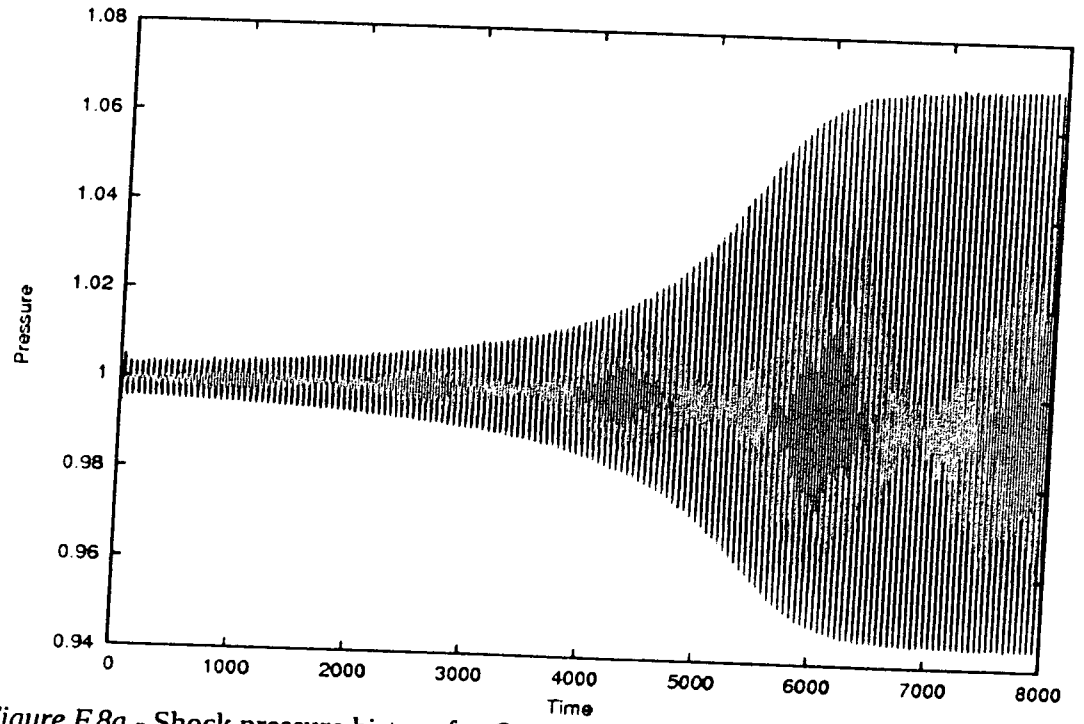

Figure F.8a - Shock pressure history for Q = 5.000, E = 10, K_e = 0.45

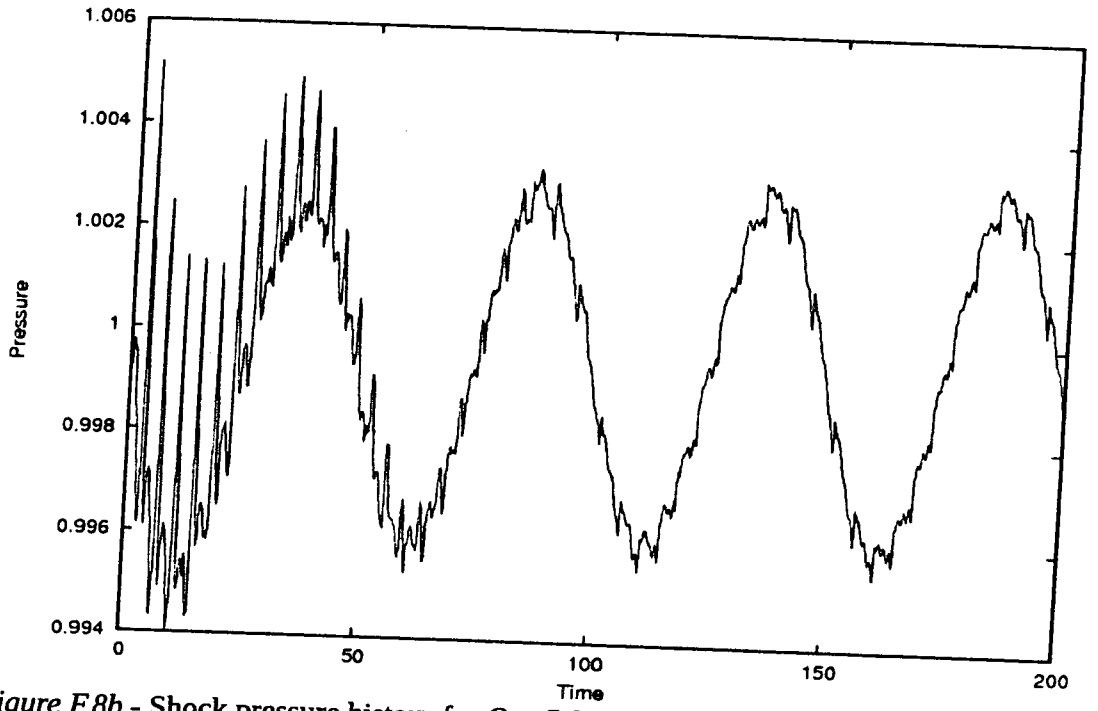

Figure F.8b - Shock pressure history for $Q = 5.000$, $E = 10$, $K_e = 0.45$

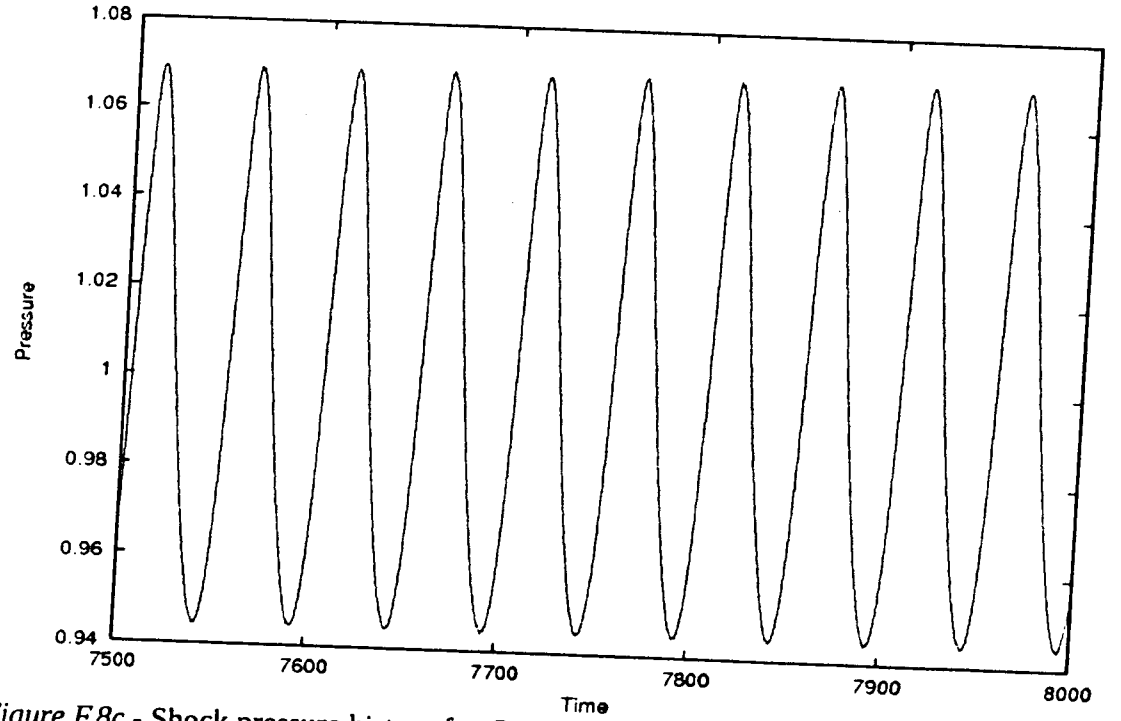

Figure F.8c - Shock pressure history for $Q = 5.000$, $E = 10$, $K_e = 0.45$

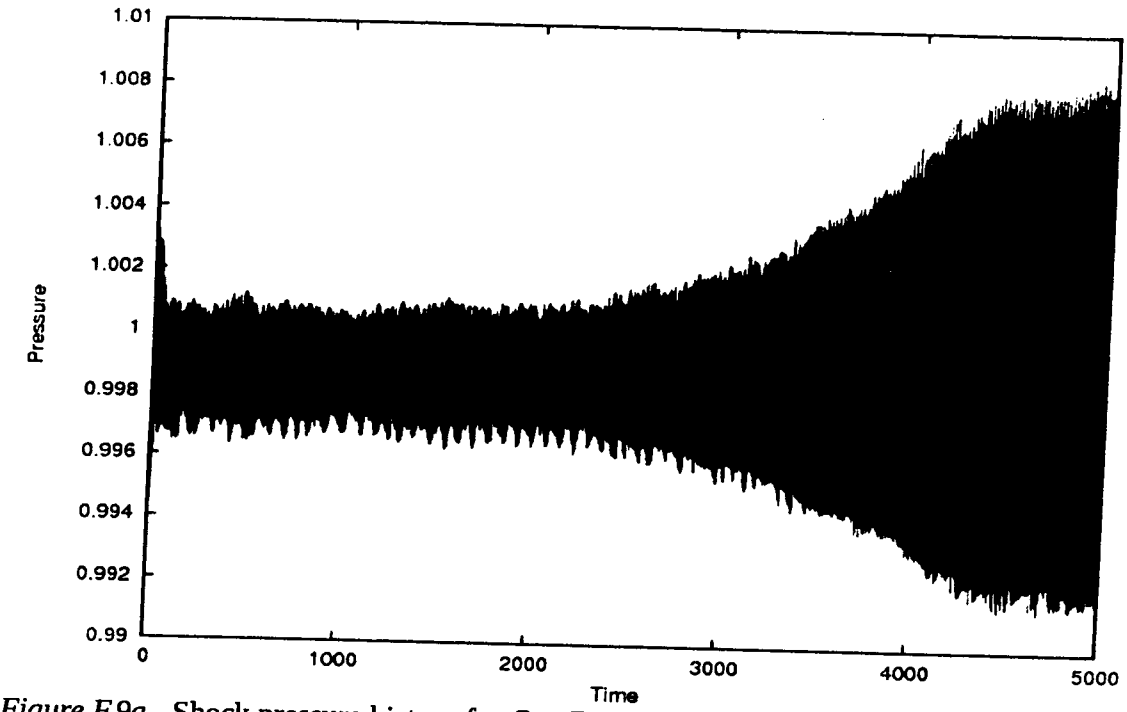

Figure F.9a - Shock pressure history for $Q = 7.500$, $E = 1$, $K_e = 2.89$

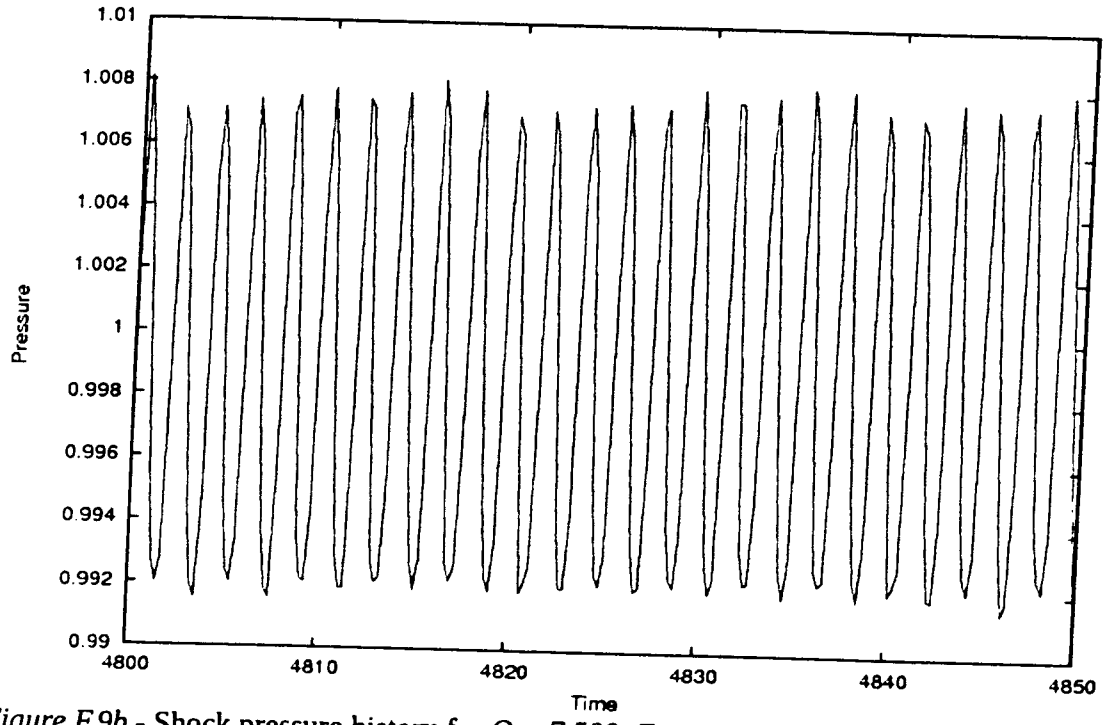

Figure F.9b - Shock pressure history for $Q = 7.500$, $E = 1$, $K_e = 2.89$

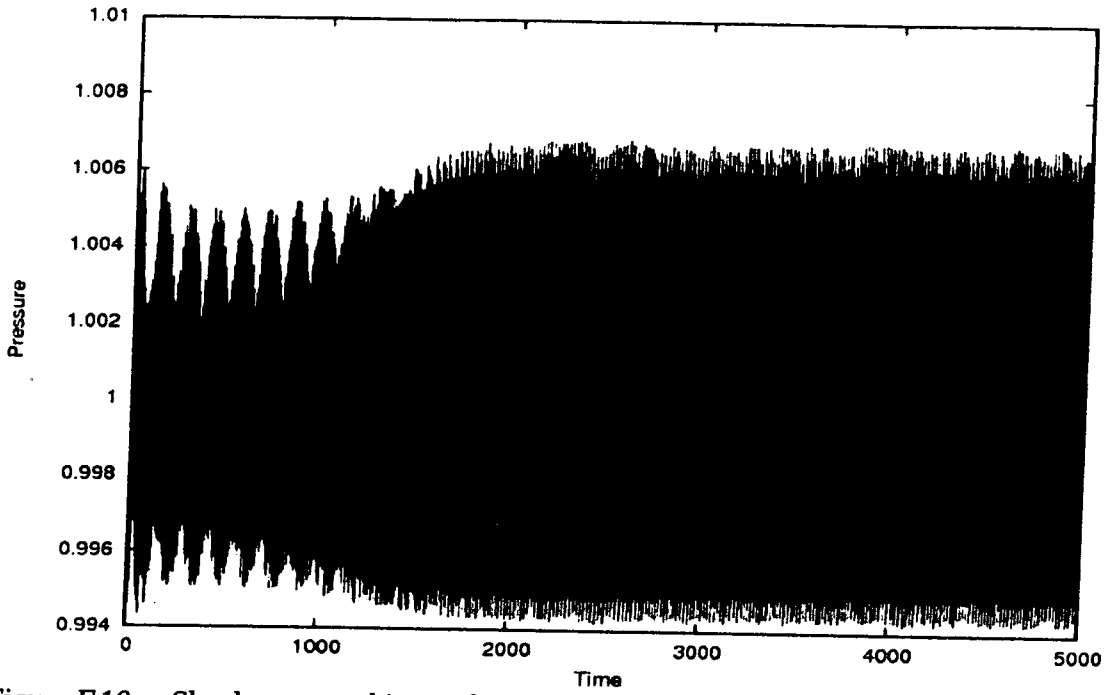

Figure F.10a - Shock pressure history for Q = 7.500, E = 5, K_e = 0.54

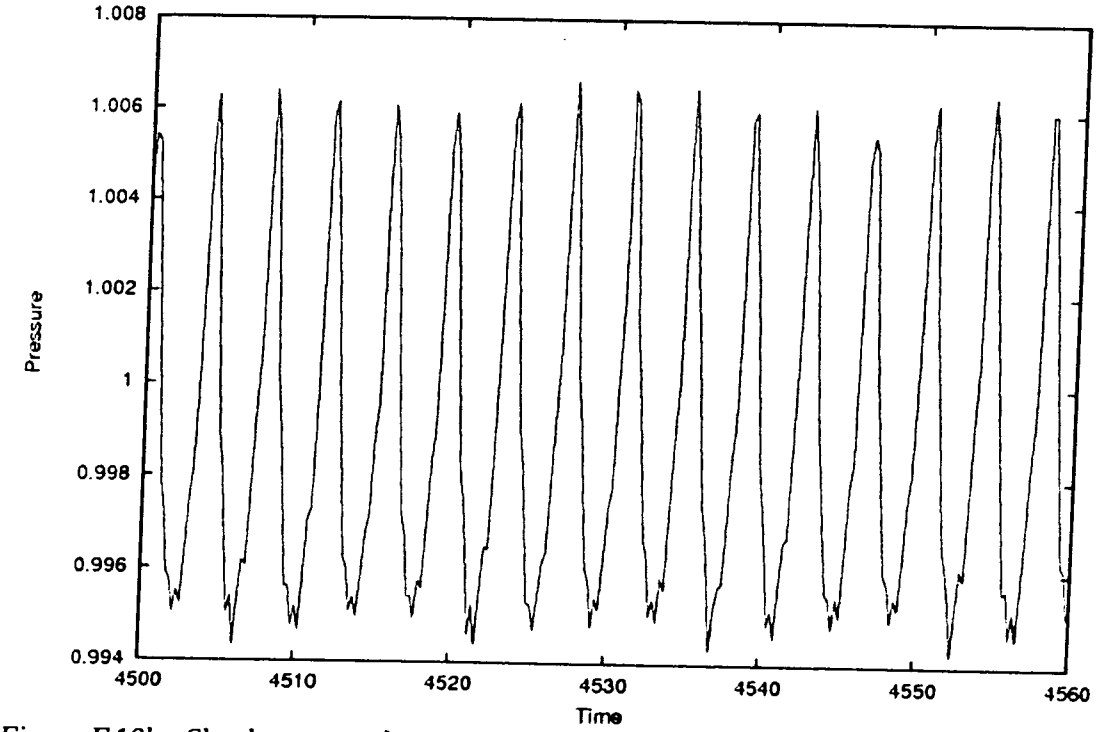

Figure F.10b - Shock pressure history for Q = 7.500, E = 5, K_e = 0.54

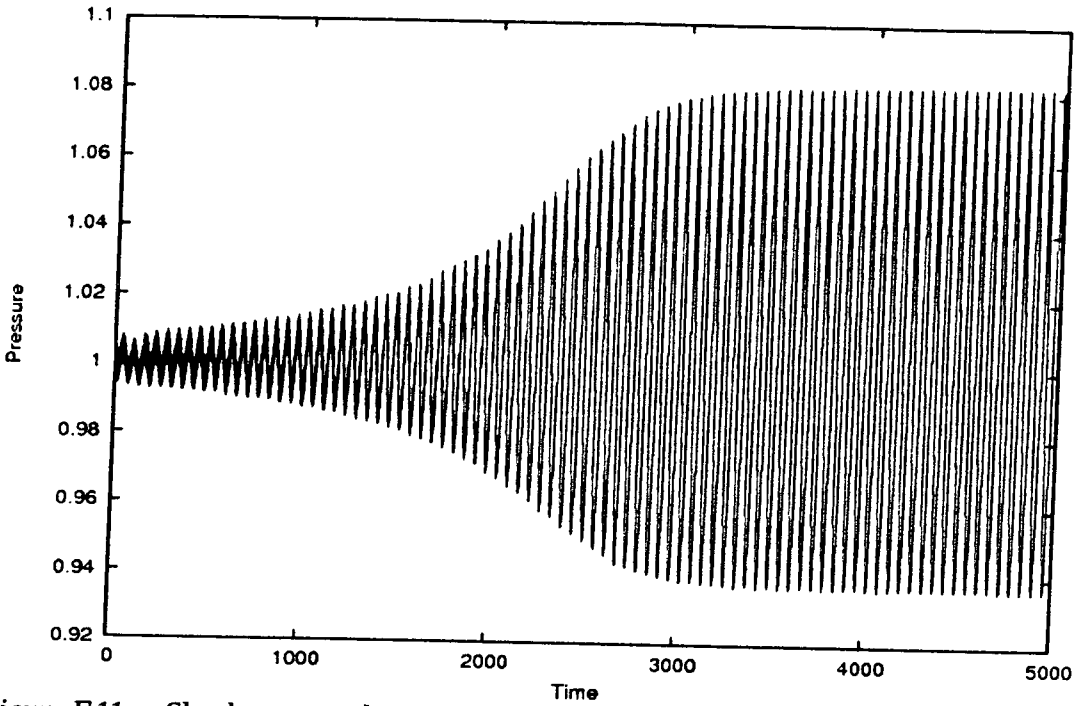

Figure F.11a - Shock pressure history for Q = 7.500, E = 7.5, K_e = 0.35

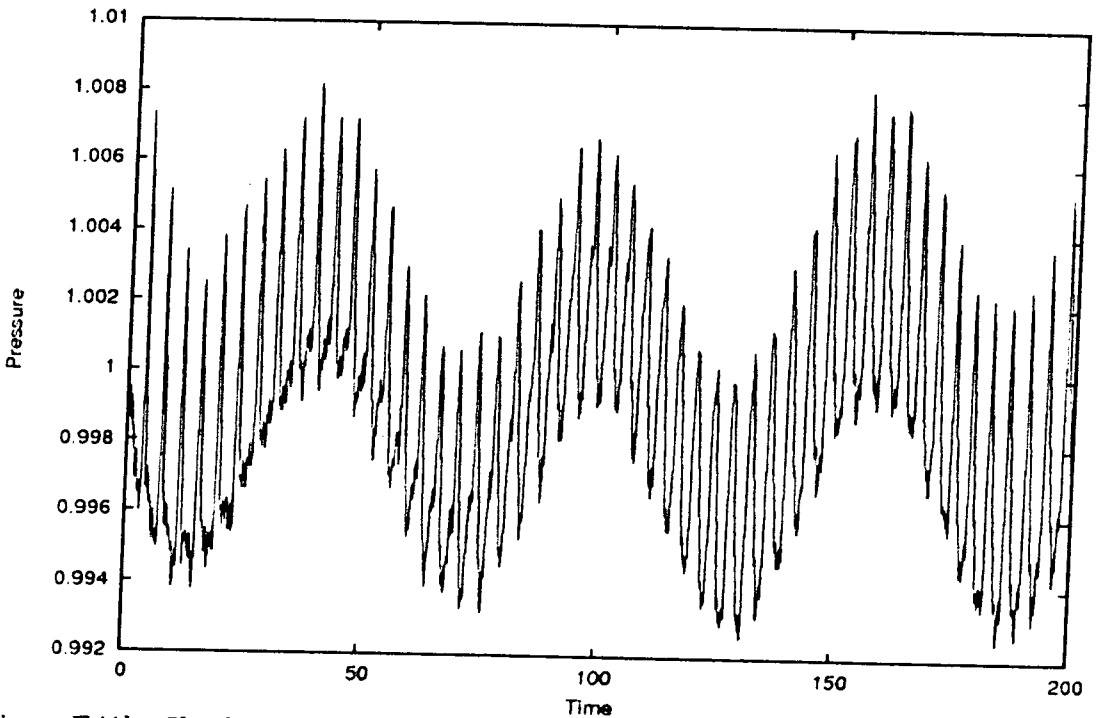

Figure F.11b - Shock pressure history for Q = 7.500, E = 7.5, K_e = 0.35

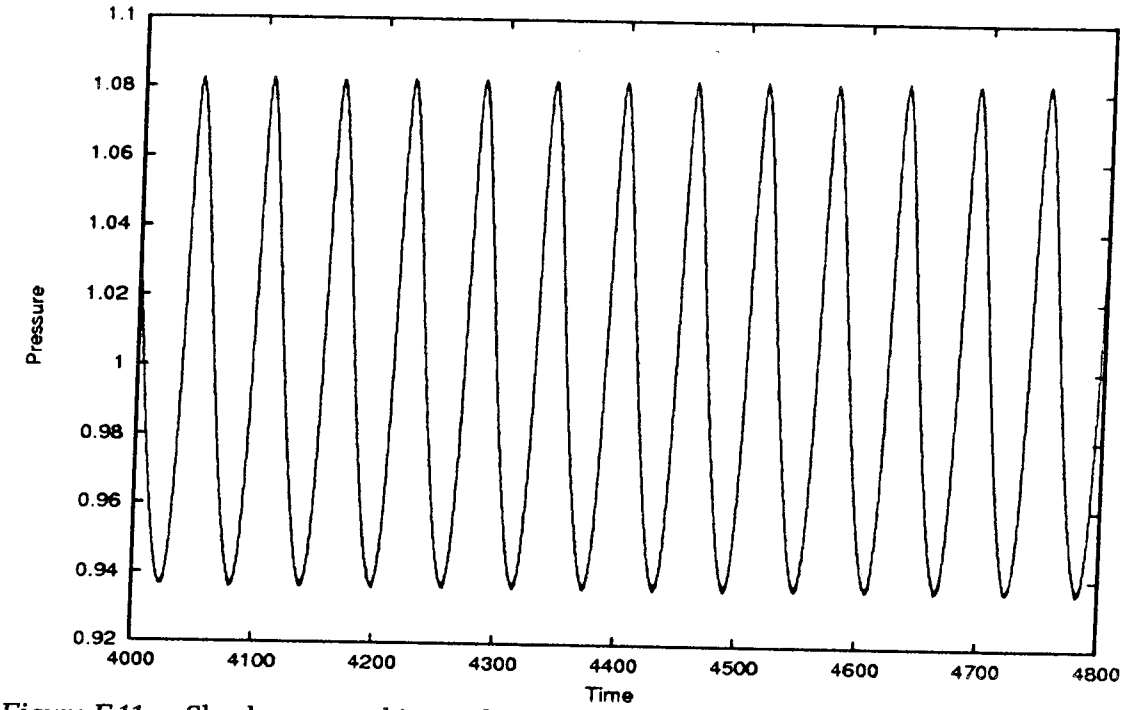

Figure F.11c - Shock pressure history for $Q = 7.500$, $E = 7.5$, $K_e = 0.35$

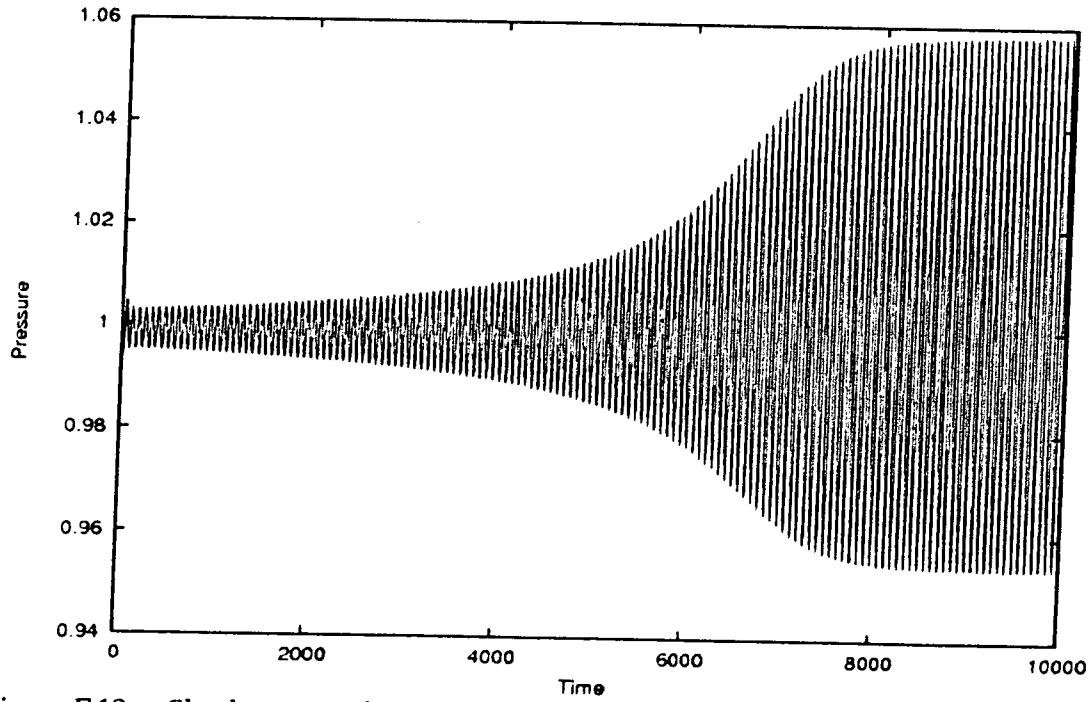

Figure F.12a - Shock pressure history for $Q = 7.500$, $E = 10$, $K_e = 0.24$

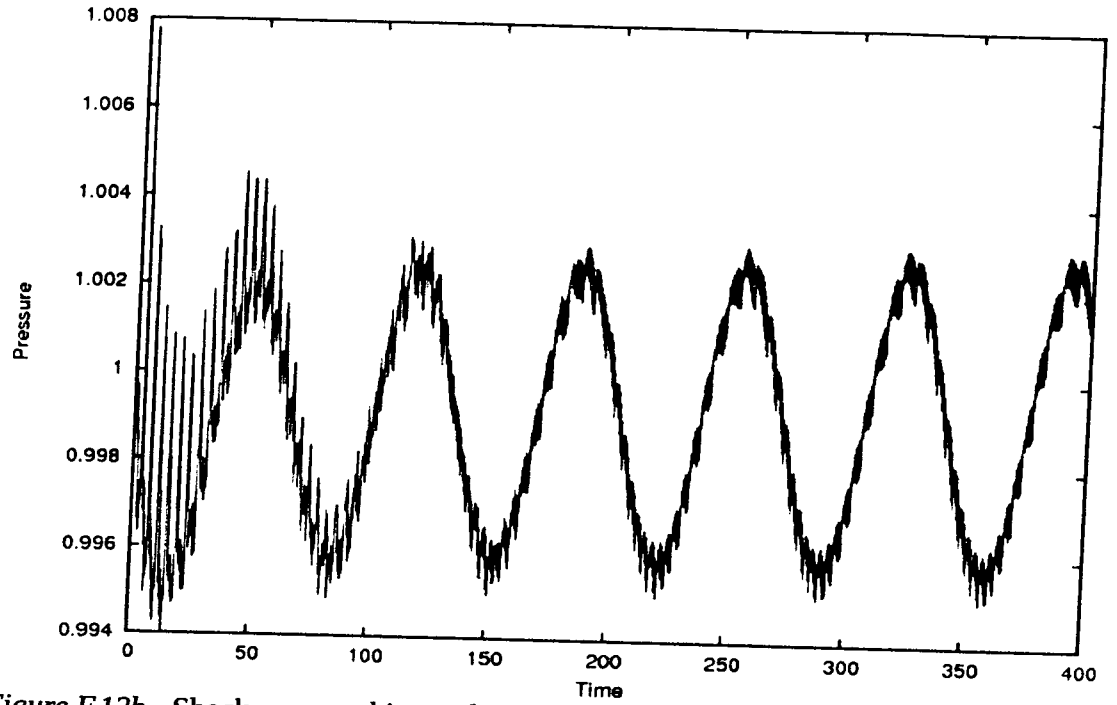

Figure F.12b - Shock pressure history for Q = 7.500, E = 10, K_e = 0.24

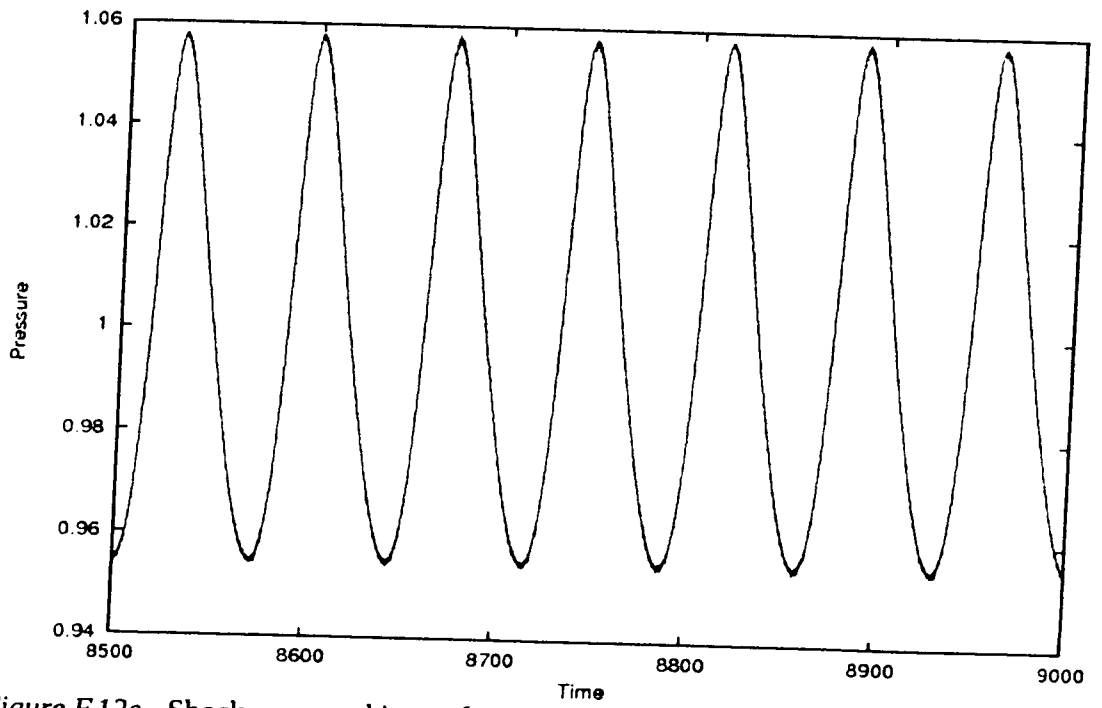

Figure F.12c - Shock pressure history for Q = 7.500, E = 10, K_e = 0.24

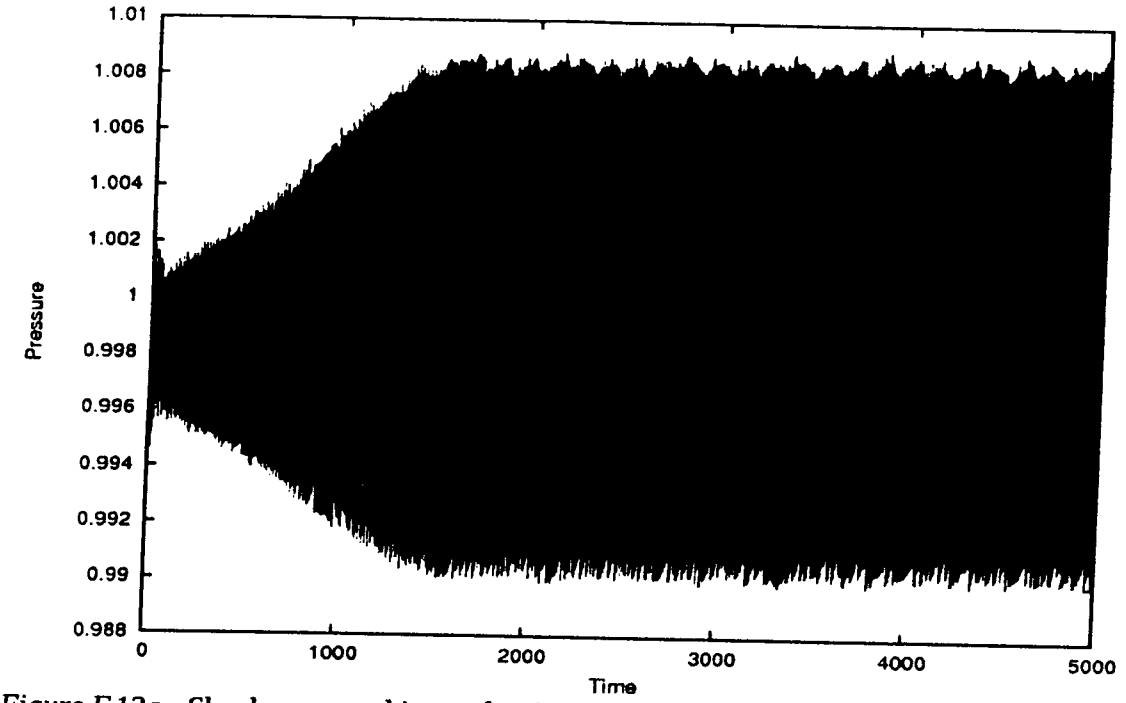

Figure F.13a - Shock pressure history for Q = 10.3875, E = 1, K_e = 1.66

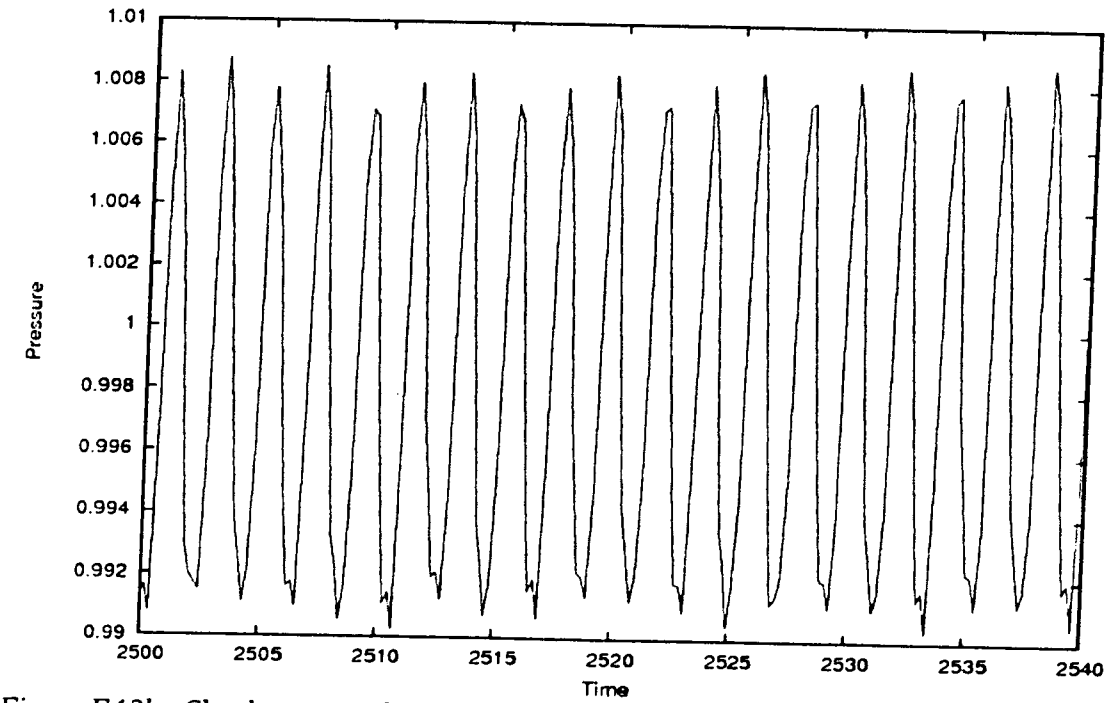

Figure F.13b - Shock pressure history for Q = 10.3875, E = 1, K_e = 1.66

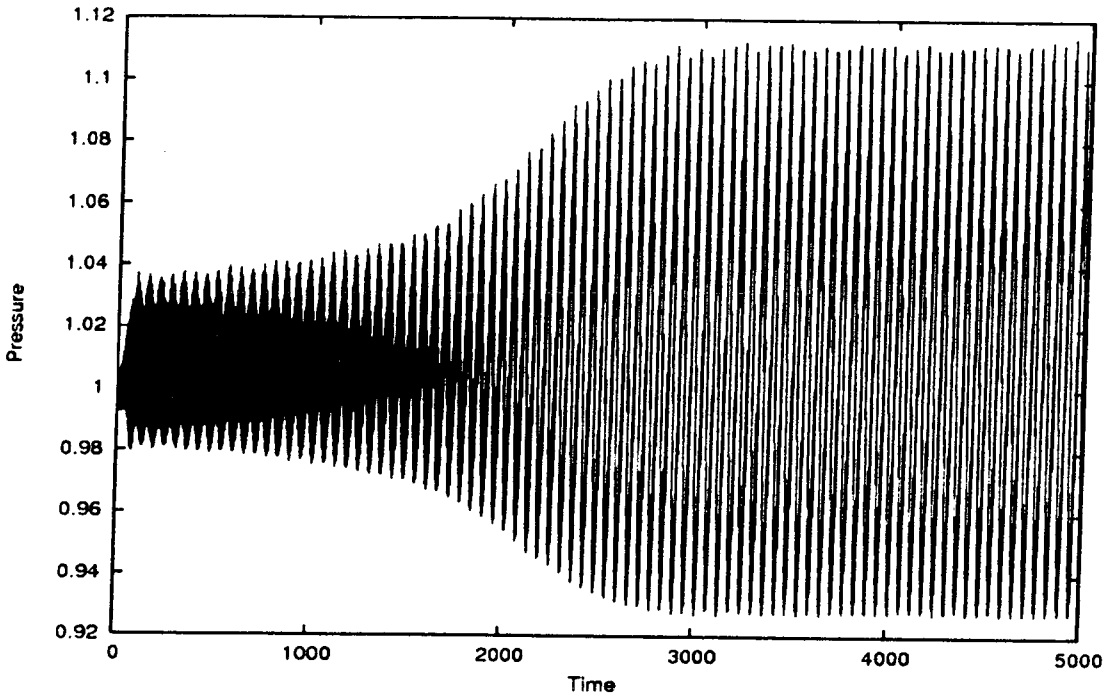

Figure F.14a - Shock pressure history for Q = 10.3875, E = 5, K_e = 0.37

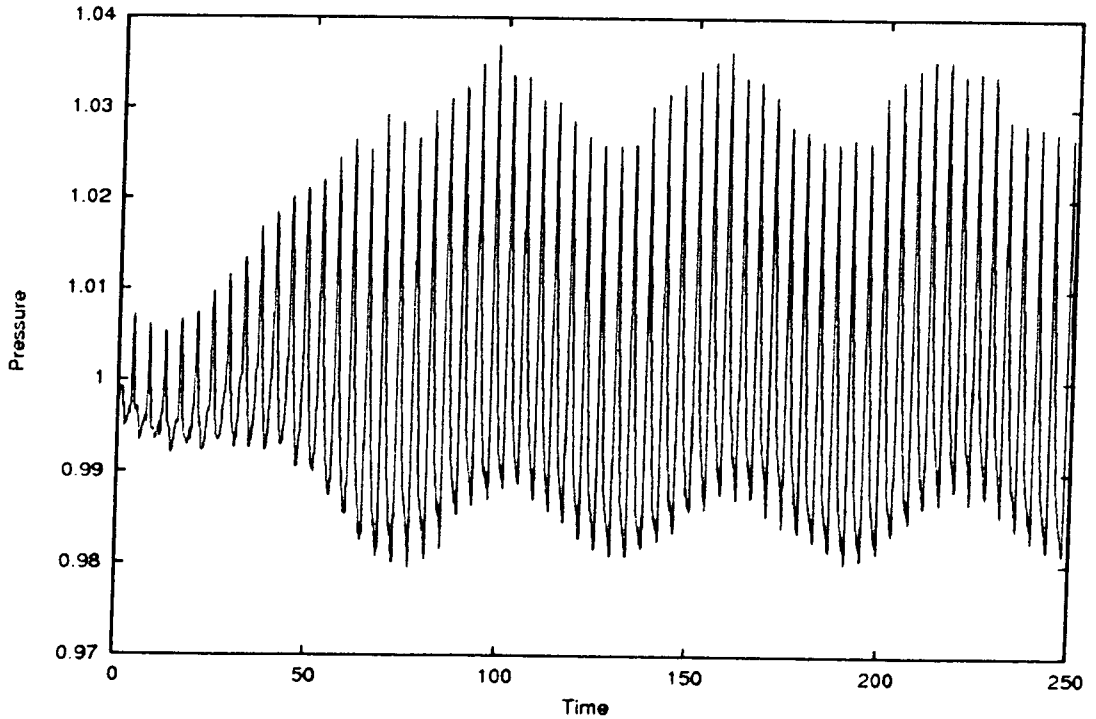

Figure F.14b - Shock pressure history for Q = 10.3875, E = 5, K_e = 0.37

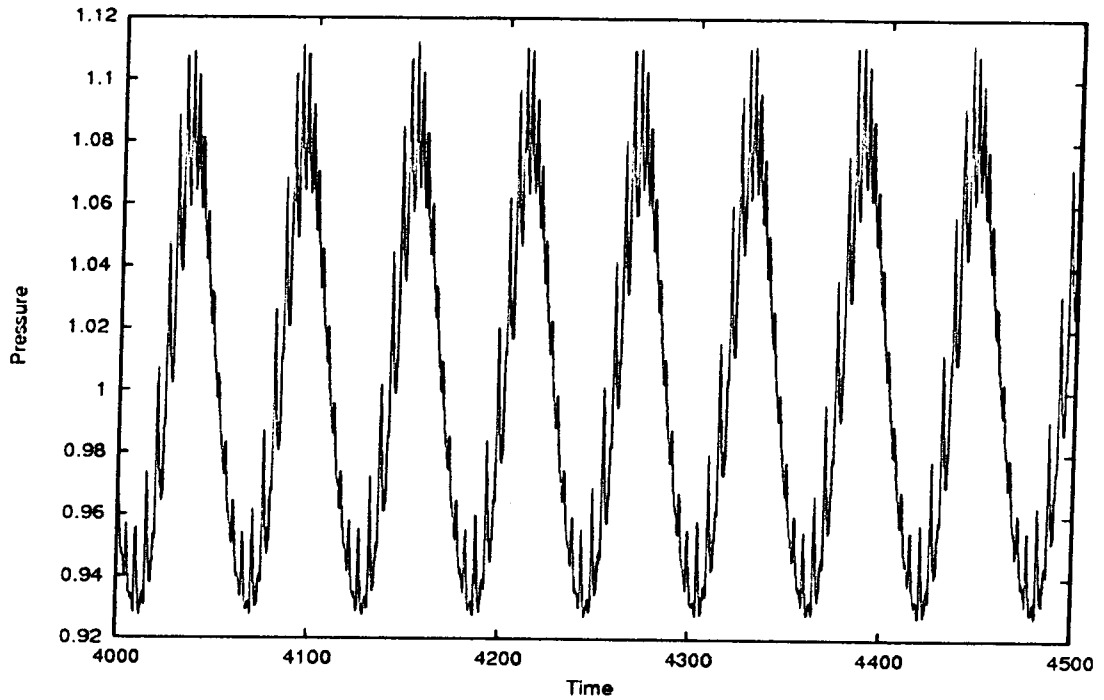

Figure F.14c - Shock pressure history for Q = 10.3875, E = 5, K_e = 0.37

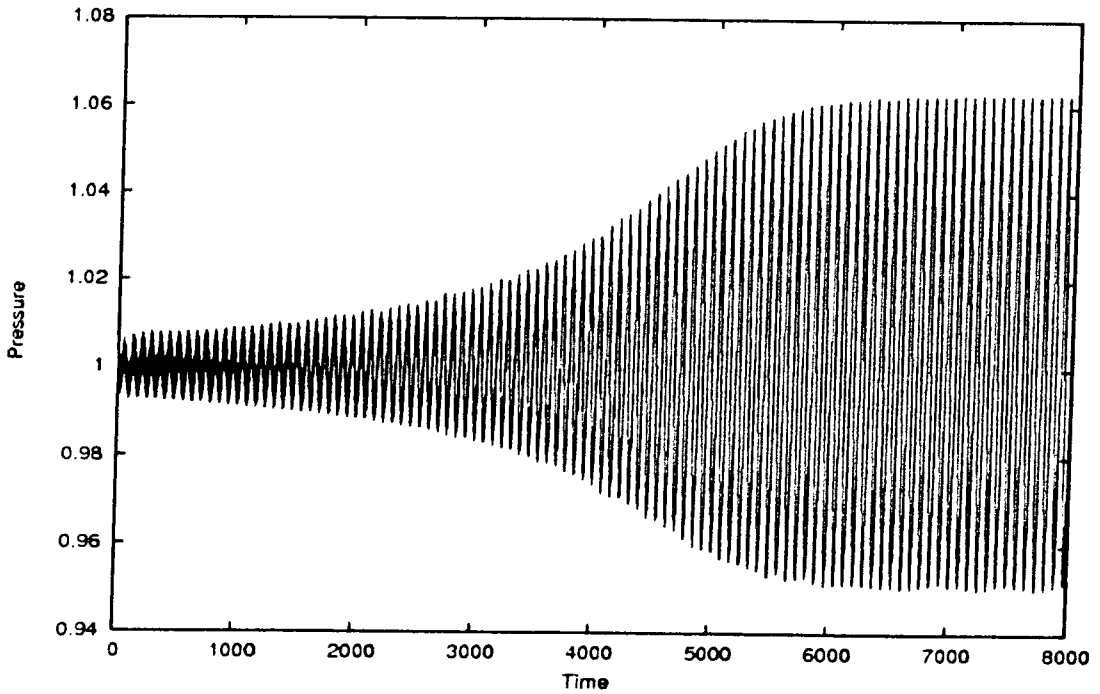

Figure F.15a - Shock pressure history for Q = 10.3875, E = 7.5, K_e = 0.21

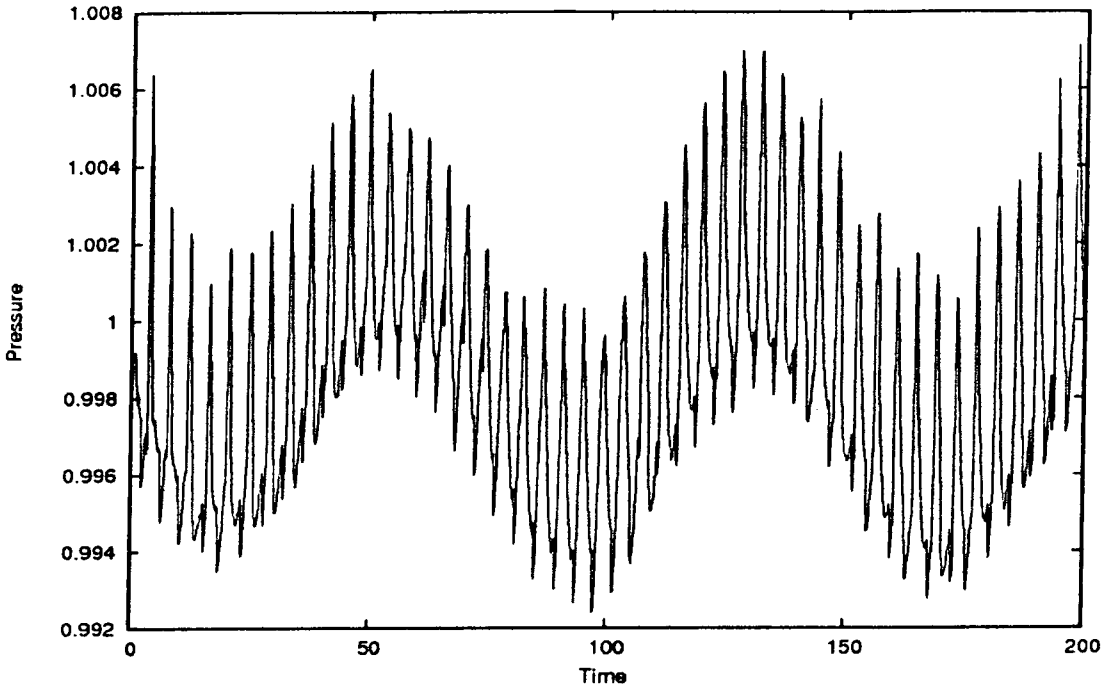

Figure F.15b - Shock pressure history for Q = 10.3875, E = 7.5, K_e = 0.21

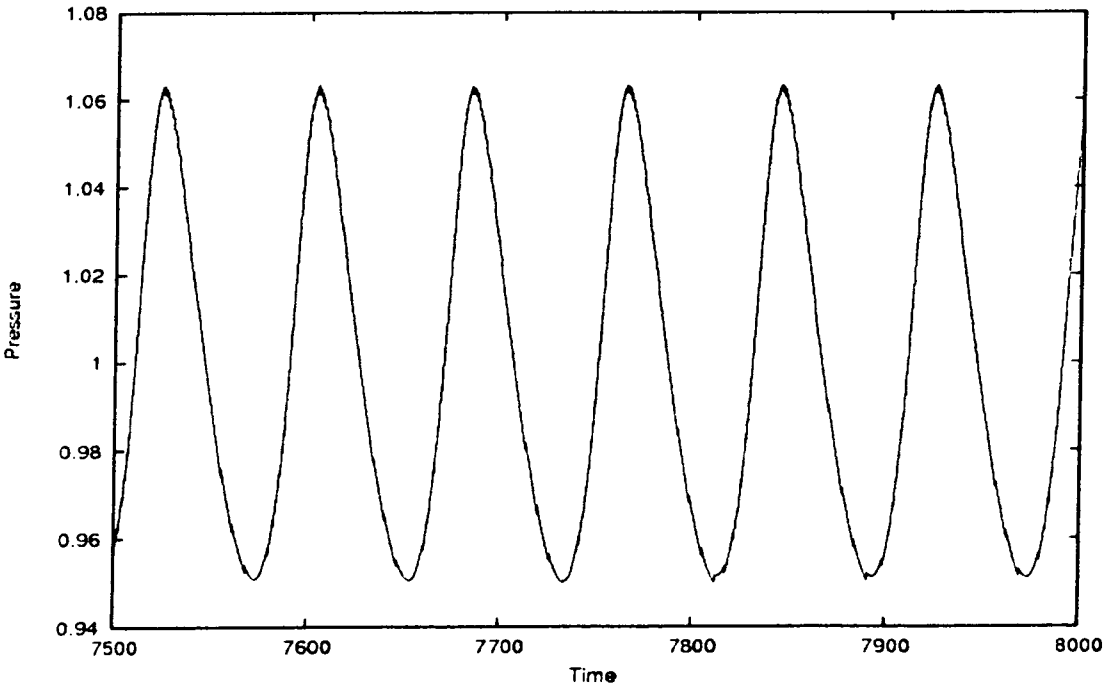

Figure F.15c - Shock pressure history for Q = 10.3875, E = 7.5, K_e = 0.21

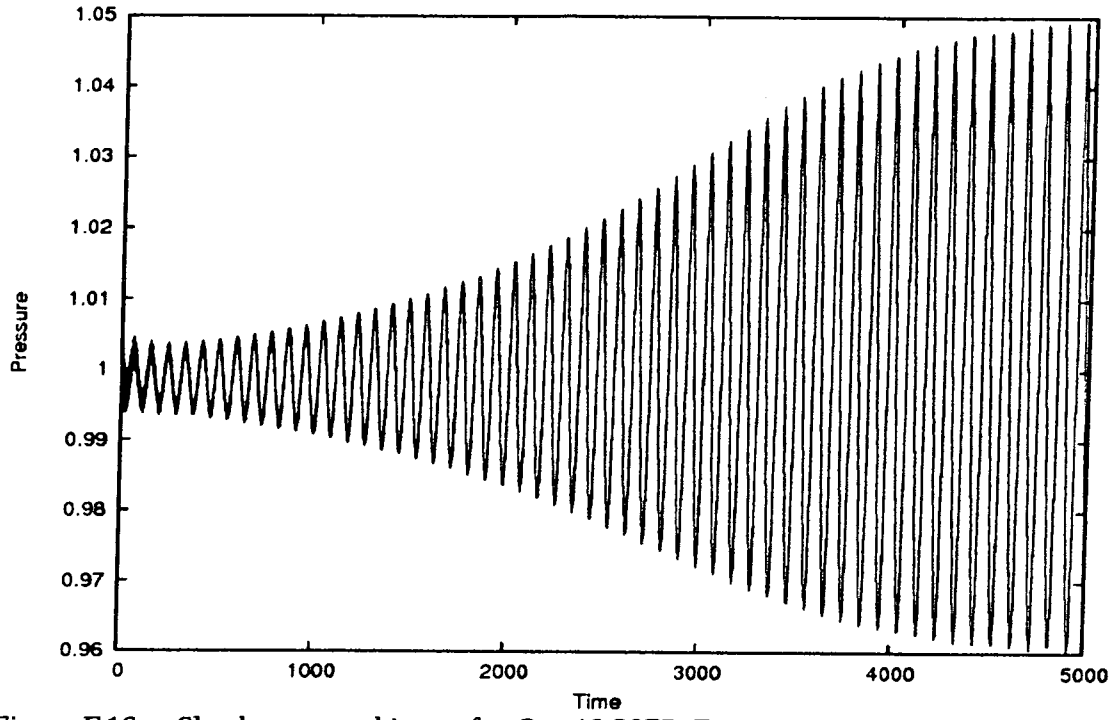

Figure F.16a - Shock pressure history for Q = 10.3875, E = 10, K_e = 0.15

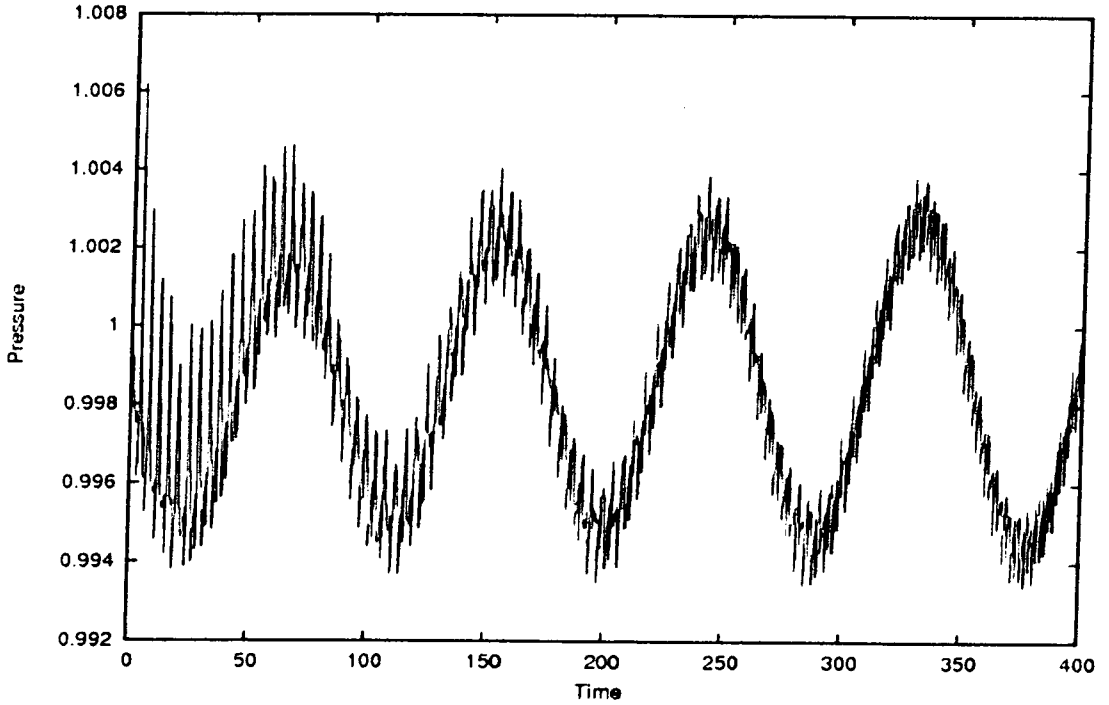

Figure F.16b - Shock pressure history for Q = 10.3875, E = 10, K_e = 0.15

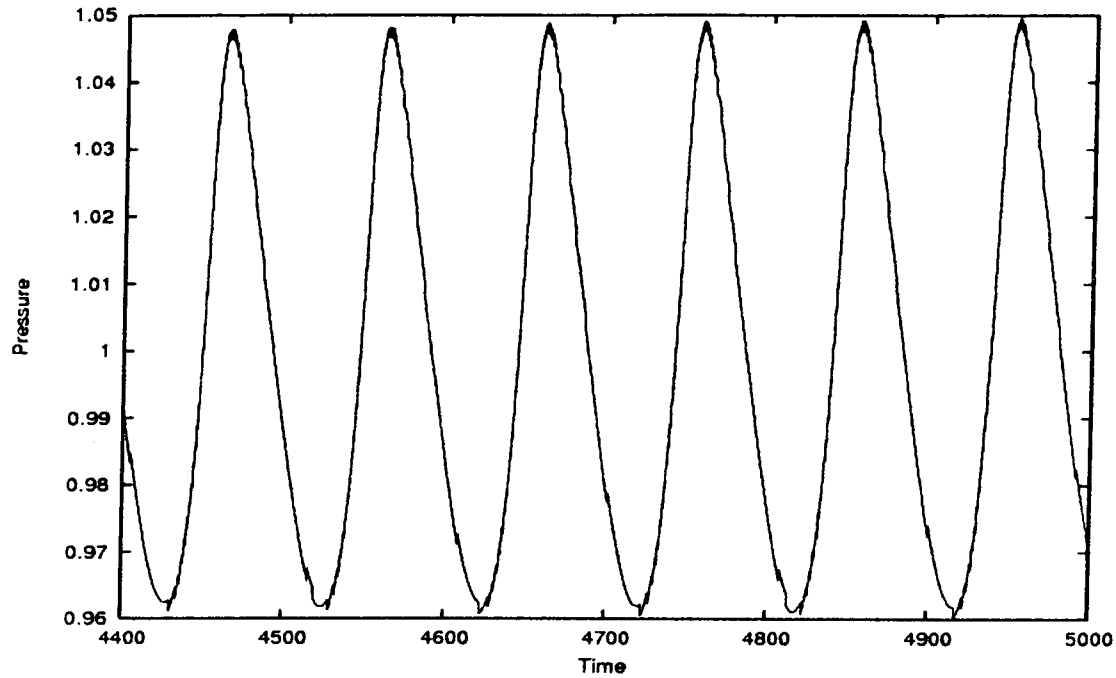

Figure F.16c - Shock pressure history for Q = 10.3875, E = 10, K_e = 0.15